Cell size-selective MRI for characterizing brain lesions in rodent models of tumor and radiation necrosis

By

Sean Philip Devan

Dissertation

Submitted to the Faculty of the

Graduate School of Vanderbilt University

in partial fulfillment of the requirements

for the degree of

DOCTOR OF PHILOSOPHY

in

Chemical and Physical Biology

May 31, 2022

Nashville, Tennessee

Approved:

John C Gore, PhD

Bruce M Damon, PhD

Adam W Anderson, PhD

Austin N Kirschner, MD, PhD

Junzhong Xu, PhD

Table of Contents

List of Figures

List of Tables

CHAPTER 1

Introduction

1.1 Motivation

With 1.7 million new cases and 600,000 deaths in 2018 in the United States [1], cancer remains a prominent disease in its severity and ubiquity. While it is promising that therapeutic improvements for many cancers have led to an annual increase in median 5-year survival, the increased longevity with cancer is accompanied by a higher incidence of brain metastases – estimated to occur in 10-30% of cancer patients [2,3], and up to 50% of patients with lung cancer [4], which is the most common site of origin. While brain metastases were historically treated with whole brain radiation therapy (WBRT), stereotactic radiosurgery (SRS) has increased in popularity due to its normal tissue sparing and decrease in neurocognitive detriments [5]. SRS has shown evidence of increased prognosis as well. Median survival for patients receiving a combination of WBRT and/or surgical resection was shown to be on the order of 4-9 months [6], and was increased to 46 months with SRS [7]. Despite this improvement, therapy of brain metastases tends to be palliative rather than curative, and many treated tumors show recurrence. Patient care is further complicated by treatment-induced injuries, notably radiation necrosis (radionecrosis), to the surrounding tissues. Though combining SRS with chemotherapy or immunotherapy leads to improved survival outcomes, incidence of radionecrosis is increased with these combination therapies [8,9]. Because recurrent tumor and radionecrosis are managed quite differently, either requiring aggressive re-treatments or conservative observation and pharmaceuticals, accurate *in vivo* assessment of the lesions is critical for managing patients following SRS treatments.

Biopsy is the most accurate method for distinguishing between lesions [10], but it is accompanied by the risks of neurosurgery including hemorrhage or patient death [11]. Diagnostic imaging using non-invasive techniques offers an advantage in patient safety. For instance, gadolinium-enhanced magnetic resonance imaging (Gd-MRI), which is sensitive to breakdown of the blood-brain barrier (BBB), is standard for localizing lesions pre- and post-therapy. However, neoangiogenesis is a hallmark of both tumor and radionecrosis and has highly permeable vessels to gadolinium chelates, resulting in a lack of specificity using the standard method [12]. Identifying

1

an advanced or quantitative mode of contrast beyond the routine imaging methods may be able to overcome this deficiency and improve patient care.

In vivo imaging has many modes of contrast, probing tissue changes at the molecular, vascular, and cellular levels. Several of these have been shown to discriminate between recurrent tumor and radionecrosis [13]. There are several molecular imaging methods that have been applied to this clinical problem. Positron emission tomography (PET) combined with computed tomography (CT) can be tailored to probe the concentration of molecular analogs tagged with positron emitters. ^{18}F-FDG, for instance, is a glucose analog widely used for identifying extracranial tumors, but has only moderate contrast in intracranial tumors due to the high energic demand of the healthy brain. Amino acid PET (e.g., ^{11}C-MET, ^{18}F-FET, ^{18}F-DOPA) has been proposed to overcome this challenge in FDG-PET, but with a pooled sensitivity of 85% and a specificity of 88% to differentiate radionecrosis from current brain metastases, the advantage is yet unclear [14]. The intrinsic low resolution, cost, time, and added radiation exposure may be additional disadvantages of PET/CT over other methods [15]. Proton MR spectroscopy (^{1}H MRS) is an alternative molecular imaging technique using clinical MRI scanners and can probe metabolites such as N-acetylaspartate (NAA), total choline (tCho), and total creatine (tCr). Ratios of NAA and tCr to tCho have shown the ability to discriminate between radiation necrosis and recurrent tumor [15–17]. These lesions can be small, however, and MRS has poor spatial resolution, with voxel sizes on the centimeter scale. Partial volume effects can therefore decrease the sensitivity to tumors. Chemical exchange saturation transfer (CEST) is an alternative molecular MRI approach with higher spatial resolution. In particular, amide proton transfer weighted (APTw) CEST, which is theorized to be sensitive to cytoplasmic proteins [18], was able to discriminate between tumor and radionecrosis in rodent models [19], but extension to human trials has met with varying results [20]. On the vascular level, a quantitative extension of Gd-MRI is dynamic susceptibility contrast (DSC), which uses the temporal profile of signal following injection of a contrast agent bolus to glean metrics such as cerebral blood volume (CBV). This is used for characterizing brain tumors in general [21] and recurrent tumor in particular [22], but cross-study variance in CBV thresholds has been high [23] and the use of exogenous contrast agents may have patient safety concerns. Cellular changes may be detectable by diffusion MRI. Mean diffusivity (MD), or the isotropic apparent diffusion coefficient (ADC), has been shown to correlate with cellularity [24]. Fractional anisotropy (FA) is an indicator of axonal fiber coherence and integrity [25], which can be disrupted

in intracranial lesional tissues. MD and FA can both be measured using diffusion tensor imaging (DTI) [26], which has been investigated to differentiate tumor from radionecrosis [27] but may suffer from a lack of specificity [28]. Despite attempts to probe such a wide array of tissue characteristics, no existing method is able to meet the challenge of differentiating tumor from radionecrosis, and it may be valuable to pursue alternative pathological features to increase specificity.

Because deregulated proliferation is a hallmark of malignant neoplasms, it is interesting that probes of cellularity are not specific to recurrent tumor. This may be due to the abundance of small restrictions, such as dendrites, axons, and glia, in brain tissue. Although cell sizes in brain metastases depend on the site of origin, the most common metastases have cell diameters of 10-20 μm – a few times larger than most restriction sizes in the brain. Cell size could therefore be a promising discriminator between radionecrosis and recurrent tumor. Diffusion MRI using varying diffusion times (t_{diff}) has shown sensitivity to cell size information. This has been applied with quantitative models in extracranial tumors, including prostate (VERDICT) [29] and breast (IMPULSED) [30] cancer. However, these models assume isotropic diffusion and have not been validated with mixtures of tumor cells with small restriction sizes, such as axons and dendrites. The anisotropy and heterogeneous cell sizes of the brain make extending quantitative models to intracranial tumors challenging. Higher angular sampling to account for anisotropy requires more scan time, which is not desirable for clinical applications. An alternative strategy is to filter signal by cell size, such that only cellular compartments of similar size to cancer cells contribute to contrast. This may be achievable using the change in signal with diffusion time, which has dependence on cell size and therefore may itself be a biomarker for cancer. By acquiring at a range of diffusion times, enabled by a combination of pulsed (PGSE) and oscillating (OGSE) gradient spin echo, signal from select cell sizes is emphasized while contributions from other compartments are suppressed. This method, named *size-selective imaging using filters via diffusion time* (SSIFT), effectively generates a cell size-weighted map that may be more specific to tumor than existing methods. The body of work described in this thesis comprises the practical development and preclinical validation of SSIFT for meeting the clinical need to differentiate radiation necrosis from recurrent tumor.

3

1.2 Goals and outline

The overarching goal of this thesis is to provide the foundational work for future human studies implementing time-dependent diffusion in differentiating brain tumor from radiation necrosis. To this end, these chapters comprise work describing the theoretical foundation for time-dependent diffusion, development of a practical method for cell size-selective contrast (SSIFT), and applications in preclinical models of tumor and radiation necrosis. Following this introduction, Chapter 2 gives a general overview of how the behavior of water in restricted environments is measured using MRI. This comprises a foundational mathematical description of the diffusion process, the coupling of water motion with phase encoding to drive MRI signal, and how signal can be interpreted using temporal diffusion spectroscopy to relate a measurement to quantitative restriction size. While the modeling framework is not explicitly used in the implementation of SSIFT, Chapters 3 and 4 use simulated signal crucial for the development and validation of the SSIFT methodology. Chapter 2 therefore builds up to the explicit equations used to generate this signal.

Chapter 3 gives a brief survey on how cell size has been used in studies of cancer and why this is challenging to extend to the brain. We then introduce the theoretical basis for SSIFT and demonstrate why this can offer a more sensitive map to cancer than conventional diffusion imaging. Simulation is used to provide guidance on a choice of protocol. Some effects from artifacts are considered that may need special consideration in SSIFT compared to conventional diffusion. Finally, a descriptive summary of the acquisition and preprocessing methods is given.

Chapter 4 is the first of three experimental studies in this thesis and tests hypotheses regarding the correlation of SSIFT with biophysical parameters and its efficacy as a discriminator between radiation necrosis and tumor. First, simulated synthetic intra- and extracellular signals are generated to compare SSIFT to the apparent diffusion coefficient and the diffusion dispersion rates. This not only demonstrates that a new pattern of contrast can be generated, but also allows evaluation of noise effects on each output. *In vitro* imaging of cell pellets is then applied to demonstrate that SSIFT is sensitive to cancer cells and insensitive to potentially competing intracellular compartments such as lymphocytes. *In vivo* imaging of tumor and radiation necrosis in rats allows comparison of cellularity in different etiologies to assess the dependence of SSIFT on the number of cells. ROI-averaged values in tumor and radiation injury are compared to demonstrate that SSIFT has potential to differentiate these lesion types. Finally, a proof-of-concept

comparison of human subjects is performed to demonstrate that the method is feasible on human systems and that the patterns of contrast seen in animals translates to human tissue.

While Chapter 4 shows that SSIFT has potential to differentiate radiation necrosis from tumors, there are many other MRI methods that purport to do the same. In Chapter 5, we compare some of these methods to see what role SSIFT should play relative to them and to determine which methods offer complimentary, redundant, or insufficient contrast. We therefore apply diffusion, quantitative magnetization transfer (qMT), chemical exchange saturation transfer (CEST), and dynamic susceptibility contrast (DSC) methods to the rodent models of tumor and radiation necrosis. In addition to single parameter comparisons, there is currently little literature detailing how multiple parameters can be quantitatively combined to assess differentiating these lesions. To address this, we explore various processing schemes using penalized logistic regression to generate a generalized linear model of the fitted data. We demonstrate how parameters from each method can be chosen, how they can be combined in a generalized linear model, and how SSIFT fits in with the rest of the methods.

In Chapter 6, we offer methodology details and histological validation of the novel rodent radiation necrosis model used in Chapters 4 and 5. Models of radiation necrosis typically either use specialized equipment or have beam characteristics (energy, dose rate) which do not model human therapies. There is no current model for clinical energy (6+ MV) linear accelerator-based stereotactic radiosurgery (LINAC-SRS) in rodents which can solve this problem. Chapter 6 offers further explanation of a reproducible LINAC-SRS model of radiation injury in mice and rats. We describe the animal setup, on-board imaging alignment with the dose plan, and arc and couch configurations for treatment. We validate via histology that this method shows characteristics of radiation necrosis seen in humans. We image the treated animals using gadolinium (Gd)-enhanced MRI, which allows us to identify targeting accuracy and track lesion progression in the high dose mice, as these have never been reported using any LINAC treatment in animals.

Finally, Chapter 7 provides a summary of the results and a discussion of their limitations and impact. The outcome of this work is a new, practical method for leveraging signal dependence on diffusion time to generate cell size-based contrast in brain imaging. This method is validated through simulation, *in vitro* imaging with correlation to microscopy, *in vivo* imaging with correlation to histology. Patient data demonstrates that this is a practical method in humans and has potential to differentiate radiation necrosis from tumor. A framework for multiparametric MRI

is provided and SSIFT is compared to other quantitative methods to inform how human studies of SSIFT could incorporate other methods for comparison or complementary information. A practical and reproducible method for treating mice with high dose radiotherapy is also described and validated. This work overcomes existing obstacles for implementing cell size imaging in the brain with a fast, practical method to increase specificity to tumors. Through the development and preclinical validation of SSIFT, this work provides an acquisition and processing framework to differentiate radiation necrosis from tumor in future human studies.

CHAPTER 2

Background

As we will see, the central method used in this thesis, *SSIFT*, is simple in its implementation and its output has highly conspicuous results in cancer. However, in order to understand, develop, validate, and interpret the method we will rely on concepts based in diffusion physics, magnetic resonance imaging (MRI), temporal diffusion spectroscopy, the current state of research on microstructural modeling using diffusion-weighted MRI, and particular challenges to diffusion imaging in the brain. This chapter is intended to give an overview of these topics.

Section 2.1 walks through the basic principles of diffusion in free water with the goal of setting the framework of diffusion as a stochastic process described in terms of a probability distribution. Section 2.2 highlights some foundational concepts in MRI, with the disclaimer that MRI is far too extensive to even cover in one section, let alone one thesis. We will therefore build up to the sources of contrast due to diffusion and relaxation that are necessary for modeling *SSIFT* in a spin-echo sequence, and will forego a lengthy discussion on alternative acquisition schemes, reconstruction, and radiofrequency (RF) pulses, which are all rich fields on their own. Section 2.3 merges the concepts to Section 2.1 and Section 2.2 to detail the Stejskal-Tanner experiment to measure diffusivity and define the framework for diffusion imaging. Section 2.4 details the effects of restrictive barriers on water diffusion, using simulated Monte Carlo results to illustrate the impact of restriction size and diffusion time on molecular displacements. Section 2.5 defines the conventional diffusion metric (the *apparent diffusion coefficient,* ADC) and diffusion tensor imaging, how restriction drives their contrast, and why they may lack specificity to restriction sizes. Finally, Section 2.6 defines an alternative framework to conventional methods, *temporal diffusion spectroscopy*. This section will also define the gradient waveforms and signal equations used in later chapters for measured and simulated signal.

2.1 Free water diffusion

In 1827 Robert Brown observed through a magnifying lens particles extracted from flower pollen suspended in water exhibiting motion [31]: "These motions were such as to satisfy me, after

frequently repeated observation, that they arose neither from currents in the fluid, nor from its gradual evaporation, but belonged to the particle itself." This observation of what he calls "active molecules," though quite enigmatic to Brown, describes the phenomenon we now know as diffusion: the motion of molecules generated solely through a system's internal thermal energy. A few decades after Brown's observation, Adolf Fick would observe on a macroscopic level that the transport of concentrate in a solution is analogous to Fourier's and Ohm's observations in the transport of heat and charge. He modeled the change in solute concentration f over time t along dimension r using the heat equation [32]:

$$\frac{\partial f}{\partial t} = D\frac{\partial^2 f}{\partial r^2} \tag{1}$$

This is known as Fick's Second Law and gives a mathematical definition of the diffusion coefficient D as the rate of expansion of a concentration kernel. Fourier had previously solved this in his studies of heat for one case that will be of interest to us: the propagation of particles originating at a single point r_0, i.e. $f(t=0) = \delta(r - r_0)$, which has a Gaussian solution [33]:

$$f(r) = \frac{1}{\sqrt{4\pi Dt}}e^{-\frac{(r-r_0)^2}{4Dt}} \tag{2}$$

Although Fick only considered the one-dimensional case in his experiment, Equation (1) extends to higher dimensions as:

$$\frac{df}{dt} = D\nabla^2 f \tag{3}$$

Although this result was understood at a mathematical and observational level, it was not until Albert Einstein's 1905 work that Fick's macroscopic description would be related to the microscopic phenomenon observed by Brown [34]. To do so, Einstein describes a model of random molecular motion to build a statistical mechanical framework for diffusion consistent with modern understanding. He considers molecular motion in 1-dimension as a random walk: during a time interval τ, a particle will move a distance δ in either the positive or negative direction with equal probability. The particle's position r at time t is then described as:

$$r_t = r_{t-\tau} \pm \delta \tag{4}$$

Einstein uses this model to derive Fick's equation from a statistical view of molecular motion and points out an important result from the known Gaussian solution, the ensemble-mean square displacement measured at a diffusion time t_{diff}:

$$l^2 = \langle (r - r_0)^2 \rangle = 2Dt_{diff} \tag{5}$$

Here η is the characteristic or diffusion length. This is extended into n-dimensional diffusion as:

$$l^2 = 2nDt_{diff} \tag{6}$$

To illustrate this idea, Figure 1 shows an example 1-dimensional trajectory of such a model, and a simulated distribution of many ($N_{trial} = 10^4$) such particles.
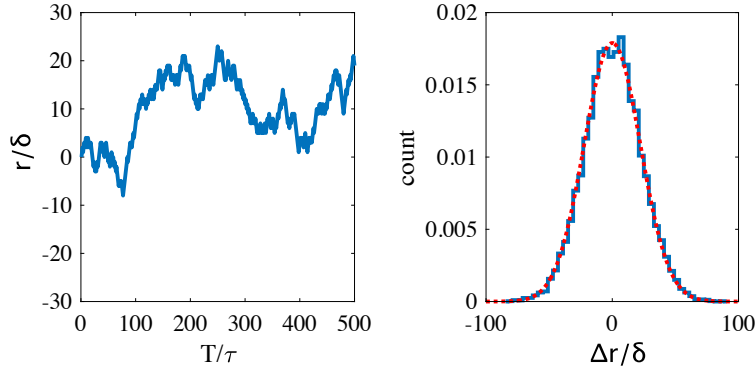
Figure 1. 1-dimensional free water Monte Carlo demonstration. (left) The position of a simulated particle undergoing diffusion with normalized units over 500 steps. (right) The blue curve shows a histogram of endpoints for 10^4 particles and follows a binomial distribution. The red curve is the Gaussian asymptotic limit of the binomial distribution with a large sample.

While these relations hold for the diffusion of an arbitrary solute in any ideal molecular kinetic system, for this thesis we are interested in *water self-diffusion*, or the diffusion process of water molecules in a solution of water. In this case, Fick's law needs to be rephrased, since the concentration gradient of water in water is zero everywhere. Einstein's framework of diffusion as a stochastic process allows us to define the *diffusion propagator* $P(\boldsymbol{r}, t; \boldsymbol{r}_0)$, which is the probability that a particle originating at location $\boldsymbol{r}_0$ assumes position $\boldsymbol{r}$ at time t. The propagator plays the same role as the solute concentration (i.e., we can imagine water molecules originating at $\boldsymbol{r}_0$ are identical to yet identifiable from the rest of the water solution):

$$\frac{\partial P}{\partial t} = D \frac{\partial^2 P}{\partial r^2} \tag{7}$$

By definition, $P(t = 0) = \delta(\boldsymbol{r} - \boldsymbol{r}_0)$. Using this initial condition, in free water, the Gaussian propagator allows for relatively simple estimates of D by probing the system at one subsequent time point, which can be done using diffusion NMR.

9

2.2 Magnetic resonance imaging (MRI)

Nuclear magnetic resonance (NMR) generally describes the response of nuclear magnetic moments to external electromagnetic radiation of particular frequencies. Following Stern's 1933 discovery that protons have a net magnetic moment[1] [35,36], Rabi performed the foundational experiment detecting NMR in a proton beam[2] [37]. Bloch and Purcell would extend this to solids[3] [38][39], and Hahn in liquids [40]. Generating NMR signal using Hahn's method broadly relies on three tools: (a) manipulating precessional frequency of the nuclear magnetic moments through an external magnetic field, (b) manipulating the orientation of magnetic moments through an applied (transmit) RF pulse, and (c) detecting the net magnetization as signal through a receive coil. This section will summarize how these can be combined in a *spin-echo* pulse sequence to generate signal, after which our discussion will detail how signal can be sensitized to diffusion using spatially and temporally varying fields.

Nuclei with non-zero spin have a magnetic moment $\boldsymbol{\mu}$. With no external magnetic field, an ensemble of many spins is uncorrelated and has a net magnetization of zero. However, when experiencing an external field $\boldsymbol{B_0}$ the spins are preferentially aligned parallel to the field, with a net magnetization $\boldsymbol{M_0}$. Individual spins precess around about $\boldsymbol{B_0}$ with the *Larmor frequency*:

$$\omega_0 = -\gamma B_0 \qquad (8)$$

where γ is the *gyromagnetic ratio*, or $267.5 \cdot 10^{-6}$ rad/s/T for hydrogen nuclei in water. When the field $\boldsymbol{B}$ is not colinear with the magnetization $\boldsymbol{M}$, a torque is applied:

$$\frac{\partial \boldsymbol{M}}{\partial t} = \gamma \boldsymbol{M} \times \boldsymbol{B} \qquad (9)$$

Using this, the orientation of the net magnetization can be manipulated away from $\boldsymbol{B_0}$ by applying a transverse RF pulse at the Larmor frequency. The field generated by this pulse is denoted $\boldsymbol{B_1}$. When a component of $\boldsymbol{M}$ is placed into the transverse plane, the precession of the transverse component of $\boldsymbol{M}$ can induce a current through an RF coil to be detected as signal. By convention, the transverse plane has axes x, y and the longitudinal axis parallel to $\boldsymbol{B_0}$ is z. We generally describe the magnetization $\boldsymbol{M_{xy}}$ in a rotating reference frame, which rotates at the Larmor

---

[1] 1943 Nobel Prize in Physics "for his contribution to the development of the molecular ray method and his discovery of the magnetic moment of the proton."
[2] 1944 Nobel Prize in Physics "for his resonance method for recording the magnetic properties of atomic nuclei."
[3] 1952 shared Nobel Prize in Physics "for their development of new methods for nuclear magnetic precision measurements and discoveries in connection therewith."

frequency relative to the scanner coordinates and transverse to the applied field $\boldsymbol{B_0}$. The phase φ of a spin is defined as the angle between its moment $\boldsymbol{\mu}$ and this rotating frame. The signal $s(t)$ read in this plane is the sum of signal from each magnetic moment with density $\rho(x, t)$. In a spatially varying field, the signal is modulated by the phase distribution:

$$s(t) = \int_{-\infty}^{\infty} \mu_{xy}\rho(\boldsymbol{r}, t)e^{-i\phi(\boldsymbol{r})}d\boldsymbol{r} \tag{10}$$

The signal dependence on phase can be leveraged to encode spatial information in the spin phase distribution. Lauterbur first did this for image formation using magnetic gradients – added magnetic fields with magnitude linearly dependent on any axis and with direction along $\boldsymbol{B_0}$.[4] The effective Larmor frequency during the application of a gradient with field $\boldsymbol{G}$ is:

$$\omega = \gamma(\boldsymbol{G} \cdot \boldsymbol{r} + B_0) \tag{11}$$

Note, the notation $\boldsymbol{G}$ is vectorized in the spatial dependence, not field direction. I.e.:

$$\boldsymbol{G} = \left(\frac{\partial B_z}{\partial x} \quad \frac{\partial B_z}{\partial y} \quad \frac{\partial B_z}{\partial z}\right)^\top \tag{12}$$

When a gradient is played for a time, the phase of a spin at location $\boldsymbol{r}$ is:

$$\varphi(t) = \gamma \int_0^t \boldsymbol{G}(t') \cdot \boldsymbol{r}(t')dt' \tag{13}$$

For durations short enough that $\boldsymbol{r}$ is constant with time, we can define a parameter $\boldsymbol{k}$ as:

$$\boldsymbol{k} = \frac{\gamma}{2\pi} \int_0^t \boldsymbol{G}(t')dt' \tag{14}$$

and relate our signal as:

$$s(t) = \int_K \rho(\boldsymbol{r})e^{-2\pi i k(t) \cdot \boldsymbol{r}}d\boldsymbol{k} \tag{15}$$

where K is the domains of $\boldsymbol{k}$. This is a remarkably convenient representation, as $s(t)$ is then the inverse Fourier transform of the net transverse magnetization density, which is the image.

---

[4] 2003 Nobel laureate Paul Lauterbur proposed that the joint use of gradient and static fields be called *zeugmatography* from the Greek ζευγμα for "that which is used for joining," and the image generated be called a *zeugmatogram*. While it caught on with some contemporaries, such as his fellow Nobel laureate Sir Peter Mansfield, for better or worse this terminology did not find a place in their extensive impact on MRI.

There are several mechanisms that affect M_{xy} and yield contrast in the image. Spins in the excited transverse orientation will return to thermal equilibrium along the longitudinal axis with some probability over time. Bloch models this relaxation as an exponential recovery:

$$\dot{M}_z = -\frac{1}{T_1}(M_z - M_0) \qquad (16)$$

where T_1 is the longitudinal[5] relaxation time.

Phase incoherence can be caused by spins in an ensemble experiencing non-uniform fields causing further relaxation from a few mechanisms: (a) stochastic fluctuations in local fields caused by motion of adjacent dipoles (T_2-relaxation), (b) spatial heterogeneity in the magnetic field within the ensemble (T_2'-relaxation), and (c) movement of spins between spatially varying fields (diffusion).

The effects of T_2'-relaxation can be mitigated through a spin echo experiment. This occurs in three steps:

1. An *excitation pulse*, or a B_1 field rotating M into the transverse plane, is applied. Spin phase coherence decreases with transverse relaxation. At a time τ, each spin has accumulated a phase $\Delta\varphi$ relative to the rotating frame due to T_2'-relaxation.

2. A *refocusing pulse*, reflects the transverse magnetization M_{xy} so that the effective phase from the rotating frame is $-\Delta\varphi$.

3. At time t following the refocusing pulse, each spin accumulates another phase $\Delta\varphi$, which reverses the preceding $-\Delta\varphi$. This brings the phases back into coherence and maximizes the signal from M_{xy}. The *spin echo* is the signal generated at time 2τ and is read through the receive coil. This time point is the *echo time*, often denoted TE.

This reversal of T_2' effects relies on the assumption that local field heterogeneities are time-invariant and that spins do not move substantially relative to the spatial gradient of the field, so that $\Delta\varphi$ is the same before and after the refocusing pulse. Since the stochastic interactions

---

[5] In *Nuclear Induction*, Felix Bloch refers to T_1 as the *thermal relaxation time* [38]. With this phrasing, he points out a qualitative difference between T_1 and T_2: T_1-relaxation is a change in nuclear energy state, whereas T_2-relaxation is a net ensemble effect. While this is a useful distinction on a physical level, *longitudinal* and *transverse* more accessibly describe the equations they govern. Bloembergen also called T_1 relaxation *spin-lattice* relaxation [186] following early experiments in salt crystals (e.g. Heitler and Teller [187]) which described thermal relaxation as a deposition of energy from the excited *spin* into the crystal *lattice*. Although most modern MRI applications are performed on non-crystal water, this name is still common.

governing T_2-relaxation and diffusion do not have a constant $\Delta\varphi$, they are not reversible with this experiment. Bloch models the effects of T_2-relaxation as an exponential decay:

$$\dot{M}_{xy} = -\frac{1}{T_2} M_{xy} \qquad (17)$$

which can be combined with the model for T_1 relaxation to build a governing equation for $\boldsymbol{M}$:

$$\dot{\boldsymbol{M}} = \gamma \boldsymbol{M} \times \boldsymbol{B} - \frac{1}{T_2} \boldsymbol{M}_{xy} - \frac{1}{T_1}(M_z - \boldsymbol{M}_0) \qquad (18)$$

The following section describes how we can apply time-varying gradients to encode spins with phase to glean information on water diffusion.

2.3 Pulsed gradient spin echo (PGSE) and the Stejskal-Tanner experiment in free water

The general principle of diffusion encoding in MRI is to use a diffusion-sensitizing gradient scheme to map the spin displacement distribution $P(\boldsymbol{r})$ to a phase distribution $p(\varphi)$. This gives a signal:

$$S = S_0 \int_{-\infty}^{\infty} d\varphi\, p(\varphi) e^{-i\varphi} = S_0 \langle e^{-i\varphi} \rangle \qquad (19)$$

where S_0 is the signal without the diffusion-weighting gradients. Because the gradient $\boldsymbol{G}(t)$ is known and the attenuated signal S/S_0 is measurable, modeling can be used to approximate information on the spin displacements. A simple experiment to quantify the diffusion coefficient D in free water using this relationship was performed by Stejskal and Tanner [41]:

1. Using a spin-echo sequence, a gradient with duration δ is played following excitation to spatially encode spins with a net phase. This has a dephasing effect on the ensemble of spins with different $\boldsymbol{r}_0$. If δ is sufficiently small such that $|\boldsymbol{r}(\text{t}) - \boldsymbol{r}_0|_{t<\delta} \approx 0$ (called the *short pulse approximation* [42]), then the net phase is:

$$\varphi_1(\boldsymbol{r}_0) = \gamma \int_0^{\delta} \boldsymbol{G} \cdot \boldsymbol{r}_0 dt = \gamma \delta \boldsymbol{G} \cdot \boldsymbol{r}_0 \qquad (20)$$

2. Spins mix freely during a diffusion time Δ from the first pulse. The displacement distribution follows the diffusion propagator (Equation (2)), so the probability of a spin at location $\boldsymbol{r}$ having phase $\varphi_1(\boldsymbol{r}_0)$ is $P(\boldsymbol{r}, \Delta; \boldsymbol{r}_0)$. In free water this is Gaussian-distributed. During this time a refocusing pulse at time τ reflects the phases from φ_1:

13

$$\varphi_1(t > \tau) = -\varphi_1(t < \tau) \tag{21}$$

3. A second gradient equal to the first is played at time Δ following the start of the first gradient. The second gradient then gives additional phase:

$$\varphi_2(\boldsymbol{r}) = \gamma \int_\Delta^{\Delta+\delta} \boldsymbol{G} \cdot \boldsymbol{r} \, dt = \gamma \delta \boldsymbol{G} \cdot \boldsymbol{r} \tag{22}$$

The net phase of a spin is then:

$$\varphi = \varphi_2(\boldsymbol{r}) - \varphi_1(\boldsymbol{r_0}) = \gamma \delta \boldsymbol{G} \cdot (\boldsymbol{r} - \boldsymbol{r_0}) \tag{23}$$

The gradients are balanced (i.e., $\boldsymbol{G}(t)$ has a central moment of 0), so stationary spins have their phase completely rewound. Spins that do move have a net phase linear with their displacement.

4. The signal is read at time TE and the free water diffusion coefficient D is modeled from the signal. Douglass and McCall [43] demonstrated that the ensemble average of Gaussian-distributed phases is itself Gaussian-distributed (the *Gaussian phase approximation*):

$$S = S_0\langle e^{-i\varphi} \rangle \approx S_0 e^{-\frac{1}{2}\langle \varphi^2 \rangle} = S_0 e^{-\frac{1}{2}(\gamma \delta G)^2 \langle r - r_0 \rangle^2} = S_0 e^{-\frac{1}{2}(\gamma \delta G)^2 (2Dt_{diff})} \tag{24}$$

The diffusion time t_{diff} can be approximated as Δ for short δ, but typically is defined as $\Delta - \frac{\delta}{3}$. The exponent can be separated into D and the design parameters grouped as b:

$$S = S_0 e^{-bD} \tag{25}$$

D is then simply:

$$D = -\frac{1}{b}\ln(S/S_0) \tag{26}$$

This acquisition method using short rectangular diffusion-sensitizing gradients is referred to as *pulsed gradient spin echo*, or PGSE. For time-varying fields (PGSE with non-negligible δ or other waveforms covered in later sections), the phasing is given by:

$$\boldsymbol{F}(t) = \gamma \int_0^t \boldsymbol{G}(t')dt' \tag{27}$$

Stejskal and Tanner showed that the signal can be formalized as:

$$S = S_0 \exp\left(\int_0^{TE} \boldsymbol{F}(t)^\mathsf{T} \cdot \boldsymbol{D} \cdot \boldsymbol{F}(t)dt\right) \tag{28}$$

And the diffusion weighting b-value is:

$$b = \int_0^{TE} F(t)^2 dt \qquad (29)$$

which, for a PGSE preparation with finite δ, is:

$$b = (\gamma \delta G)^2 \left(\Delta - \frac{\delta}{3} \right) \qquad (30)$$

2.4 Restricted diffusion: dependence of diffusivity on diffusion time and restriction size

In the presence of restrictive non-permeable barriers, a particle's trajectory is trapped and the ensemble RMSD decreases. In this case the propagator becomes non-Gaussian. This is illustrated in Figure 2.
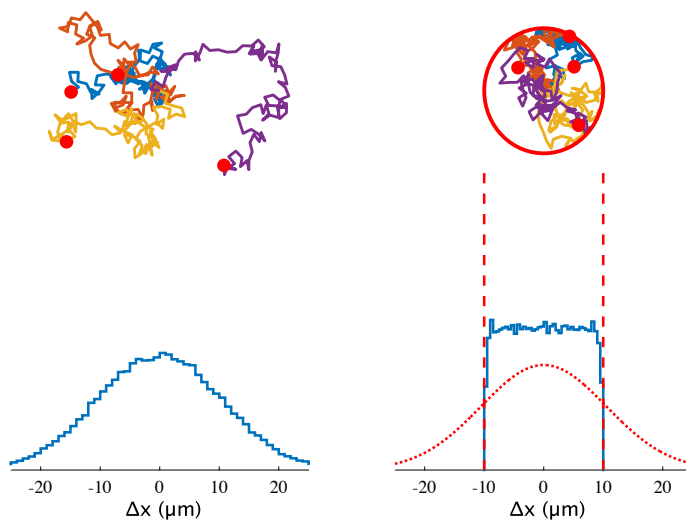
Figure 2. Restricted Diffusion. (left) Histogram of simulated water displacements Δx show a Gaussian distribution. (right) In the presence of restrictive barriers, the distribution (blue solid line) has a narrowed RMSD compared to the would-be distribution in free water (red dashed line).

At short times, few molecules experience the effects of a barrier and the RMSD approaches the intrinsic diffusion length: $\lim_{t \to 0} \langle (r - r_0)^2 \rangle = l^2$. However, with longer diffusion times, the RMSD decreases. A simulation demonstrating this is shown in Figure 3, with 10^4 particles, t_{step}=0.1 ms, intrinsic diffusivity 1.58 µm²/ms. The fraction of molecules that interact with the barrier in a given

diffusion time decreases with the radius. The RMSD of particles increases with restriction size, and the diffusivity then appears more Gaussian. This is shown in Figure 4. The trends of increased RMSD with size and decreased RMSD with time in restricted barriers forms the basis of the SSIFT method described in Chapter 3.
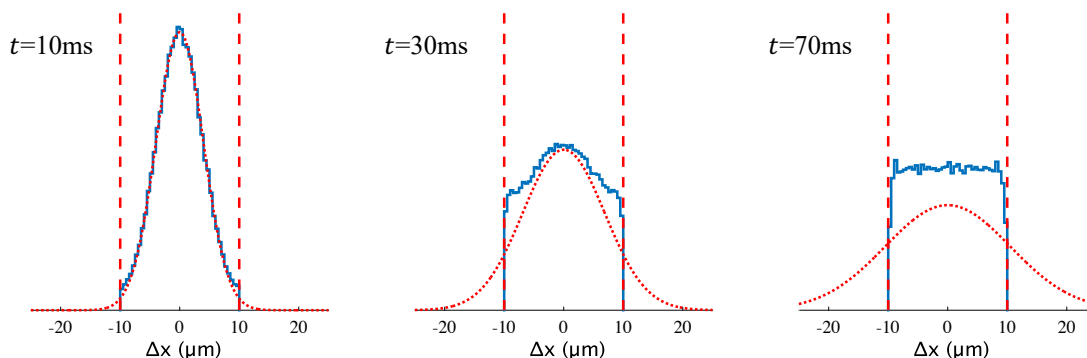
Figure 3. Diffusion time dependence. Histograms from a 1D Monte Carlo experiment show water displacements from initial position at the center of the restricted space. At short diffusion times water diffusion (blue) is roughly Gaussian (red). With longer diffusion times more particles interact with the restrictive barrier and the RMSD is smaller than the Gaussian case.
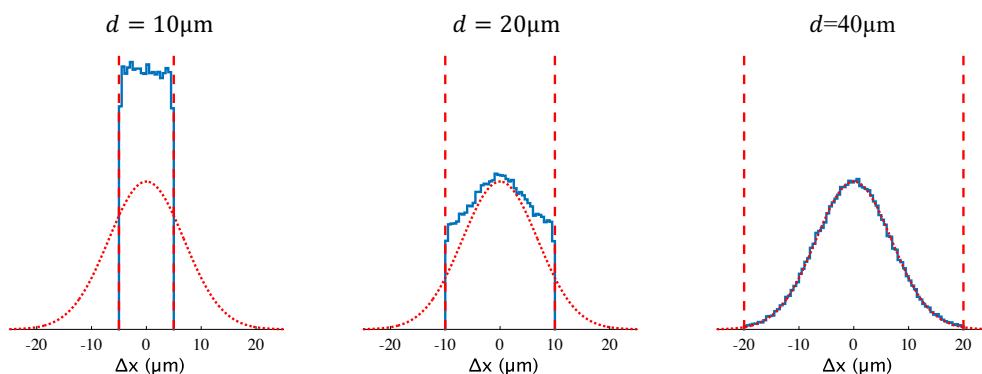
Figure 4. Diffusion dependence on restriction size. The fraction of water particles within the characteristic diffusion length from the barrier decreases with cell size. A 1D Monte Carlo experiment in a restricted medium shows water diffusion in larger cells approaches free water behavior.

2.5 The apparent diffusion coefficient (ADC) and diffusion tensor imaging (DTI)

In free water, the Stejskal-Tanner experiment measures the intrinsic physical parameter D through Equation (26). In restricted diffusion, however, this is not the case. As restrictions drive a smaller RMSD of spins, the phase variance decreases. This coherence of phases leads to higher signal and Equation (26) then gives a smaller measured diffusivity. The diffusivity measured in this way is therefore reported as the *apparent* diffusion coefficient (ADC), which is the diffusivity of free water which, if measured with the same b value, would give the acquired signal.

$$ADC = -\frac{1}{b}\ln(S/S_0) \qquad (31)$$

Since the ADC is sensitive to restrictions, the source of contrast in ADC maps may be better described by the deviance from the Gaussian model than changes intrinsic diffusivity. This can be useful to distinguish media with and without restrictions. It can also be used to probe anisotropic geometries. For instance, water restricted between two parallel planes or within a cylinder will have a larger RMSD parallel to the barrier than perpendicular to it. In this case the diffusivity is a positive definite and symmetrical matrix:

$$\boldsymbol{D} = \begin{pmatrix} D_{xx} & D_{xy} & D_{xz} \\ D_{yx} & D_{yy} & D_{yz} \\ D_{zx} & D_{zy} & D_{zz} \end{pmatrix} \qquad (32)$$

The Gaussian propagator in this case is given a matrix form:

$$P(\boldsymbol{r}, t; \boldsymbol{r}_0) = \frac{1}{\sqrt{|\boldsymbol{D}|4\pi t}} e^{\frac{-(\boldsymbol{r}-\boldsymbol{r}_0)^{\mathsf{T}}\boldsymbol{D}(\boldsymbol{r}-\boldsymbol{r}_0)}{4t}} \qquad (33)$$

The eigenvalues λ of $\boldsymbol{D}$ then follow Einstein's relation:

$$\langle(r_i' - r_{i,0}')^2\rangle = 2\lambda_i t \qquad (34)$$

where r_i' is the component of $\boldsymbol{r}$ along the ith eigenvector of $\boldsymbol{D}$. $\boldsymbol{D}$ can be determined by applying gradients along any set of directions spanning the three-dimensional space, and each measurement is solved by:

$$\ln\left(\frac{S}{S_0}\right) = -\sum_{i,j} b_{ij} D_{ij} \qquad (35)$$

where i, j parametrize the three spatial axes. With assumptions about diffusion symmetry ($D_{ij} = D_{ji}$), the diffusion tensor in any orientation is fully characterized by six degrees of freedom and

describes the covariance matrix of displacement. Assuming restrictions are the driving contrast between the diffusion eigenvalues [25] which causes anisotropy in the diffusion tensor, we consider these eigenvalues to be apparent diffusivities rather than intrinsic values as well.

In addition to recovering the full diffusion tensor, four parameters are typically defined by the three eigenvalues to comprise *diffusion tensor imaging* (DTI):

$$Fractional\ Anisotropy\ (FA) = \sqrt{\frac{(\lambda_1 - \lambda_2)^2 + (\lambda_1 - \lambda_3)^2 + (\lambda_2 - \lambda_3)^2}{2\sum\lambda_i^2}} \qquad (36)$$

$$Mean\ Diffusivity\ (MD) = \frac{1}{3}\sum\lambda_i \qquad (37)$$

$$Axial\ Diffusivity\ (AD) = \lambda_1 \qquad (38)$$

$$Radial\ Diffusivity\ (RD) = \frac{\lambda_2 + \lambda_3}{2} \qquad (39)$$

When directional information such as FA or the eigendirections of $\boldsymbol{D}$ are not important, the trace of $\boldsymbol{D}$ can be quickly calculated as an analog to MD. Since the trace is rotationally invariant, the orientation of $\boldsymbol{D}$ does not need to be known and an acquisition along any set of three orthogonal gradient directions can give:

$$\bar{S} = \sqrt[3]{S_x S_y S_z} \qquad (40)$$

The geometric mean of the signal is equivalent to the arithmetic mean of the log signal we can calculate:

$$-\frac{1}{b}\ln\left(\frac{\bar{S}}{S_0}\right) = \frac{(D_{xx} + D_{yy} + D_{zz})}{3} \qquad (41)$$

which gives an isotropic average ADC.

One limitation of ADC is in restricted water where diffusion is time dependent, in which case ADC is also reliant on the gradient timing parameters and is therefore not intrinsic to the system. As shown in Section 2.4, the diffusion time-dependence carries structural information (e.g. pore

18

size) that may be more specific than ADC. PGSE, however, is generally unable to achieve sufficiently short diffusion times to probe this due to hardware constraints: reducing Δ requires increasing G. Additionally, PGSE only encodes information on the net displacement of spins and is agnostic to intermediate points of the spin trajectories that may give more efficient information. Varying the gradient waveforms may therefore alter the sensitivity to diffusion in restricted media. The following section details how the temporal profiles of the acquisition sequence and the diffusion process can be related to estimate physical parameters.

2.6 Temporal diffusion spectroscopy (TDS)

In restricted diffusion, the Einstein relation $D = \frac{\langle (r-r_0)^2 \rangle}{2t}$ becomes time-dependent, and can be described as:

$$D(t) = \frac{1}{2}\frac{d}{dt}\langle (r - r_0)^2 \rangle \qquad (42)$$

In this case it can be easier to describe the time-dependent diffusivity in terms of the ensemble-averaged *velocity autocorrelation function* C_v:

$$C_v(t) = \langle \boldsymbol{v}_0 \cdot \boldsymbol{v} \rangle \qquad (43)$$

One property of Einstein's random walk was that each step is independent in time, which does not always hold. The velocity autocorrelation is a metric of how correlated a particle's motion is with previous points in time. For instance, in Einstein's assumption of free water where particles have uniform probability in velocity orientation at the smallest finite timepoint, the ensemble-averaged C_v would instantly ($\sim 10^{-11}$ seconds) decorrelate. In ideal flow, particles would have constant (perfectly correlated) velocity. And in the presence of restrictive barriers, the average C_v would fall to negative values: an interaction with a barrier is a reflection, which is negatively correlated with the incident velocity. If a significant fraction of particles reflect before decorrelating, the ensemble average would trend to negative values rather than the zero-valued Gaussian equilibrium. The autocorrelation function can therefore be indicative of the hydrodynamic environment of the system, and diffusion coefficient can be represented in these terms:

$$D(t) = \int_0^t C_v(t')dt' \qquad (44)$$

19

which can be used to define the *temporal diffusion spectrum*:

$$D(\omega) = \int\limits_{0}^{\infty} C_v(t) e^{-i\omega t} dt \qquad (45)$$
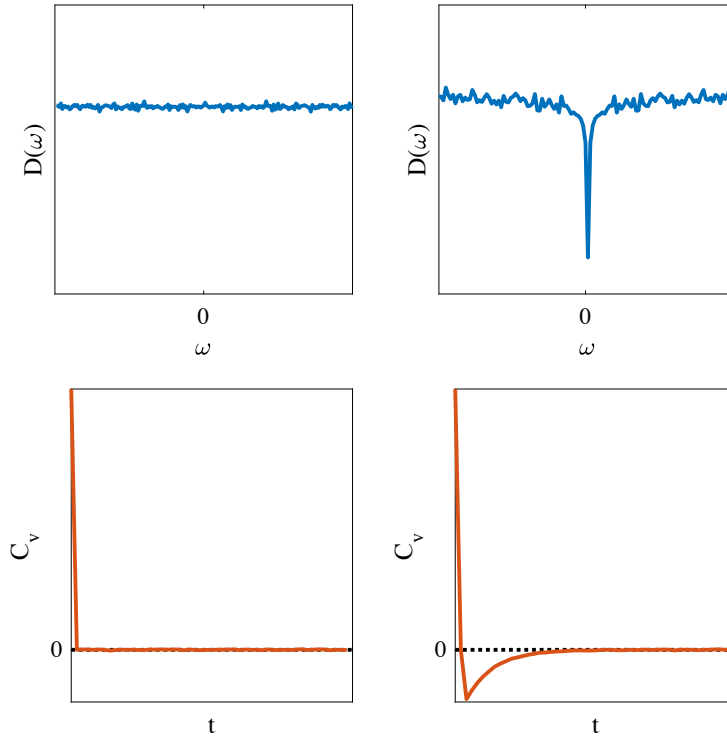
Figure 5. Velocity Autocorrelation Function. 1-dimensional Monte Carlo experiment in free (left) and restricted diffusion (right). The calculated velocity autocorrelation for the two cases (bottom) shows the expected immediate decay to 0 in free water, and the finite recovery from negative value in restriction. The spectral density (top) of free water is uniform while in restricted diffusion it is diminished around 0 Hz.

Probing the diffusion spectrum therefore can give structural information about the water microenvironment. In free water, the spectrum is flat and diffusivity can be measured at any frequency. In restricted diffusion, the DC component approaches zero, as this represents water moving at a constant velocity, which will eventually reach a barrier. It can also be related to the physical properties of the restricted compartments. Janez Stepišnik derived the temporal diffusion spectrum for a sphere of radius R [44]:

$$D(\omega) = \sum_{k}^{\infty} B_k \frac{a_k D_0 \omega^2}{a_k^2 D_0^2 + \omega^2} \tag{46}$$

$$B_k = \frac{2\left(\frac{R}{\mu_k}\right)^2}{\mu_k^2 - 1}$$

$$a_k = \left(\frac{\mu_k}{R}\right)^2$$

where μ_k solves $\mu J'_{\frac{3}{2}}(\mu) - \frac{1}{2}J_{\frac{3}{2}}(\mu) = 0$ and D_0 is the intrinsic diffusivity $\lim_{t \to 0} D(t)$.
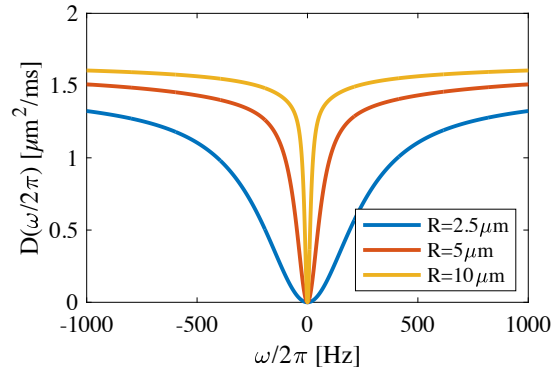
Figure 6. Temporal diffusion spectrum in restricted sphere. Stepišnik's equation is plotted to model diffusion as a function of frequency in spheres of physiologically relevant diameters of 5, 10, and 20μm.

In this way, probing the diffusion spectrum $D(\omega)$ allows one to directly quantify structural physical parameters such as spherical pore radius. In particular to the present work, this means that when modeling a cell as an impermeable sphere, the transient region of $D(\omega)$ directly relates to cell size. In order to measure this using NMR, Stepišnik showed that the velocity autocorrelation is coupled with the dephasing function as:

$$S = S_0 \exp\left[-\frac{1}{2}\int_0^{TE} dt' \int_0^{TE} dt'' \, \boldsymbol{F}^{\mathsf{T}}(t')\langle\boldsymbol{v}(t')\boldsymbol{v}(t'')\rangle\boldsymbol{F}(t'')\right] \tag{47}$$

which is computationally cumbersome, but much simplified in the frequency domain:

$$S = S_0 \exp\left[-\frac{1}{\pi}\int_{-\infty}^{\infty} \boldsymbol{F}^{\mathsf{T}}(\omega)\boldsymbol{D}(\omega)\boldsymbol{F}(-\omega)d\omega\right] \tag{48}$$

21

The spectral profile of the rectangular pulse used in PGSE is given by:

$$F(\omega) = \frac{4G\gamma}{\omega^2} \sin\left(\frac{1}{2}\omega\delta\right) \sin\left(\frac{1}{2}\omega\Delta\right) \qquad (49)$$

where G is the gradient strength. Figure 7 below compares the analytical spectra for $\boldsymbol{F}(\omega)$ and $\boldsymbol{D}(\omega)$ in restricted diffusion. The diffusion spectrum is equally probed for all frequencies in free water. However, in a spherical restriction the correlation is small. Because of the mixing time between pulses in PGSE, this method is sensitive to large molecular displacements, which correspond to high velocity correlation and low frequency. Flow, for instance, is a zero-frequency motion (velocity is fully self-correlated), and this would maximize the phase during the mixing time. As shown above, restrictive barriers cut off the zero-frequency component of motion, and only higher frequencies approach the intrinsic diffusivity.

In order to encode for these frequencies, alternative gradient waveforms are desirable. Oscillating gradient spin echo (OGSE) is a natural fit for this application, since oscillations in the time domain lead to frequency profiles that are mathematically easy to describe, and the rapid dephasing and rephasing cycles yield higher frequencies with less maximum gradient strength. Early applications of OGSE used sine-modulated waveforms [45], which are natural to implement because they are zero-valued at $t = 0$ and therefore the ideal waveform can be achieved. This has a dephasing spectrum of:

$$F(\omega) \approx \frac{2\pi N\gamma G}{\omega_m} \left[\delta(\omega) + \frac{1}{2}\delta(\omega - \omega_m)\right] \qquad (50)$$

where N is the number of cycles and ω_m is the gradient modulation frequency. The approximation in the equation is due to the finite duration of the gradient, and is exact for an infinite cycle case. The finite duration is effectively the infinite case windowed by a rectangular function, which leads to a convolution by a sinc function in the spectral profile. This has a b-value:

$$b = \frac{3}{8}\left(\frac{\gamma G}{\pi N}\right)^2 \left(\frac{2\pi N}{\omega_m}\right)^3 \qquad (51)$$

We can approximate an effective diffusion time[6] of $\frac{3}{8}\tau$, where τ is the period of one oscillation. While this has some density around $\omega = \omega_m$, 2/3 of the diffusion encoding is around 0 and is still sensitive to flow. Alternatively, a cosine waveform has a more ideal spectrum for isolating finite frequencies:

$$\boldsymbol{F}(\omega) \approx \frac{2\pi N\gamma G}{\omega_m}\left[\frac{1}{2}\delta(\omega - \omega_m)\right] \quad (52)$$

which has all of its density at ω_m and an effective diffusion time of $\frac{1}{4}\tau$.
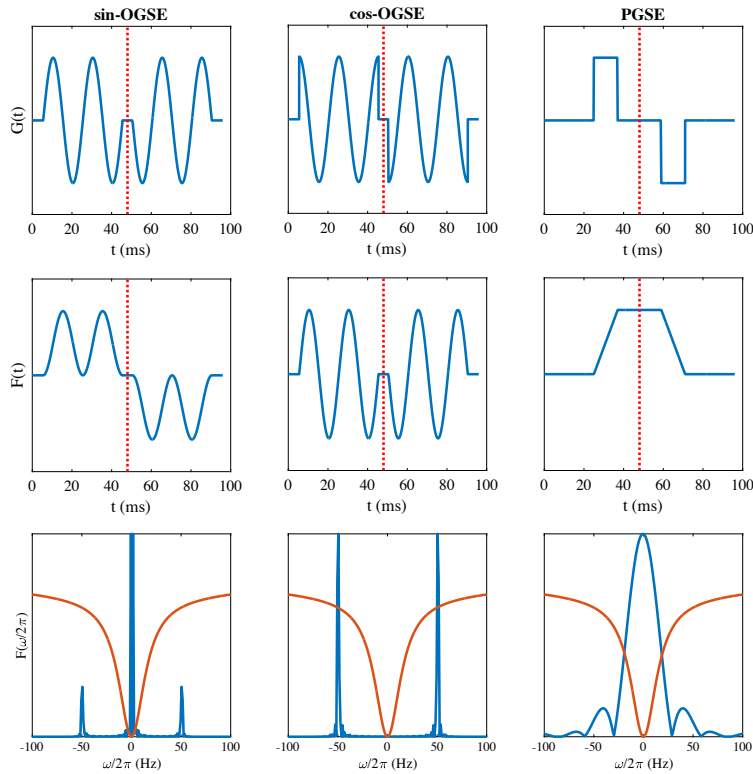
Figure 7. Temporal Diffusion Spectroscopy diagram. (Top) Gradient waveforms for ideal sine- and cosine-modulated OGSE at 50Hz, and PGSE with $\delta = 12$ms and $\Delta = 34$ms. The waveforms

---

[6] There are varying definitions of the *effective diffusion time*, which does not have a consensus for continuous gradient waveforms, as matching effective diffusion times for OGSE and PGSE gives different signals in restricted media [188]. While OGSE is better defined in terms of frequency and PGSE in terms of diffusion time, it is semantically useful to be able to compare them on the same domain. Therefore, for this thesis when referring to OGSE, we will use the 0th order effective diffusion time as defined by Fordham et al. [189]; e.g. 25Hz cos-OGSE has a diffusion time of 10ms.

on the right side of the refocusing pulse (red dashed line) are shown negatively polarized to reflect the effective change in phase. (Middle) The time integral $F(t)$ of the gradient is related to the phase accumulation. The sin-OGSE and PGSE profiles have non-zero moments on each side of the refocusing pulse, which allows phase buildup in molecules experiencing flow. Cos-OGSE, on the other hand, rapidly reverses the net phases such that no accumulation occurs on long time scales. (Bottom) The long-duration gradient power spectrum $|F(\omega)|^2$ is shown (blue) with the analytical diffusion spectrum (red) of molecules in a 20µm sphere. Sin-OGSE has more selective encoding in the frequency domain than PGSE, but the sensitivity to flow is apparent in the density around 0Hz. All cos-OGSE density is at the modulation frequency, which allows it to better attenuate signal in the restricted volume.

The ideal finite cosine function, however, begins at maximum gradient strength, which is not feasible with a finite slew rate. Callaghan and Stepišnik proposed a method *frequency-domain analysis of spin motion using modulated gradient NMR* (FD-MG-NMR) [46], which uses a series of rectangular pulses with interspersed refocusing, effectively giving a discretized cosine waveform. While this improved the selectivity of the dephasing frequency spectrum, it further suffers from high gradient demand and is unsuitable for imaging. Does et al. proposed a double sine OGSE waveform [47], which reverses polarity every other zero-crossing. This cuts off the zero-frequency component by reversing the dephasing polarity in $\boldsymbol{F}(t)$. Parsons et al. [48] proposed using two modified cosine waveforms, which begin with either a sine lobe at twice the modulation frequency or a sine lobe at half the amplitude. These allow a non-zero spectral profile while having a smoother slew rate than a windowed cosine. The smooth double-frequency sine-apodized cosine waveform used by Parsons was further modified for lower gradient requirements by approximating the shape with trapezoidal gradient lobes (Figure 8). In this case, the block lobes encapsulate a larger area (Equation (27)), allowing more dephasing with the same oscillating frequency and same peak gradient strength. This has a practical advantage when gradient strength is the limiting factor on the b-value. Because this tends to be the case in human scanners (e.g. the human scanners in this project had maximum gradient strength 80 mT/m), the trapezoidal PGSE and OGSE waveforms are used in our experimental results throughout this thesis.
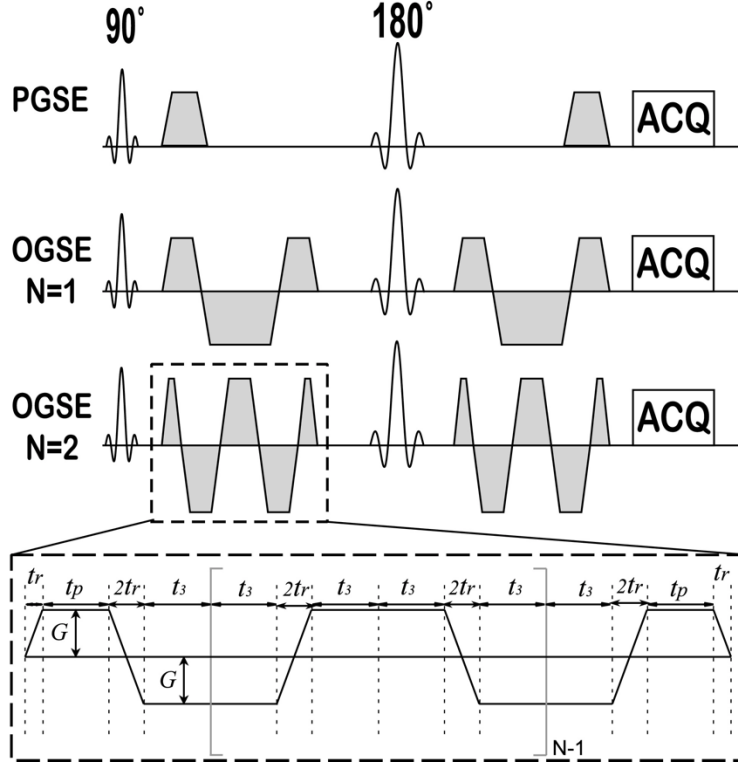
Figure 8. Trapezoidal cosine OGSE. The waveforms used in this project are trapezoidal PGSE (i.e., with a finite rise time) and trapezoidal cosine-modulated OGSE. The 90º and 180º pulses denote the excitation and refocusing, respectively, and the ACQ block denotes the acquisition readout. The expanded waveform in the dashed box parametrizes the wave form with three timing parameters: rise time t_r, plateau time t_p, and extended plateau time $t_3 = t_p + \frac{t_r}{2}$, which balances the area under the extended plateau with the area under the rising gradient. The $N - 1$ bracket denotes the section added or removed to change number of cycles N. Figure from Xu et al. [49].

The b-value for this waveform is calculated as:

$$b = \gamma^2 G^2 \left[\frac{91 N t_r^3}{15} + \frac{8 N t_p^3}{3} + \frac{t_r^3}{30} + 12 N t_r t_p^2 + \frac{46 N t_r^2 t_p}{3} \right] \tag{53}$$

Defining $\phi = -\ln (S/S_0)$, Xu et al. derived an analytical expression for signal attenuation for the trapezoidal-cosine waveform in an impermeable sphere using Equations (46) and (48) [49]:

$$\phi = \gamma^2 G^2 \sum_k \frac{B_k}{a_k^4 D^4 t_r^2} \left\{ \begin{aligned} &4\exp(-a_k Dt_p) - 4\exp(-a_k Dt_r) - 4\exp(-2a_k Dt_r) - 8\exp(-a_k D\Delta) - 12a_k Dt_r + 2\exp[-a_k D(\Delta - t_r)] \\ &+2\exp[-a_k D(\Delta + t_r)] + 2\exp[-a_k D(\Delta + 2t_r)] + 2\exp[-a_k D(\Delta - 2t_r)] - 2\exp[-a_k D(\Delta - t_p)] \\ &-2\exp[-a_k D(\Delta + t_p)] - 4\exp[-a_k D(t_r + t_p)] + 2\exp[-a_k D(t_r + 2t_p)] - 4\exp[-a_k D(2t_r + t_p)] \\ &+4\exp[-a_k D(3t_r + t_p)] - 4\exp[-a_k D(3t_r + 2t_p)] - 4\exp[-a_k D(3t_r + 3t_p)] + 4\exp[-a_k D(4t_r + 3t_p)] \\ &+2\exp[-a_k D(5t_r + 2t_p)] + 4\exp[-a_k D(5t_r + 3t_p)] + 2\exp[-a_k D(5t_r + 4t_p)] - 4\exp[-a_k D(6t_r + 3t_p)] \\ &-4\exp[-a_k D(6t_r + 4t_p)] + 2\exp[-a_k D(7t_r + 4t_p)] + 6a_k^3 D^3 t_r^3 + 8a_k^3 D^3 t_r^2 t_p + 2\exp[-a_k D(\Delta - t_r - t_p)] \\ &-\exp[-a_k D(\Delta - t_r - 2t_p)] + 2\exp[-a_k D(\Delta + t_r + t_p)] + 2\exp[-a_k D(\Delta - 2t_r - t_p)] \\ &-\exp[-a_k D(\Delta + t_r + 2t_p)] + 2\exp[-a_k D(\Delta + 2t_r + t_p)] - 2\exp[-a_k D(\Delta - 3t_r - t_p)] \\ &-2\exp[-a_k D(\Delta + 3t_r + t_p)] + 2\exp[-a_k D(\Delta + 3t_r + 2t_p)] + 2\exp[-a_k D(\Delta - 3t_r - 2t_p)] \\ &+2\exp[-a_k D(\Delta + 3t_r + 3t_p)] + 2\exp[-a_k D(\Delta - 3t_r - 3t_p)] - 2\exp[-a_k D(\Delta + 4t_r + 3t_p)] \\ &-2\exp[-a_k D(\Delta - 4t_r - 3t_p)] - \exp[-a_k D(\Delta + 5t_r + 2t_p)] - \exp[-a_k D(\Delta - 5t_r - 2t_p)] \\ &-2\exp[-a_k D(\Delta + 5t_r + 3t_p)] - 2\exp[-a_k D(\Delta - 5t_r - 3t_p)] - \exp[-a_k D(\Delta + 5t_r + 4t_p)] \\ &-\exp[-a_k D(\Delta - 5t_r - 4t_p)] + 2\exp[-a_k D(\Delta + 6t_r + 3t_p)] + 2\exp[-a_k D(\Delta - 6t_r - 3t_p)] \\ &+2\exp[-a_k D(\Delta + 6t_r + 4t_p)] + 2\exp[-a_k D(\Delta - 6t_r - 4t_p)] - \exp[-a_k D(\Delta + 7t_r + 4t_p)] \\ &-\exp[-a_k D(\Delta - 7t_r - 4t_p)] + 8 \end{aligned} \right\} \qquad (54)$$

where a_k and B_k are as defined in Equation (46). This equation, while cumbersome, depends only on known gradient parameters, intrinsic diffusivity D, and spherical radius R, which allows efficient fitting for intrinsic physical parameters in restricted media. Attenuation for pulsed gradients with finite gradient ramps (i.e., trapezoidal rather than rectangular blocks) is given by:

$$\phi = \gamma^2 G^2 \sum_k \frac{B_k}{a_k^4 D^4 t_r^2} \left\{ \begin{aligned} &2\exp(-a_k Dt_p) - 4\exp(-a_k Dt_r) - 4\exp(-\Delta a_k D) - 4a_k Dt_r + 2\exp[-a_k D(\Delta - t_r)] \\ &+2\exp[-a_k D(\Delta + t_r)] - \exp[-a_k D(\Delta - t_p)] - \exp[-a_k D(\Delta + t_p)] - 4\exp[-a_k D(t_r + t_p)] \\ &+2\exp[-a_k D(2t_r + t_p)] + (4/3)a_k^3 D^3 t_r^3 + 2a_k^3 D^3 t_r^2 t_p + 2\exp[-a_k D(\Delta - t_r - t_p)] \\ &+2\exp[-a_k D(\Delta + t_r + t_p)] - \exp[-a_k D(\Delta - 2t_r - t_p)] - \exp[-a_k D(\Delta + 2t_r + t_p)] + 4 \end{aligned} \right\} \qquad (55)$$

The general analysis using the frequency spectrum to characterize diffusion is called *temporal diffusion spectroscopy* [48]. A brief review of how this has been extended to quantitative fits of cell size *in vivo* is provided in the next chapter, as well as how diffusion time dependence can be leveraged as a cancer biomarker. The temporal diffusion spectroscopy framework, particularly Equations (54) and (55), also provides the basis for the simulation results of intracellular signal shown throughout this thesis.

CHAPTER 3

Size-Selective Imaging using Filters via diffusion Time

Chapter 2 described how the diffusion process and measurements are dependent on restrictive barriers in a medium. We saw that analysis on the temporal frequency domain allows for a quantitative relation between the signal and restriction size. The objective of this chapter is to show how these principles can be extended into brain cancer imaging in a practical manner. Section 3.1 reviews the effects of *in vivo* tissues on diffusion measurements. This includes how conventional ADC and DTI are affected by changes in tissue microstructure, and how time dependent diffusion has been used to glean cell size information in extracranial cancer imaging. Section 3.2 describes how the complexity of brain tissue presents a challenge to extend those methods into brain cancers. Section 3.3 provides an alternative method to sensitize contrast to cell size, illustrating the theoretical basis for the method via simulated signal. This method is termed Size-Selective Imaging using Filters via diffusion Time (SSIFT). Section 3.4 provides methodology for best implementation of SSIFT based on simulation and preliminary results in healthy subjects and a tumor-bearing patient.

3.1 Cellular imaging in tumors with diffusion MRI

In Chapter 2 we saw that water inside restricted compartments yields a lower ADC. In biological tissues, ADC shows an inverse relationship with intracellular volume fraction, which changes with cellularity [24] or cellular swelling [50]. While ADC has been shown to decrease in tumors due to the increase in cellularity [51,52], this trend is not universal for all cancer lines, as some are more diffuse [53]. Additionally, it may not be specific enough to distinguish malignant and benign lesions [20]. To solve the lack of diagnostic accuracy in ADC, time-dependent diffusion has been applied to use cell size information. This section highlights some recent efforts to quantify cellular microstructural parameters for cancer imaging.

The use of restriction size information for characterizing cancers is motivated by particular features of cell size and intracellular volume fraction in cancer. The roles of cell size in cellular function are many. Neuronal size ensures the cell is able to communicate with the appropriate

27

networks [54]. Hormone production in glandular cells is correlated with size [55]. To preserve such functions, cell size is controlled through a combination of external growth factors and self-regulation. Cell size plays a role in progression through the cell cycle [56], and in some cases is the rate-limiting factor for propagation [57]. These checkpoints to the cell cycle serve to both maintain cell size heterogeneity and limit proliferation. Cancer displays a breakdown in regulation of both cell size and count, correlating with tumor grading [54]. In addition, cell size can be markers of tumor response to therapies, as apoptosis displays cell shrinkage [58] and successfully targeted immunotherapy leads to small immune cell infiltrates [59]. The ability to detect cell size *in vivo* may therefore be useful for cancer diagnostics.

Two cell size methods have been successfully implemented in humans: *imaging microstructural parameters using limited spectrally edited diffusion* (IMPULSED) [30,60,61], which has been implemented in human breast [30] and prostate [62] cancers, and *vascular, extracellular, and restricted diffusion for cytometry in tumors* (VERDICT) [29,63,64], which has been implemented in prostate cancer. Both methods use multicompartment models of signal to extract cell size. The primary difference between the models is in their intracellular modeling resulting from the use of different pulse sequences. VERDICT has only been applied using PGSE to fit cell size, while IMPULSED has mixed PGSE and OGSE data. Both methods were tested in prostate cancer, and IMPULSED slightly outperformed VERDICT in half the scan time. This may be due to the additional information offered by probing short diffusion times with OGSE. While these methods have been successfully applied in patients with breast and prostate cancer, where cells generally meet the modeling assumption of isotropic spheres. Translation to the brain, however, may require modification to accommodate the considerably different microstructure, which is described in the following section.

3.2 dMRI in brain tissue

The brain is far from monolithic and has many heterogeneous substructures, but for simplicity we will group brain tissues generally as white matter (WM), gray matter (GM), and cerebral spinal fluid (CSF). These tissues present various challenges to diffusion imaging in the brain, such as anisotropy and heterogeneous cell sizes. This section will instead focus on human implementation and challenges in diffusion MRI of the brain.

28

Both healthy and dysfunctional white matter have been popular subjects of study using diffusion MRI due to the high anisotropy of water diffusion in myelinated axons [65,66]. In regions where axons have high coherence, this anisotropy is detectable with conventional DTI. In cases with lower macroscopic coherence caused by fiber crossings, high angular resolution acquisitions can either fit multiple orientations (e.g., Spherical Deconvolution [67–69] or q-Ball Imaging [70]) or model the directionally averaged signal to remove the effect of anisotropy altogether [68,71,72]. Because isotropic models such as IMPULSED use only 3 orthogonal directions for each combination of b-value and diffusion time [49,62], addressing anisotropy may require additional directional sampling and cost scan time.

Cortical gray matter tends to have less anisotropy on the voxel scale (~2-3mm) than white matter [73], though on the 100s of µm scale FA varies by cortical layer [74], and on the cellular microstructural level can be highly anisotropic [71]. Despite the relative isotropy, GM still poses a challenge to cell size imaging due to the range of cell sizes. Most of the volume is intracellular, comprising dendrites and axons with 0-5µm diameters (medians less than 1µm) [75], glia ranging from 1-10µm [76], and neurons with 5-35µm diameter bodies [76,77]. Cell size quantification by fitting a mean size may therefore lack specificity due to this broad range.

Because of the heterogeneity of cell sizes and the problem of anisotropy, cancer imaging using time-dependent diffusion has met with little success in the brain. One study applied VERDICT for grading gliomas [78], but it does not represent an ideal use of cell size estimation in the brain for a few reasons. First, the analysis was restricted to only the tumor ROI and the processing time was ~20min. Whole brain fitting may be desirable for some applications, which may be limited by processing time and this data does not report how well VERDICT performs in extra-tumoral tissue. Secondly, while the acquisition was fast (5.5min), a longer protocol applied on the same subject (~50min) yielded a cell size differing by more than one standard deviation, indicating some accuracy may be sacrificed in the shortened scan time. Finally, while the study found cellularity to have diagnostic accuracy, cell size fitting yielded the same values in low- and high-grade gliomas (6.7±1.2 vs. 6.8±2.3µm). It is unclear whether this cell size estimation could have been improved with shorter diffusion times achievable with OGSE, as these sizes are much smaller than the characteristic length of PGSE diffusion times.

3.3 Size-Selective Imaging using Filters via diffusion Time (SSIFT)

Due to the challenges of quantitative models in brain tissue, we turn toward an alternative strategy to generate cell size-based contrast. Because a characteristic of cancer is deregulated proliferation of progenitor cells, and in the case of metastases these cells differ in size from most cells in the healthy brain, parsing cell count from cell size may not be necessary in order to classify tumors. We hypothesize that a simple imaging metric sensitive to both cell density and size is the signal dependence on diffusion time itself. Figure 9 depicts simulated signal using two diffusion times over a range of cell sizes, with signal simulated from Equations (54) and (55). While the diffusion weighted signal decreases monotonically with size, the plotted residual has a maximum at 18.5µm and minima at the extremes. This may have an advantage in brain tissue, as not only will the residual be sensitive to tumor cells (10-20µm), but it will suppress small restriction sizes (axons and glia) and unrestricted water (edema or CSF).
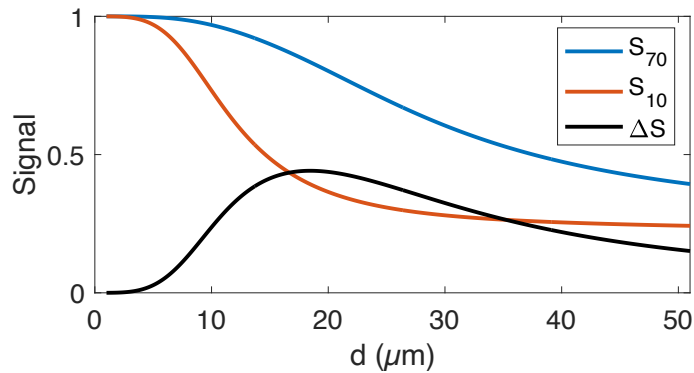
Figure 9. Signal dependence on t_{diff} and cell size. Intracellular signal simulated by temporal diffusion spectroscopy for a PGSE sequence with 70ms t_{diff} (blue) and an OGSE sequence with 10ms t_{diff} (red). The difference in signals at two diffusion times (black) alters the curve of output sensitivity to restriction size, having a maximum at finite sizes rather than a monotonic decrease with size.

The remainder of this chapter formalizes the methodology of signal dependence on diffusion time. We term this method *size-selective imaging using filters via diffusion time* (SSIFT).

The incremental area under the curve (iAUC). First we define the output metric of SSIFT. While there are multiple ways the signal dependence on diffusion time could be defined quantitatively

(e.g., the difference in signal ΔS, shown above, or the derivative $\Delta S / \Delta t_{diff}$), it may be desirable to incorporate multiple diffusion times. We therefore use the *incremental area under the curve*, or iAUC, which is the cumulative difference between sampled signals. This is illustrated geometrically in Figure 10a, and for measurements M the iAUC is quantified as:

$$\text{iAUC} = \sum_{m=2}^{N_{tdiff}} \frac{t_{diff,m} - t_{diff,m-1}}{2\left(t_{diff,N_{tdiff}} - t_{diff,1}\right)} \left[M\left(t_{diff,m}\right) + M\left(t_{diff,m-1}\right) - 2M\left(t_{diff,1}\right)\right] \qquad (56)$$
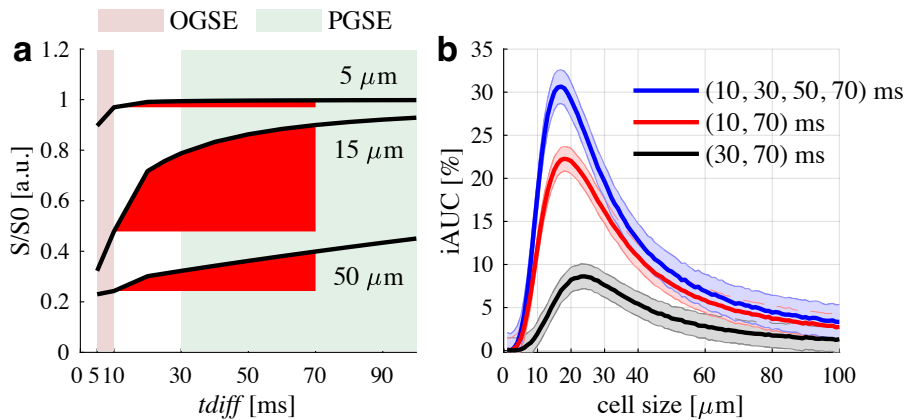
Figure 10. SSIFT iAUC definition. (a) Simulated dependence of dMRI signals on cell size and diffusion time t_{diff}. The red incremental area under curve (iAUC) shows a strong dependence on cell size. Colored backgrounds represent typical measurable t_{diff} ranges in clinics. (b) Normalized iAUC with three different combinations of t_{diff} values may serve as a filter to selectively enhance sensitivity to typical cancer cell sizes (i.e., $10 - 20$ μm) in brain tumors. Solid lines and shaded areas indicate means and standard deviations of 500 runs with a signal-to-noise ratio of 20.

Figure 10b simulates the iAUC for three sets of diffusion times: a 4-point mixture of OGSE and PGSE, a 2-point iAUC mixing OGSE and PGSE (equivalent to $\frac{1}{2}\Delta S$), and a 2-point iAUC with only PGSE. Two effects are seen when varying diffusion time: the height of the output and the window/level of the filter. The 4-point combination shows the highest output, and is 8.4 times higher than the PGSE-only maximum and is 1.4 times higher than the 2-point . The FWHM of the 4-point curve spans 9.3-36.1 μm and is similar to the 2-point curve, while the PGSE-only curve spans 14.9-50.8 μm. A comparison of the schemes for maximizing contrast between pathologies

will be done in Chapter 4, but this simulation illustrates the importance of incorporating short diffusion times with OGSE and that sampling intermediate times can improve intracellular sensitivity.

Although Figure 10 shows the basis for size-selectivity in intracellular water, it is not trivial that this will generate contrast in the brain due to the anisotropic microstructure and multiple tissue compartments. The remainder of this section describes how this can be accounted for by considering the effect of each compartment separately.

Diffusion modeling. Typically, diffusion MRI signal models treat measured signal as a linear combination of signals arising from each compartment:

$$S = \sum v_i S_i \tag{57}$$

where i indexes the compartment (e.g., extracellular, intracellular). The signal fraction[7] v_i is proportional to both proton density and relaxation:

$$v_i \propto \frac{\rho_i}{\rho} \frac{e^{-TE/T2_i}}{e^{-TE/T2}} \tag{58}$$

and is subject to $\sum v_i = 1$. Here $T2_i$ is the transverse relaxation time of the ith compartment and $T2$ is voxel-averaged.

We can separately consider three main categories of diffusing water molecules in brain tissues:

1. *Free water* is unrestricted such as in cysts or CSF that has a constant diffusivity D_{free} of 3.05 μm^2/ms at body temperature (37°) [79].
2. *Hindered diffusion* is water outside of cells that is not confined within a cell but encounters restrictive barriers that reduce its RMSD, and is described by $D_h < D_{free}$ and may have anisotropy [80].

---

[7] *Volume fraction*, which is approximately $\frac{\rho_i}{\rho}$, is often used to mean *signal fraction*, since v_i is the closest surrogate to physical volume in the model. This substitution is tempting because it carries physiological meaning, but is not strictly speaking correct due to relaxation. Terminology such as *apparent volume fraction* may be a reasonable compromise to capture the physiological interpretation of v_i while acknowledging the bias from relaxation effects.

3. *Restricted diffusion* is intracellular water, as was considered in Chapter 2. In the brain this comprises dendrites, axons, neuronal soma, glia, and cancer cells. Because of the anisotropy of dendrites and axons, locally these can be modeled as cylindrically symmetric compartments with longitudinal diffusivity $\lambda_{||} = \lambda_1$ and transverse diffusivity $\lambda_\perp = \lambda_2 = \lambda_3$, where λ_i is the ith eigenvector of the diffusion tensor. These compartments are illustrated in Figure 11.

The signals from free S_{free}, hindered S_h, and restricted S_r compartments are then combined as:

$$S = v_{free}S_{free} + v_h S_h + v_r S_r \qquad (59)$$

where the restricted compartment is:

$$v_r S_r = v_{axon}S_{axon} + v_{neuron}S_{neuron} + v_{cancer}S_{cancer} \qquad (60)$$
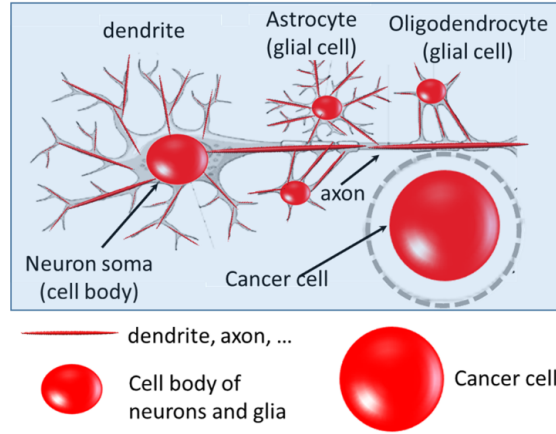
Figure 11. Diagram of restricted diffusion in brain tissue. Diagram of three categories of restricted diffusion based on the local diffusion environment: (1) dendrites, (2) normal cells (neuron and glia cell bodies), and (3) cancer cells. Local diffusion tensors (red ellipsoids) are overlaid on diagram of brain and cancer cells.

Directional averaging. The hindered and axonal/dendrite compartments are anisotropic on a local scale (i.e., within a ~10s of μm radius around the cell). It has been shown that the arithmetic mean (or powder-average) of signal from multiple diffusion encoding gradient directions removes the directional dependence and can be modeled as [72]:

$$M(t_{diff}) = \sum_i^{N_{compt}} v_i \exp\left[-b\lambda_{\perp,i}(t_{diff})\right] \frac{\sqrt{\pi}\,\text{erf}\left(\sqrt{b(\lambda_{||,i}(t_{diff}) - \lambda_{\perp,i}(t_{diff}))}\right)}{2\sqrt{b(\lambda_{||,i}(t_{diff}) - \lambda_{\perp,i}(t_{diff}))}} \qquad (61)$$

Equation (61) describing the time-dependent directionally averaged signal M depends only on signal fraction v and the local diffusion tensors of each compartment i. For isotropic compartments ($\lambda_\perp = \lambda_{||}$) this reduces to the usual form $S_i = v_i e^{-bD_i}$. Operating on the directionally independent space is ideal in brain cancer imaging because identifying the isotropic cancer compartment does not require information on tensor orientations.

Compartment dependence on diffusion time. The signal fractions are tissue parameters that do not change with t_{diff}. D_{free} is constant with diffusion time, and the dependence of $\lambda_{\perp,h}$ and $\lambda_{||,h}$ on t_{diff} have been reported to be small. For example, a brain DTI study showed that FA and MD are independent of t_{diff} using PGSE [81]. MD dependence on t_{diff} has also been reported to be small using OGSE with t_{diff} down to 10 ms [82,83]. This suggests the dependence of the local tensors on t_{diff} is mainly due to restricted diffusion with the t_{diff} range used in the current work.

For restricted diffusion, compartments show t_{diff} dependence based on their sizes, which were highlighted in the previous section. For tensors in dendrites and axons, $\lambda_\perp$ is approximately 0 due to very small diameters, and $\lambda_{||}$ is t_{diff} independent due to the long main axes. The influences of fiber organization such as undulation, crossing, and dispersion at even longer length scales have shown to be minimal after directional averaging [84]. Neuron cell bodies have sizes that span across the SSIFT filter and S_{neuron} is non-negligible, but the volume fraction is small (less than 20% [76]) so the signal fraction v_{neuron} tampers its effect on the measurement. Tumor cells of sizes 10-20 µm with higher volume fraction and a tighter distribution of sizes would therefore contribute appreciably more than normal tissue, giving iAUC $\cong$ iAUC$_{cancer}$. This is the key hypothesis for applying SSIFT to tumors, which is the subject of Chapter 4.

Normalization. Signal at different diffusion times needs to be normalized to a common intensity in order to be comparable. In Figure 10, the single-compartment intracellular signals are normalized to a non-diffusion-weighted signal (S_0) to generate the iAUC. However, in practice a measurement of S_0 will often have multiple compartments from different tissues, extracellular water, and a distribution of cell sizes. While the iAUC selectively filters out the non-cancer compartments, the measured S_0 will be impacted by these compartments in their varied T2-

weighted signal. Voxelwise normalization of iAUC by S_0 would therefore give the undesirable result:

$$\frac{iAUC}{S_0} \cong \frac{iAUC_{cancer\ cell}}{S_{0,free/edema} + S_{0,dendrite/axon} + S_{0,cancer\ cell} + \dots} \qquad (62)$$

This can compromise the cell size-weighted contrast of the iAUC, since e.g. edema and white matter may have T2 values different than primary and metastatic tumors in humans [85]. To normalize signal to be comparable between intra- and inter-subject volumes, a global normalization to the median S_0 in non-leasional white matter is used; this strategy is employed by Raffelt et al. to avoid partial voluming effects [86]. This way, inter-voxel variation from T2-weighted signals separate from the iAUC are eliminated.

3.4 Practical implementation of SSIFT

Translating time-dependent diffusion imaging to the brain also has practical challenges in the acquisition design that can have an effect on the SSIFT output. For instance, differences such as eddy currents between OGSE and PGSE sequences can have residuals propagating to the parametric map. Additionally, some processing factors have special considerations in SSIFT, such as the effects of noise on whether to normalize by S_0, and will be noted in detail. While Section 3.3 detailed the theoretical processing for SSIFT, in this section we provide theoretical and practical choices specific to human imaging. This includes optimization of the diffusion times based on human gradient constraints, simulation to detail the effects of noise on the SSIFT map with and without normalization, and the observations on the effect of acquisition and processing differences between PGSE and OGSE. The end of this section provides a step-by-step protocol listing both the special considerations of SSIFT and other processing (e.g. Gibbs ringing or susceptibility correction) that is typical for diffusion imaging. The patient data available to this project were limited, and so the data in this section is mostly from healthy subjects used for assessing factors such as image distortion correction. The parametric map for the test patient data is shown in Figure 12 below.
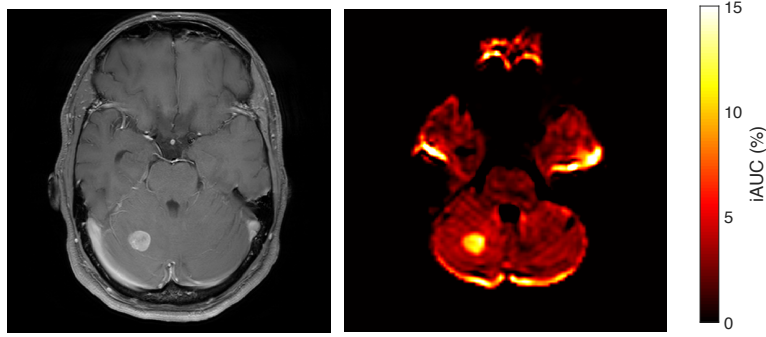
Figure 12. SSIFT patient data. An example patient data used to test contrast in processing schemes. The tumor is a non-small cell lung carcinoma metastatic to the right cerebellum. The lesion is conspicuous on Gd-enhanced T1-weighted image (left) and SSIFT (right).

Gradient parameters. The b-value and echo times of both the PGSE and OGSE sequences are matched to isolate the effects of diffusion time on signal. The limiting factor for both of these is the OGSE gradient scheme, requiring a long duration and high gradient strength. For instance, a t_{diff} of 10 ms (or f=25Hz) can be achieved with a single-cycle trapezoidal cosine waveform of δ=40 ms and Δ=46 ms, giving a total preparation time of 86 ms. A PGSE sequence with δ=12 ms has a maximum Δ = 74 ms to match this. With these timing parameters and a b-value of 1000 s/mm^2, the OGSE sequence has maximum gradient strength of 75 mT/m and PGSE 40 mT/m. Figure 13 shows five SSIFT filters with varying OGSE diffusion times and maximum b-value set by a fixed gradient strength. To account for the varying preparation time, the simulated signal is T2-weighted with a T2 of 100 ms. For simplicity, the iAUC is calculated with just the OGSE signal and one PGSE signal with δ=12 ms and an adjusted Δ to match the preparation time. The 10 ms and 12.5 ms sequences generate the highest sensitivity. The 12.5 ms sequence has 4% higher T2-weighted iAUC, but has two disadvantages that may not be worth the marginal increase: (a) the longer TE (+20 ms) can lead to more severe distortions and (b) a b-value at or less than 1000 s/mm^2 prevents bias in ADC estimation [87], and it may be desirable to perform ADC fits on the SSIFT data (Chapter 5). We therefore use the 10 ms OGSE sequence and match it with a 70 ms PGSE in the studies described in this thesis. The animal data also include 30 and 50 ms data.
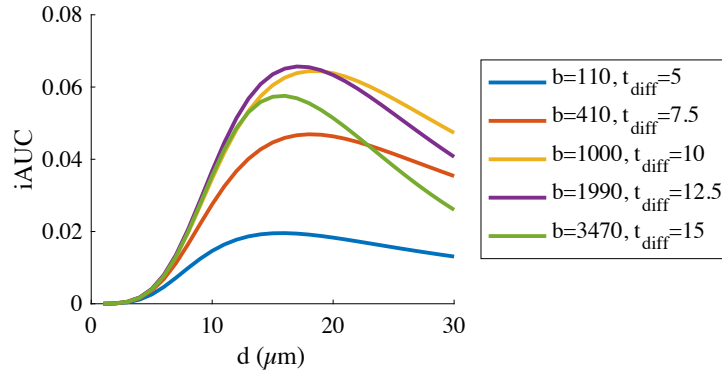
Figure 13. SSIFT gradient strength-limited sequences. Five T2-weighted iAUC curves are generated with varying protocols limited by the OGSE gradient strength. Units on b and t_{diff} are s/mm^2 and ms, respectively. The 10 and 12.5 ms sequences had the highest maximum iAUC.

Signal Noise. Noise in MRI is typically modeled by a Rician distribution, which with sufficiently high signal-to-noise ratio (SNR) approaches a Gaussian distribution with standard deviation σ [88]. In this case, the propagation of errors yields a noise level of 2σ in an image subtraction, such as a 2-point SSIFT. SSIFT processing involves taking the spherical mean of the data, which reduces the variance. A recent denoising strategy was developed by Veraart et al. to mitigate noise in modalities with redundant information, such as diffusion MRI with many directions [89] or T2 relaxometry with many echo times [90]. This offered only marginal benefit to the contrast-to-noise ratio (CNR) of tumor to normal tissue (1-4%); however, since the denoising method corrects the individual diffusion-weighted images and has little processing time, it is useful to include when also fitting the diffusion tensor from the same data volume. Figure 14 demonstrates the qualitative effect of reducing the number of directions. Additionally, Section 3.3 detailed two normalization strategies for SSIFT (global and voxelwise division by S_0), and argued that global normalization reduces bias in iAUC induced by T2 differences between compartments. Global normalization also reduces variance in iAUC, as noise in the S_0 data propagates into the iAUC otherwise. Figure 15 demonstrates this for the subtraction between simulated OGSE and PGSE signal.
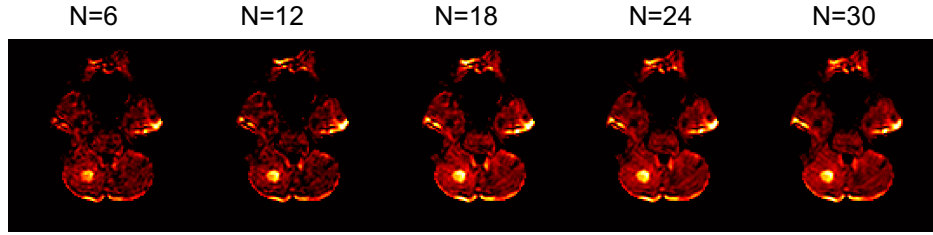
Figure 14. Influences of the number of gradient directions on SSIFT iAUC images. Visual contrast between tumor and normal tissue is high with a reduction in the number of directions.
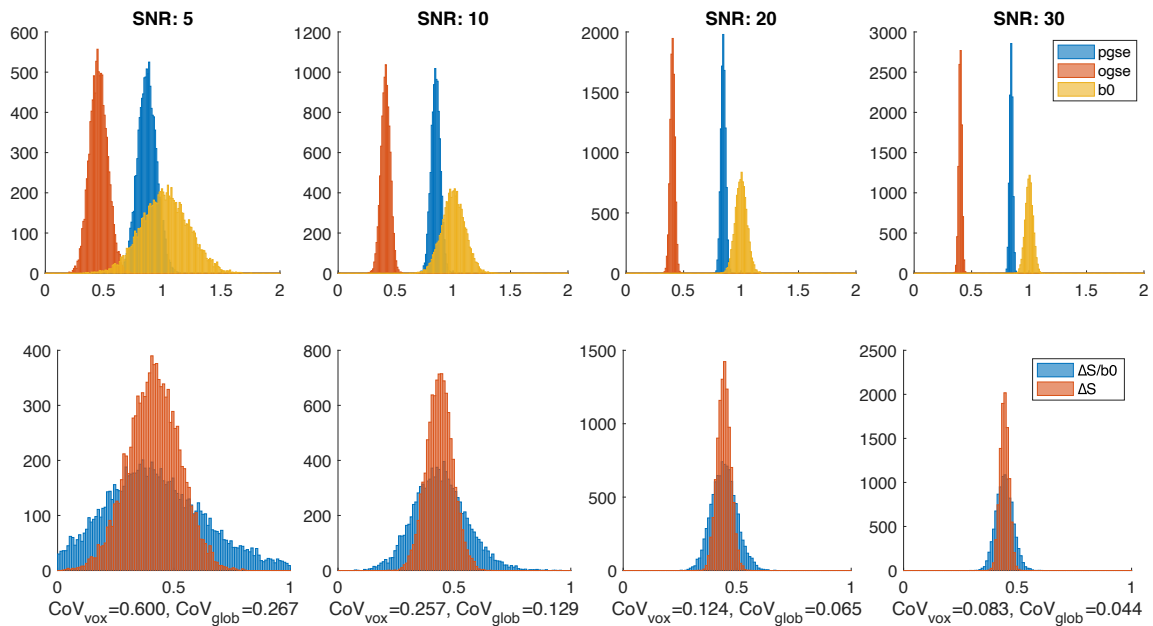
Figure 15. Simulated effect of S_0 normalization. Signal from 18μm cells was simulated using PGSE and OGSE schemes of 70 and 10ms diffusion times, respectively. Rician noise was added for S_0 SNR levels from 5 to 30. The voxel intensity histograms from the signal are shown above and the calculated ΔS is shown below with (blue) and without (red) normalization of the S_0 signal. The Coefficient of Variation for voxelwise (S_0) normalization (CoV_{vox}) is twice that of global normalization (CoV_{glob}).

Eddy currents. Fast changes in the magnetic field can induce electrical currents in a conductor, such as the MRI hardware. In the case of steep gradient ramps, this can alter the ideal waveform

[91]. In diffusion-weighted imaging, this is especially problematic. First, ideal diffusion-sensitizing gradients are needed for accurate ADC estimation. Steep ramps in these gradients can cause deviation in the nominal b-value, leading to estimation errors. Second, phase buildup from non-ideal diffusion gradients can lead to image distortions. Third, clinical applications of diffusion MRI typically use echo planar imaging (EPI), which require fast gradient switching during readout and add additional eddy distortions. Moreover, this may be especially problematic in OGSE, which uses high gradient strengths and has more ramps in its waveform which can induce eddy currents. To address the particular problems of eddy currents in diffusion imaging, Andersson and Sotiropoulos developed a correction algorithm that is now commonly used [92]. However, this method may not correct PGSE and OGSE data to the same extent [93], which is particularly problematic for SSIFT in which any discrepancy between the PGSE and OGSE acquisitions will propagate to the output iAUC. Figure 16 shows visible directional bias in the uncorrected OGSE image, but is mostly mitigated using a correction algorithm.
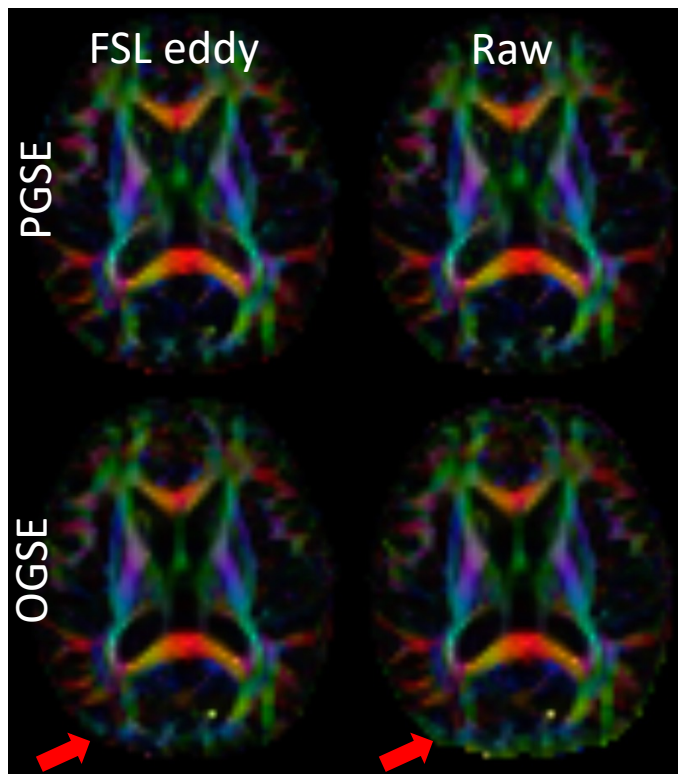
Figure 16. Bias from eddy currents. A directional bias in the color-encoded FA map is indicative of eddy currents. This can be seen on the edge of the anterior-posterior phase-encoding direction (red arrow). The effect is more severe in OGSE than in PGSE. Eddy current correction reduces this effect.

Interestingly, the correction is less effective in oscillating gradients when using a multiband acceleration. This is illustrated in Figure 17 with a multiband factor of 2. The net effect is a bright band along the edges of the phase encoding direction. This effect occurs with either anterior-posterior or left-right phase-encoding directions. While multiband acceleration can reduce scan time, it would seem to cost image quality.
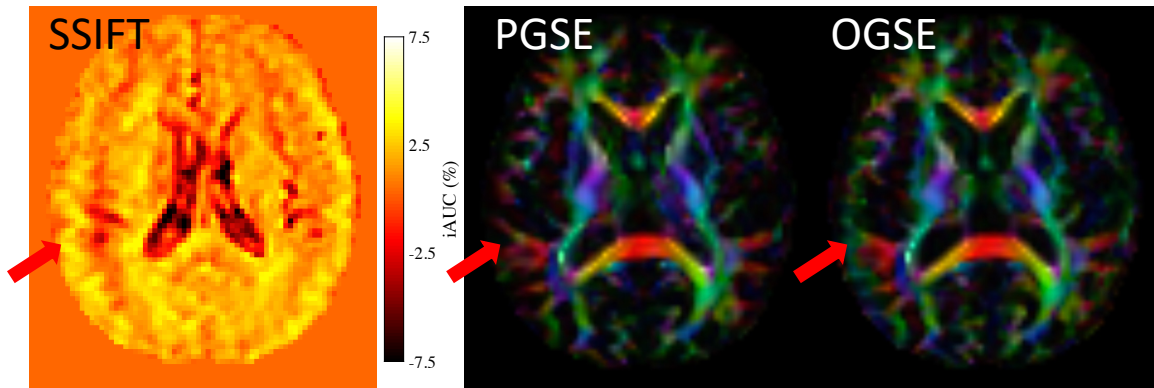
Figure 17. Multiband artifacts. Images were from data acquired with a left-right phase-encoding direction and multiband factor of 2. The left image shows a SSIFT map with a bright edge in the phase-encoding direction. The color-coded FA maps (right) show a residual bias in OGSE along this edge. The residual signal due to this bias may be the cause of heterogeneity in SSIFT.

Processing Pipeline. To summarize this section, the general workflow of SSIFT follows.

1. <u>Acquisition</u>. With a maximum gradient strength ~80 mT/m, simulation a b=1000 s/mm^2, 25 Hz trapezoidal cos-OGSE sequence (one cycle, δ=40 ms, Δ=52.7 ms) is optimal for sensitivity to cancer cells. A PGSE sequence with δ=12 ms and Δ=74 ms is used as the long diffusion time data. Additional diffusion times with Δ=54 and 34 ms are used in addition to these for a 4-point scheme in Chapter 4, but their added value in human cancers is currently unknown. CNR between tumor and normal tissue saw improvement in one tumor subject up to 24 directions. One b=0 image is needed for normalization, and is paired with a b=0 image with a reverse phase-encoding direction for distortion correction.

2. <u>Preprocessing</u>. Denoising is performed using the MRTrix3 *dwidenoise* function [89,94]. Gibbs correction uses *mrdegibbs* in MRTrix3 [95]. Susceptibility and eddy distortion correction were done with *topup* [96] and *eddy* [92] in FSL [97,98].

3. Normalization. A white matter mask is first determined using the intersection of a brain mask and an FA > 0.4 threshold. This is measured with DTI using MRTrix3 functions *dwi2tensor* [99] and *tensor2metric*. We then set the median b=0 value in white matter to 1000 [86] and scale the diffusion weighted volumes by the same amount.

4. iAUC calculation. The spherical mean of each diffusion-weighted image (excluding the b=0 image) is calculated. The time-dependent mean measurements $M(t_{diff})$ are used with Equation (56) to calculate the iAUC.

This chapter detailed how time-dependent diffusion can be leveraged to generate what we hypothesize is cell size-selective contrast. The processing pipeline provided is used in the following chapter to test this hypothesis in preclinical models.

CHAPTER 4

New insights into differentiation of brain tumors and radiation necrosis using selective cell size
MRI

The previous chapter described in detail a new method, SSIFT, which generates a map of signal dependence on diffusion time. However, the biophysical interpretation of this data is not trivial. In this chapter, we perform a set of experiments to better inform how the SSIFT iAUC should be interpreted in cancer imaging. Additionally, Chapter 1 described the clinical need of differentiating radiation necrosis from recurrent tumor. This chapter tests whether SSIFT generates suitable contrast to address this problem. This is done through four sets of experiments. The first details computer simulations to investigate how SSIFT iAUC compares to ADC and ΔADC (i.e., the difference in ADC measured at two diffusion times). Since ADC is thought to relate to cellularity, as described in Section 3.1, this simulation shows how the SSIFT sensitivity to cellularity is cell size-selective, suppressing effects fractions of small cells. The second is an *in vitro* imaging study to demonstrate that SSIFT is sensitive to various cancer cell lines and is insensitive to smaller cells. This both shows a correlation of SSIFT iAUC with cell size in the regime of cells < 20 μm, as well as cataloguing the cancer lines that show SSIFT sensitivity when normalized for volume fraction. We include the three most common human brain metastases (lung, melanoma, and breast) to motivate future human studies. Third is a study imaging *in vivo* rat models of radiation necrosis and tumor. Histology from these subjects was assessed for cell count to demonstrate that SSIFT iAUC is sensitive to the density of nucleated cells. The ROI-averaged values in tumor and radiation necrosis are compared to demonstrate that SSIFT has potential to meet this clinical need. Finally, we show proof-of-concept images in human subjects with a non-small cell lung carcinoma metastasis, a melanoma metastasis, and radiation necrosis following radiotherapy for a renal cell carcinoma metastatic to the frontal brain. These results demonstrate that SSIFT is sensitive to tumor and immune to etiologies such as peri-tumoral edema and radiation necrosis.

4.1 Introduction

Metastatic brain tumors comprise some of the most challenging malignancies to manage in terms of patient prognosis [100]. Treatments of brain tumors generally comprise a combination of surgical resection, radiation therapy, and/or chemotherapy. Stereotactic radiosurgery (SRS) in particular has shown remarkable results in local tumor control [101]. These therapies tend to be palliative, however, with the goal of extending survival on the scale of months to a few years. Tumor recurrence is common in these cases and may require re-treatment [102]. Patient care is further complicated by treatment-induced injuries to the surrounding healthy tissue. Accurate characterization of tissue as either tumor progression or injuries to normal tissue is crucial to determine follow-up treatment, but tissue biopsy has high risk to patients [11], and conventional *in vivo* diagnostic methods can fail to make accurately classify the lesions [103]. New strategies for identifying brain lesions *in vivo* with increased diagnostic specificity could therefore improve the clinical care of patients with brain tumors.

Magnetic resonance imaging (MRI) is sensitive to many properties of the tissue microenvironment and can be tailored to selectively target important pathological features. In particular, diffusion imaging is dependent on the geometric structure of tissue on a micron scale. As seen in Chapter 3, this has been shown to be sensitive to cell density [24], which may be a defining characteristic of a tumor. Brain tissue, however, is highly heterogeneous in microstructural geometry. Normal tissues comprise axons, glia, and neurons which span broad ranges in size [76], and non-malignant lesions such as edema or radiation-induced necrosis can mix in fractions of free water, autoinflammatory cells, and cellular swelling. The complexity in water compartment fraction, restriction size, and anisotropy can lead to a lack of specificity using conventional diffusion imaging to identify tumors [28]. In such cases, cell size may be a useful alternative characteristic to define a tumor, particularly metastases from tissues of origin with larger cells.

In this study, we propose that a new type of diffusion processing method, titled SSIFT: Size-Selective Imaging using Filters via Diffusion Time, . By altering the diffusion time in the acquisition and filtering the signal by this dependence, we may gain specificity to cell size. Unlike

43

conventional diffusion imaging methods, which are sensitive to the density of all restrictions in a tissue, the hypothesized SSIFT output only accepts contribution from an intermediate range of sizes similar to those in cancer cells. This generates a cell size-selective contrast which, we hypothesize, can be a better discriminator between tumors and other etiologies.

4.2 Methods

SSIFT protocol. Although more t_{diff} values may further enhance the selective sensitivity to large cancer cells as shown in Figure 10, this would increase the total scan time which is not desirable in clinical practice. Therefore, a minimum of two t_{diff} values, 10 ms and 70 ms obtained using OGSE and PGSE, respectively, were used throughout the studies in this work. All dMRI acquisitions used b = 0 and 1000 mm²/s with 32 gradient directions. For PGSE, gradient duration δ = 12 ms and gradient time interval Δ = 74 ms. For OGSE, δ = 40 ms, Δ = 52.4 ms in humans and 45 ms in rats, number of oscillating cycles = 1, Details of the implementation of OGSE sequences on both animal and human scanners have been reported previously [30]. Additional dMRI measurements using PGSE acquisitions with Δ = 54 and 34 ms were also performed in the animal study.

Computer simulations. Simulated intracellular signal using Equations (54) and (55) and Gaussian extracellular signal were generated to investigate the ability of SSIFT to differentiate brain tumors from normal tissues with mixed tissue compositions. Tumors and brain tissues were modeled as packed spherical cells with larger (16 μm) and smaller (8 μm) cell sizes, respectively [61]. The intracellular diffusivity of both cell types was fixed to a previously measured value D_{in} = 1.58 μm²/ms [61]. Different concentrations of free water, ranging from 0-100%, were added to mimic the influences of edema or cysts, which usually confound non-contrast enhanced MRI method in brain cancer imaging. Rician noise was added to dMRI signals at a typical signal-to-noise ratio (SNR) of 20 in brain dMRI at 3 Tesla. Simulations were repeated 1000 times and the means and standard deviations of all results represent the accuracy and precision of the SSIFT measurements.

Cell lines in vitro. Six different cancer cell lines were used to investigate the influences of various cancer cell types and sizes:

1. C6 (rodent glioma), 9L (rodent gliosarcoma) and GL261 (murine glioma) to mimic primary brain cancer; and

2. A549 (human lung carcinoma), B16 (mouse melanoma), and MDA-MB-231 (human breast adenocarcinoma) to mimic the three most common sources of metastatic brain cancers, i.e., lung, skin (melanoma), and breast cancers [104].

Moreover, human lymphocyte and Jurkat cell data from a previous study [30] were used as a reference for small cells, and a doped water sample with 0.1 mM $MnCl_2$ was used to mimic CSF. All tumor cell lines were purchased from ATCC and cultured in RPMI Medium 1640 supplemented with 10% FBS, 50 Units/ml penicillin, 50 µg/mL streptomycin (and 5 µg/mL recombinant insulin for breast cell lines) (Invitrogen, CA) in a humidified incubator maintained with 5% CO2 at 37°C. Cells were cultured in 150 mm dishes to full confluence, then harvested by trypsinization, washed and resuspended with PBS. Lymphocytes were extracted from human peripheral blood by using the Ficoll method [105], briefly, blood was diluted with an equal volume of PBS, and carefully added to the top of an equal volume of Ficoll-Paque in a centrifuge tube. After centrifugation at 800g for 20 minutes, the cells in the interface layers were collected, the residual red cells were removed by hypotonic lysis and washing, and the final lymphocytes were pelleted and re-suspended with PBS.

For MR experiments, cells were washed with PBS after fixation with 4% paraformaldehyde for over one hour, about 3 x 10^7 cultured cells (or 1x10^9 lymphocytes) were centrifuged at 2000g x 2 minutes in a 0.65 mL of Eppendorf tube to obtain a tight cell pellet. All the liquid on the top was carefully removed, and the tube with cell pellet was used for MRI measurements.

MRI experiments of cells. MRI measurements of cells in vitro were performed on a Varian/Agilent 4.7T MRI scanner (Agilent Technologies, Santa Clara, CA). A 2-mm-thick slice through the center of each cell pellet was imaged with a field of view (FOV) 16×16 mm^2 and a matrix size 32×32, yielding a spatial resolution of 500 µm.

Light microscopy. A small aliquot of cells from each sample pool used in MRI experiments was spotted on a glass slide and covered by coverslip. Digital images of cells were recorded at both 20x and 40x, amplification. A stage micrometer was used with the same microscope and settings

for size calibration. Average cell sizes from over 200 cells were calculated with the help of NIH ImageJ software [106]. Table 1 summarizes the calculated cell sizes.

Animals in vivo. Animal studies of rats and mice were approved by the local IACUCs and performed at Vanderbilt University Medical Center and Washington University in St. Louis, respectively. The use of different species, tumor types, and methods of inducing radionecrosis at two different institutions provided an opportunity to interrogate the ability of SSIFT to differentiate brain tumors from radionecrosis under various conditions.

Rat study at Vanderbilt University Medical Center:

1. Brain tumor in rats. To generate 9L gliosarcoma xenografts, male Fischer rats (Envigo, Indianapolis, IN, USA) were immobilized in a stereotactic head holder under anesthesia (via a 5:95% isoflurane/oxygen mixture) and were inoculated with 1×10^5 9L cells in 5 µL by using a 10-µl gastight syringe (Hamilton, Reno, NV, USA). The site of the inoculation was 1 mm anterior and 3 mm lateral to the bregma on the right side of the head, at a depth of 4 mm relative to the dural surface. Tumor growth and size were estimated by MRI after 2 weeks. 8 subjects grew large tumors and were imaged using SSIFT and DTI protocols.

2. Radionecrosis in rats. 6 rats were treated replicating clinical high-dose stereotactic radiosurgery (SRS) via a clinical Novalis TX™ unit by Varian Medical Systems (Palo Alto, California). The animals were stabilized on the couch with a bite bar and head bar. Cone-beam CT (CBCT) was used to localize the target and register the dose plan. 140 Gy was delivered to isocenter via 10 noncoplanar arcs using a 4 mm diameter cone. All 6 rats developed sufficiently large radionecrotic lesions by 8 weeks.

Mouse study at Washington University:

1. Brain tumor in mice. Tumor cells were implanted in mice, as described previously [107]. Briefly, mice were anesthetized with isoflurane and secured in a stereotactic head holder. Murine DBT glioblastoma cells were implanted (~10,000 cells suspended in 10 µL per mouse) over three minutes at a site 2-mm posterior and 3-mm to the left of bregma, 2-mm below the cortical surface.

2. Radionecrosis in mice. Six- to eight-week-old Balb/c mice were irradiated focally using a

clinical Leksell Gamma Knife (GK) Perfexion™ (Elekta AB; Stockholm, Sweden) with a single 50 Gy (50% isodose) radiation dose in the left hemisphere. Mice were scanned by MR 13 weeks post irradiation, at which time radionecrosis occupied a significant fraction of the irradiated hemisphere [108].

MRI experiments of animals. Animal MRI scans of rats and mice were acquired separately at Vanderbilt University Medical Center and Washington University, but both used the same protocol on 4.7T Varian/Agilent horizontal small animal scanners. A single-shot echo-planar imaging (EPI) diffusion sequence was used in both studies with fat suppression and saturation bands to minimize confounding signals from outside the brain. Rats were scanned using a Litz38 volume coil for both transmission and reception. Axial slice thickness = 1 mm, FOV = 16 × 16 mm and matrix size 64 × 64, resulting in a 250 μm in-plane resolution. Mice were scanned using an actively decoupled coil pair: a 9-cm inner diameter volume coil (transmit) and a 1.5-cm outer diameter surface coil (receive). Axial slices with 1-mm thickness were acquired with FOV = 12 × 9 mm and matrix size 48 × 32, yielding an in-plane resolution of 250 × 285 μm. TR/TE = 4000/98 ms.

Histology. Following imaging, rat brain tissues containing 9L gliosarcoma or radionecrosis were fixed by cardiac perfusion using 10% formalin, immersed in formalin for two days, and immersed in 70% ethanol. 8 μm-thick slices were stained with hematoxylin and eosin (H&) and assessed digitally using QuPath version 0.3.1 [109].

Patients. Human studies were approved by the local IRB at Vanderbilt University Medical Center. Two patients with brain metastases, one with non-small cell lung cancer (NSCLC) and one with melanoma, were scanned pre-treatment with the SSIFT protocol. One patient with extensive radiation necrosis was scanned following treatment of renal cell carcinoma metastatic to the brain. Scans were performed using a Philips 3T dStream Ingenia scanner with a 32-channel head coil. Acquisition sequence parameters were: TR/TE = 15 s / 118 ms; FOV = 224 × 224 mm; half scan factor 0.64; slice thickness = 5 mm; an isotropic resolution of 2 mm; and fat suppression with spectral adiabatic inversion recovery. Total scan time of SSIFT was ≈ 16.5 minutes. In addition, DTI measurements using PGSE acquisitions with Δ = 54 and 34 ms were performed to further investigate ADC dependence on diffusion times. For comparison, anatomical T1w gradient echo

images with TR/TE = 8 ms / 3.76 ms were acquired with image size 256 x 256 and 1 mm³ isotropic voxel size, and T2w FLAIR images with TR/TE = 11 s / 125 ms, image size 512 x 512, and 0.5 x 0.5 x 3 mm³ voxel size. The patient with NSCLC received clinical standard contrast-enhancement while the melanoma and radionecrosis patients were unable to receive gadolinium due to concerns of kidney dysfunction.

Data analysis. All diffusion images were processed using MRtrix3 [94] for noise [89] and Gibbs ringing [95] correction, FSL [97,98,110] for eddy current correction [92] (human data only), ANTS for N4 field bias correction [111] (human data only), and purpose-written Matlab (The MathWorks Inc., Natick, MA, USA) scripts. The average of signals over all diffusion directions of the same b value was used to remove the effects of diffusion anisotropy. Voxelwise normalization by b=0 intensity was avoided, as compartments with free water or small restrictions would not be filtered out of the b=0 signal and could reduce cell-size-weighted contrast due to a difference in T2-weighted contrast [85]. Instead, the directionally averaged diffusion signals were normalized using median b=0 signals in white matter for each scan as determined with an FA mask (as done for intersubject comparison in [86]); however, rodent data were normalized by the median contralateral gray matter signal because white matter was difficult to isolate. The incremental area under curve (iAUC, see Fig.1) was calculated using the normalized signal and values are reported as the iAUC as a percentage of normalization signal. DTI metrics (i.e., FA and ADC) were obtained using the PGSE acquisitions for comparison. ROIs were manually drawn on pre- and post-contrast T2w EPI images for brain tumors/radionecrosis, peritumor edema, and contralateral regions. The contrast-to-noise ratio (CNR) of an MRI metric P between two types of tissues I and II was calculated as CNR = $\text{abs}(P_I - P_{II})/(\sigma_{P_I}^2 + \sigma_{P_{II}}^2)$.

4.3 Results

Simulations: SSIFT is more specific to cell size than ADC. The simulated influences of intracellular volume fraction v_{in} of cancerous and non-cancerous tissues, consisting of large (16 μm) and small (8 μm) cells, respectively, are shown in Figure 18. Note that ΔADC = ADC(t_{diff}=10ms) − ADC(t_{diff}=70ms), which has shown t_{diff} dependent sensitivity to subtle microstructural changes in the brain [112]. Figure 18d shows the CNR between a cancerous tissue with v_{in} = 70% and brain tissues with varying v_{in}. Depending on v_{in}, conventional ADC of brain tissues with t_{diff} =

70 ms could be higher or lower than that of cancerous tissue, suggesting that conventional ADC is not a reliable biomarker to distinguish cancer from brain tissues. Both ΔADC and iAUC are able to distinguish tumors from brain tissues, but iAUC has a higher precision (smaller variations) particularly at low cell densities, suggesting iAUC is a more reliable metric to distinguish cancerous tissues consisting of large cells from other brain tissues consisting of small cells.
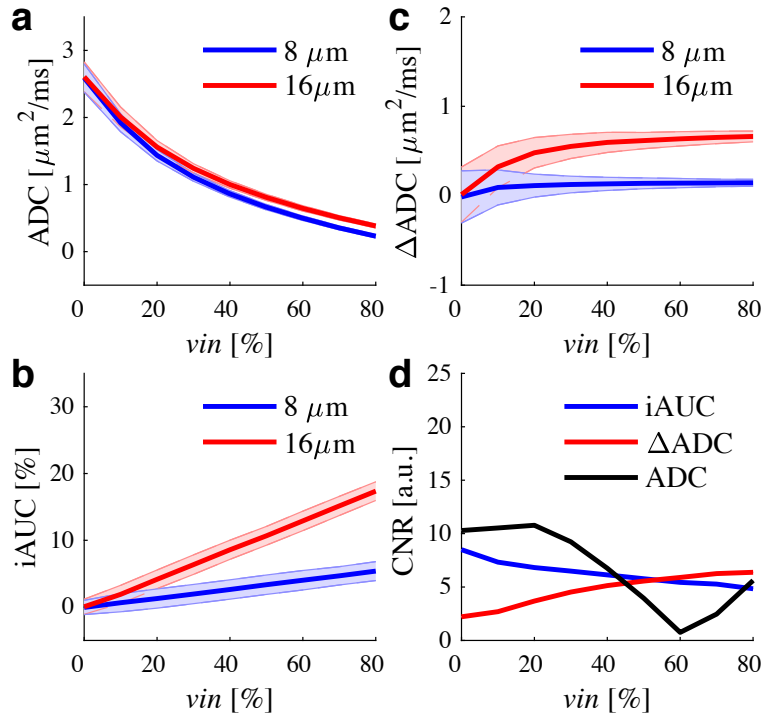
Figure 18. Simulated SSIFT vs. ADC. Simulated dependence of (a) conventional ADC with t_{diff} = 70 ms, (b) iAUC from SSIFT on varying intracellular signal fraction v_{in}, (c) ΔADC between t_{diff} = 10 and 70 ms, and (c) Subfigure (d) shows the contrast between a cancerous tissue with v_{in} = 70% and brain tissues with varying v_{in}.

In vitro: SSIFT is sensitive to cancer cells. Cell experimental results are summarized in Figure 19, showing a correlation between iAUC and mean cell size obtained using light microscopy with r = 0.92 and p < 0.01 obtained using the Spearman rank correlation. There are significant discrepancies in iAUC between all cancer cells (12.6 – 15.6 μm) and the lymphocytes and jurkat cells with a smaller cell size (10.3 – 11.9 μm). This is consistent with the simulation results shown above that SSIFT iAUC selectively enhances sensitivity to large cancer cells with simultaneous suppression of signals from water and small cells.
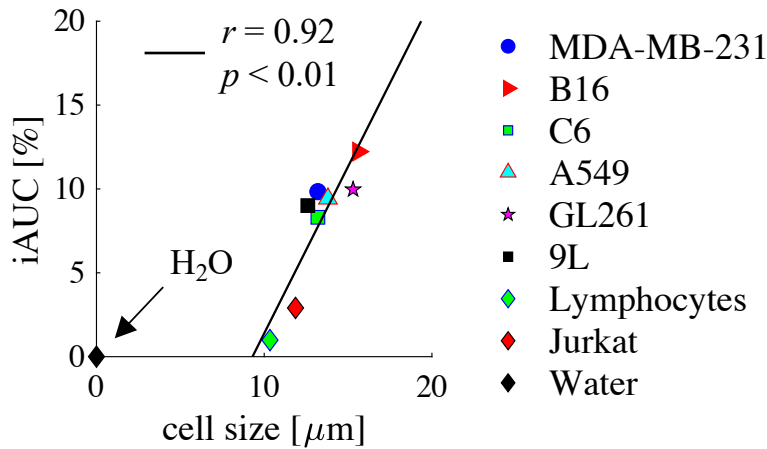
Figure 19. SSIFT dependence on cell size in vitro. The correlation between iAUC and mean cell size obtained using light microscopy. Doped water iAUC is also provided as a reference. Correlation coefficient and p-value were determined by Spearman rank correlation.

Cell line	Organism	Tissue	Diseases	Cell size [µm]
C6	Rat	Brain	Glioma	13.2 ± 1.9
9L	Rat	Brain	Gliosarcoma	12.6 ± 2.2
GL261	Mouse	Brain	Glioma	15.3 ± 4.7
A549	Human	Lung	Carcinoma	13.8 ± 2.3
B16	Mouse	Skin	Melanoma	15.6 ± 3.5
MDA-MB-231	Human	Breast	Adenocarcinoma	13.2 ± 2.9
Lymphocyte	Human	Blood	N/A	10.3 ± 2.0
Jurkat	Human	Blood	Leukemia	11.9 ± 2.0

Table 1. A summary of cell lines and their corresponding mean cell size measured using light microscopy.

In vivo: SSIFT can differentiate radiation necrosis from tumor. Figure 20 shows the multi-parametric images of both rats and mice with brain tumors and radionecrosis. ADC alone provides ambiguous results due to the variations of the CSF volume fraction. This provides challenges to distinguishing viable tumors (highlighted on T2w with contrast agents) from peri-tumoral edema. SSIFT iAUC, however, provides a clear contrast that emphasizes the tumor. SSIFT iAUC shows

diminished contrast in radionecrosis and contralateral regions, which is expected because there are no significant changes in cell size in radionecrosis.
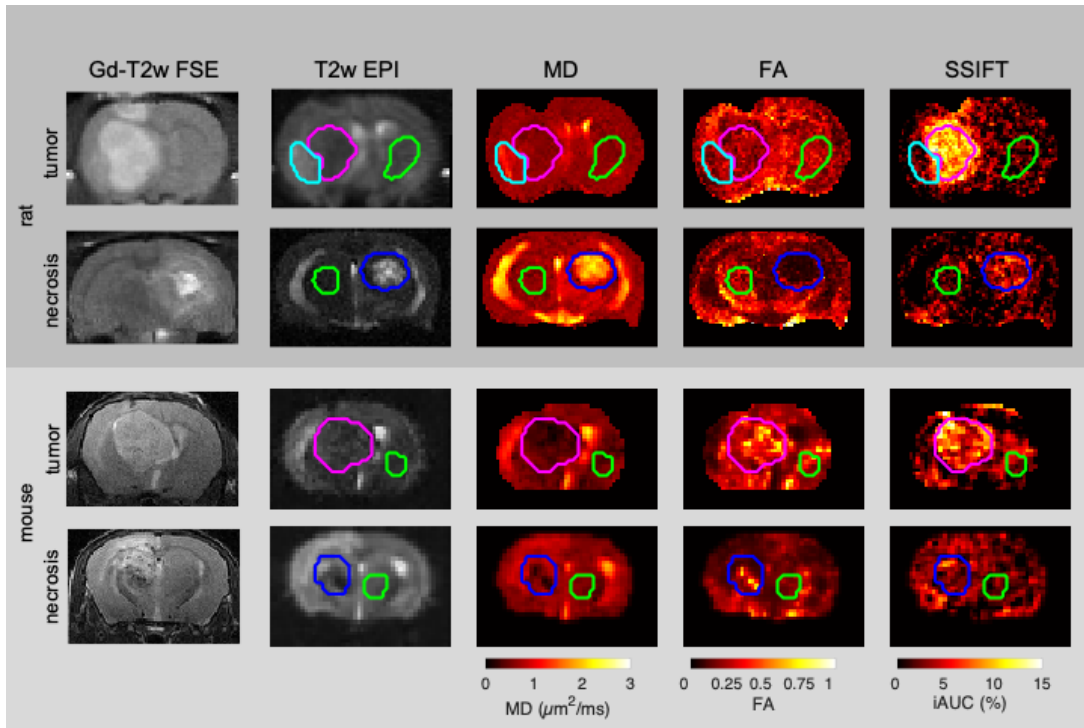
Figure 20 DTI and SSIFT images of rats and mice with brain tumors and radionecrosis. ROIs of tumor (pink), radionecrosis (blue), and contralateral regions (green) were manually drawn on T2w EPI images. Peritumor edema (cyan) was delineated in rats by hyperintense T2w EPI signal that is unaffected by Gd contrast and absent in the contralateral anatomy. ROIs were overlayed ADC, FA, and SSIFT maps registered to the T2w EPI. SSIFT shows more selective contrast in the tumor ROI than ADC or FA.

Figure 21 summarizes all iAUC and ADC values of all ROIs. Using a two-sided Wilcoxon rank sum test, in both mice (N=4 tumor, N=4 radionecrosis) and rats (N=8 tumor, N=6 radionecrosis) ROI-averaged SSIFT iAUC values are significantly different in tumor vs radionecrosis ($p < 0.05$ mice, $p < 0.001$ rats). A signed test is used in same-subject comparisons, with significant differences in tumor vs contralateral tissue ($p < 0.05$ mice, $p < 0.01$ rats) and vs edema in rats ($p < 0.01$). These tests of whether the SSIFT iAUC had different median values from each other tissue were significant within $p < 0.05$. There was no overlap in the distributions with tumor, giving 100% classification in both rats and mice. Additionally, we can observe that ADC shows contrast

in tumor vs radionecrosis. Contrast between peritumor edema and radionecrosis was small ($ADC_{rat,edema} = 0.92 \pm 0.10 \ \mu m^2/ms$, $ADC_{rat,RN} = 0.99 \pm 0.14 \ \mu m^2/ms$). FA decreases in radionecrosis relative to all other tissues and better separates necrosis from peritumoral edema ($FA_{rat,RN} = 0.16 \pm 0.03$, $FA_{rat,edema} = 0.24 \pm 0.04$) than ADC, but is insensitive to tumor.
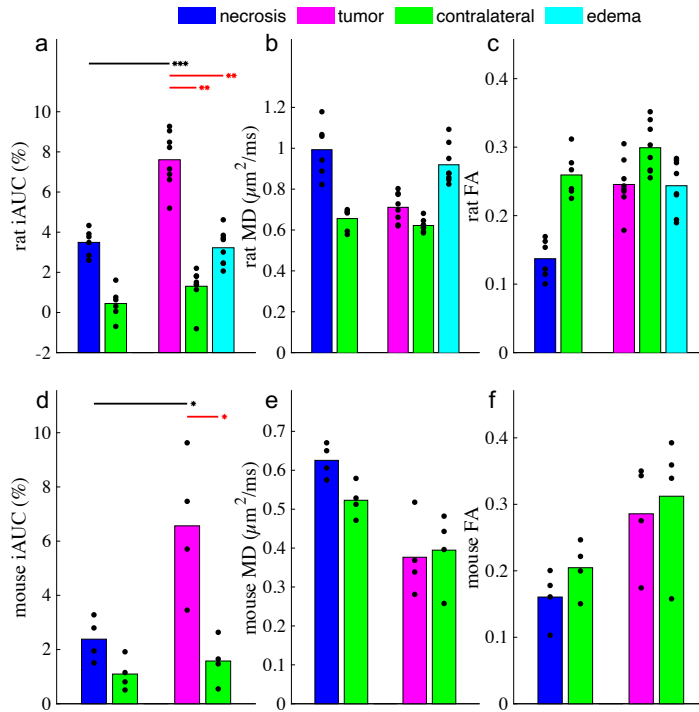
Figure 21 DTI and SSIFT tissue bar chart. Summarized results of SSIFT. iAUC (a,d), ADC (b,e) and FA (c,f) in different tissue types in rat (a-c) and mouse (d-f) subjects. Bar colors match the ROIs in Figure 20. Scatter points represent the ROI-averaged metric in individual subjects. *** p < 0.001, ** p < 0.01, * p < 0.05 by signed (red) and unsigned (black) Wilcoxon rank sum tests.

Histology: Number of large cells in tumor drives SSIFT contrast. Representative slices of H&E staining from rat tumor and radionecrosis are shown in Figure 22. The cross sections from rat brains following radiation therapy demonstrate heterogeneous features including vascular telangiectasias, intravascular thrombosis, fibrinoid necrosis, cavitation, tissue necrosis, inflammatory cell infiltrates including neutrophils and lymphocytes, macrophages and microglia, and gliosis in addition to remnant neural tissue with neurons and normal glial cells. The cells demonstrate a broad range in size from approximately 27-562 μm^2, with the largest cells representing neurons, foamy macrophages, or reactive astrocytes and the smallest cells

representing inflammatory cells. The cell density is relatively low, averaging approximately 2600 cells/mm^2. Sections from rats with gliosarcoma demonstrate a relatively well-circumscribed neoplasm comprising enlarged neoplastic cells with ovoid-to-pleomorphic, hyperchromatic nuclei and eosinophilic cytoplasm. Cell density within the tumor measured around 6000 cells/mm^2. The nonneoplastic and nonreactive brain tissue in similar regions of the brain (e.g., hippocampus and thalamus) averages approximately 1900 cells/mm^2 with cell size ranging from approximately 22-502 μm^2.
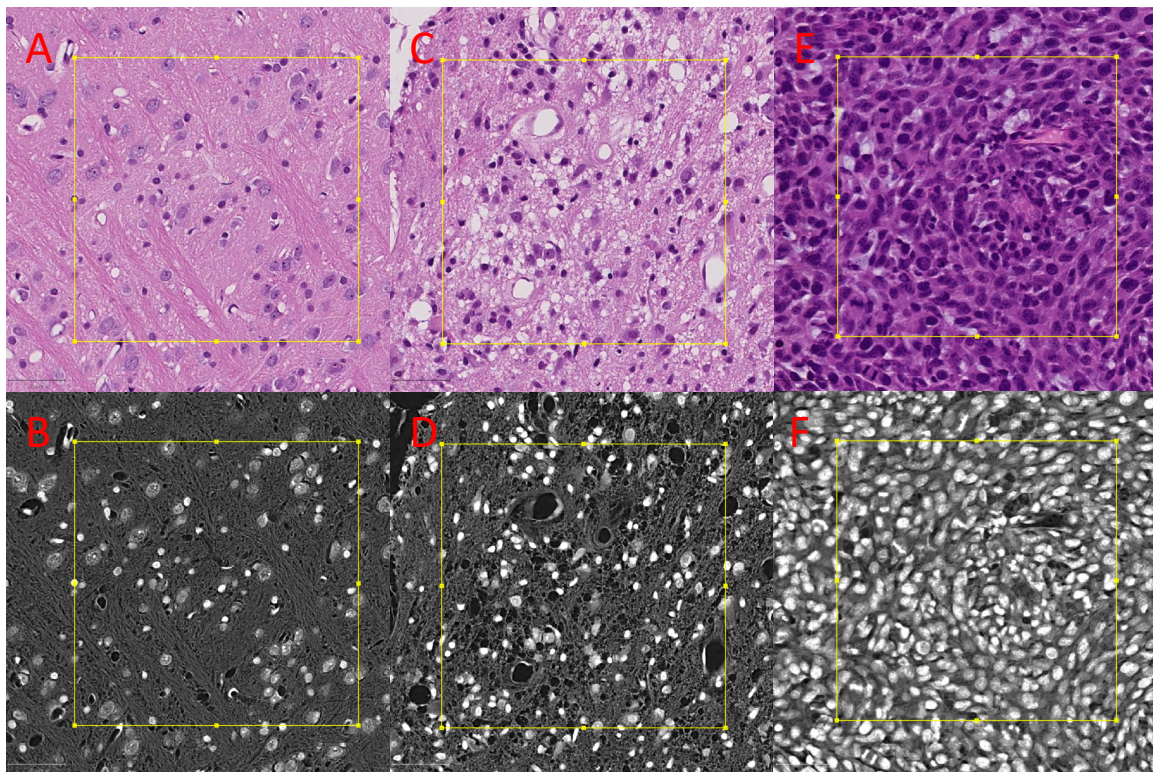
Figure 22 Hematoxylin and Eosin slides. The top row depicts brightfield microscopy for H&E stains in normal-appearing tissue (A-B), radiation injury (C-D), and tumor (E-F). The dark purple spots indicate cell nuclei. The yellow box indicates the size of a voxel (500x500μm) and the scale bars are 50μm on each slide. The bottom row shows the estimated hematoxylin signal deconvolved from the colored image, and shows good contrast for counting nuclei.

Representative patients with brain metastases and radionecrosis. Figure 23 shows representative anatomical MRI, FA, and ADC (ADC) maps from conventional DTI, and SSIFT iAUC maps of two brain cancer patients. The non-small cell lung cancer patient received Gd contrast while the

melanoma patient was unable to receive Gd due to kidney dysfunction. T2w FLAIR shows regions of viable tumors and peri-tumor edema, which are challenging to distinguish on FA or ADC maps. By contrast, SSIFT iAUC maps show distinct contrast of brain metastases alone, providing a similar contrast as the post-contrast T1w image. The radionecrosis lesion shows slight elevation in ROI-averaged iAUC (1.9 ± 2.0 %), while the NSCLC tumor shows much higher values (11.9 ± 3.4 %). Contralateral values in both are 0.5 ± 2.5 % and -0.3 ± 1.0 %, respectively.
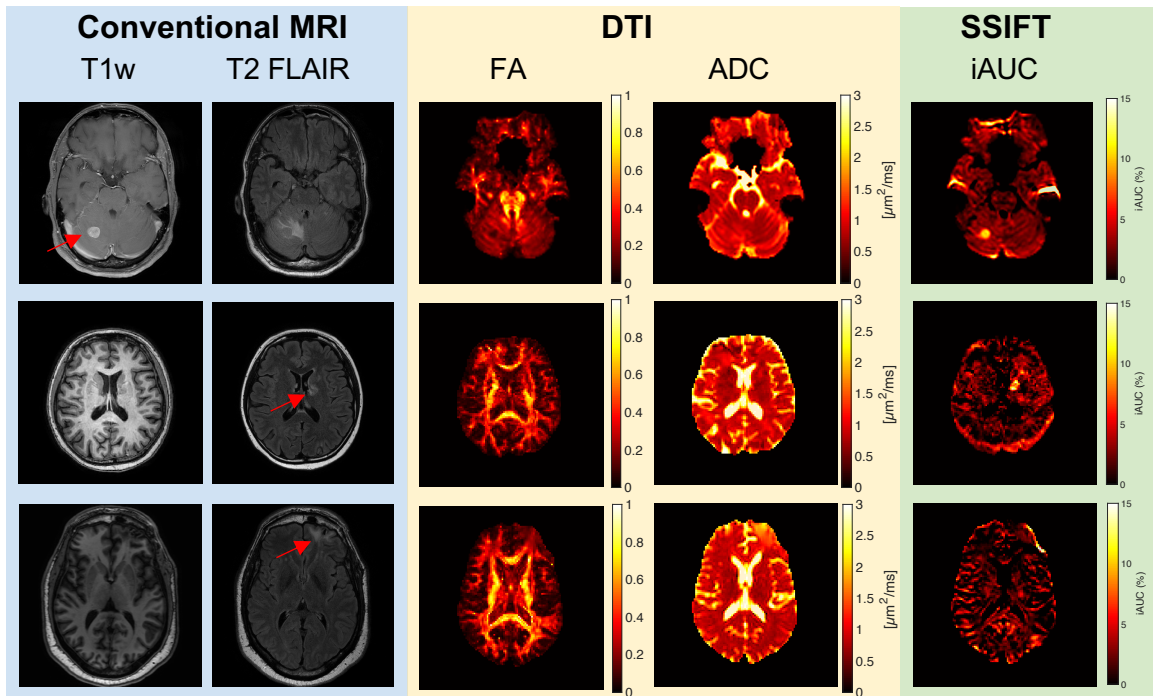
Figure 23. SSIFT results in patients. Representative images of patients with non-small cell lung cancer metastatic to the right cerebellum (top row) and melanoma adjacent to the left ventricle (middle row). The T1w image on the top is Gd-enhanced while the T1w images in the middle and bottom rows were collected without Gd contrast due to kidney dysfunction. Red arrows indicate lesions identified on the Gd-T1w image when available or T2 FLAIR otherwise. The cerebellar lesion demonstrates considerable associated peritumor edema (evident in T2 FLAIR) that is not apparent on the SSIFT map, while the tumor itself shows high signal contrast on SSIFT imaging relative to the surrounding tissue. The melanoma lesion apparent on T2 FLAIR has a high iAUC relative to the contralateral tissue. iAUC in the right frontal brain in radionecrosis (bottom row) is slightly elevated, but is substantially lower than in the tumors. Susceptibility correction was

available for the melanoma patient. The bright band at the bottom of the SSIFT image is likely the eddy artifact described in Chapter 3.

4.4 Discussion

Diffusion MRI has been implemented to differentiate recurrent tumors from radionecrosis. However, a meta-analysis shows that dMRI has only moderate diagnostic performance [113]. One explanation is that dMRI is influenced by multiple tissue microstructural features simultaneously including tissue orientation and composition. All types of tissues in an image voxel contribute to mixed dMRI signals. Therefore, other concurrent brain processes, such as edema and radionecrosis, may sometimes appear indistinguishable from brain metastases [114]. The SSIFT method focuses on a key intrinsic difference between brain tumors and other brain etiologies, i.e., the fraction of cells distinguished by cell size, and uses this distinct pathological feature of brain tumor and radionecrosis to distinguish these two types of lesions. This was validated in simulations, cells in vitro, and animals in vivo in the current work. The application of this technique in patients with neoplasms metastatic to the brain further confirms this and demonstrates the feasibility of the SSIFT method in human imaging. By targeting a physiological feature different from other dMRI methods, SSIFT may improve the diagnostic accuracy in differentiating radionecrosis from tumor. SSIFT additionally shows higher contrast between tumor and all other tissues in each study than is observed in conventional imaging, suggesting it may be useful for characterizing highly heterogeneous lesions.

The SSIFT method is based on the premise that cancer cells usually have larger cell sizes than those of most brain cells, and the contrast is dependent on both the differences in cell size, i.e., larger cancer cells resulting in larger SSIFT iAUC values (Figure 19), and the signal fraction of cells (i.e., cell density) within the SSIFT filter (Figure 18). The in vivo animal validations in this study comprised 9L gliosarcoma and DBT glioblastoma cell lines, which showed high contrast in SSIFT relative to normal brain tissue and other malignancies. Cell counts from H&E histology indicate the tumors in rats have a high density of 9L cells that are in the size range detectable by SSIFT, as measured in Figure 19. The cell study (Figure 19) consisted of human cell lines from the most common sites of origin of brain metastases: lung, breast, and melanoma. However, brain cancers can be very heterogenous and SSIFT may have different performance in different types of brain neoplasms with different cancer cell sizes and cellularities. More investigation is necessary

to evaluate SSIFT in specific types of human brain cancers. Further investigation into SSIFT in patients with radionecrosis will also be needed, as the animal subjects in this study showed slightly elevated SSIFT iAUC values relative to normal tissue. This is likely due to the increased cellularity in radionecrosis lesions observed in rats, which could diminish contrast relative to some cancer cell lines if present in humans. Nevertheless, SSIFT is a promising imaging method particularly for NSCLC which has large mean cancer cell sizes of 17.3 – 20.6 μm [115]. Because the most common source of brain metastases is lung cancer (67.2%) [104] and 80 – 85% of all cases of lung cancer are NSCLC [116] SSIFT has the potential to play a role in imaging NSCLC in the clinical setting.

Further development of the method may improve human implementation. IVIM (intravoxel incoherent motion) effects were not explicitly considered in the current work but it may adversely influence SSIFT contrast. Because OGSE sequences are flow-compensated and less influenced by blood perfusion [117], IVIM shows a t_{diff} dependence, i.e., pseudo-diffusion increases with larger t_{diff} [118]. If the pseudo diffusion (perfusion) component is sufficiently large that it may conceal the cell size restriction induced t_{diff} dependence, which is the biophysical basis of SSIFT. This effect has been observed in the liver with a high blood volume [119]. Our results in animals and patients in vivo did not show this effect, presumably because of the relatively much lower cerebral blood volume. However, if the IVIM effect becomes a concern, additional acquisitions with lower b values (e.g., 250 s/mm^2) can be used to remove the IVIM effects [119], although this could increase the scan time. Additionally, the propagation of imaging artifacts to the iAUC has not been fully characterized. For instance, PGSE and OGSE diffusion-encoding gradients may induce different eddy currents which, if not fully corrected, could appear as diffusion time dependence and lead to aberrant values in SSIFT. It is also unknown how much variance in iAUC is due to noise or physiology. The CNR does not change significantly as the number of direction averages is decreased (Chapter 3, Figure 14), indicating the variance may not be due to random noise. Whether due to noise or diffusion time dependence in normal tissue, the contralateral variations are small compared to the iAUC values in tumor (Figure 23) such that sufficient contrast can still be generated.

The total scan time of the SSIFT method in humans was 16.5 mins because of the long TR (15 sec), a limitation imposed by diffusion gradient duty cycle in the OGSE sequence used in our Philips Ingenia 3T scanner. The number of gradient directions can be decreased while maintaining

similar imaging contrast. Figure 14 shows that fewer gradient directions, e.g., 6 directions, can still provide a significant contrast to differentiate tumors from peri-tumor edema, with which the total scan time of SSIFT could be further reduced to ~3 mins. A reduction in the number of slices can also either reduce scan time further or be used as an alternative to lower directional sampling if needed. Although further optimization of SSIFT is needed, the scan time is not a limiting factor for the translation of SSIFT to clinics. Additionally, since PGSE images with multiple diffusion encoding directions are acquired, information from DTI can also be obtained. Combining iAUC with information from ADC or FA could add to SSIFT's diagnostic ability to classify lesions at no cost to scan time.

Although contrast-enhanced T1w MRI is a standard method for imaging brain metastases, its usage can be limited in the setting of kidney dysfunction or severe contrast allergy. Moreover, some brain tumors, such as low-grade glioma, do not show contrast enhancement, which results in challenges for treatment planning in radiation oncology. Other non-contrast-enhanced MRI methods such as T2 FLAIR and DTI suffer from complex tissue compositions and cannot reliably differentiate tumors from peri-tumor edema. By contrast, Figure 23 shows SSIFT provides reasonably high conspicuity and delineation of brain metastases, suggesting SSIFT may be an alternative method for imaging brain metastases when contrast-enhanced MRI is not an option. However, SSIFT is a dMRI based method that suffers from drawbacks such as distortions and relatively low resolutions (e.g, 2 mm). Corrections for eddy-current and susceptibility induced distortions can alleviate such confounding effects. SSIFT will also benefit from recent progress in super-high resolution of DTI [120], smaller than the typical 2 mm resolution used in standard clinical practice.

CHAPTER 5

Multiparametric MRI for differentiating brain tumors from radiation necrosis in preclinical models

Chapter 1 described how several methods have been applied to the problem of differentiating radiation necrosis yet have drawbacks that may hinder them from being a solution to the challenge. Chapter 4 showed via preclinical data that SSIFT has potential to meet this need, but it is unknown whether SSIFT alone is sufficient to discriminate these lesions in humans. Additionally, with many methods probing different elements of the microstructure, it is possible that a combination of techniques may provide better diagnostic accuracy than one method alone. In this chapter, we therefore explore two themes to help inform future studies in humans. First, how SSIFT contrast compares to other existing methods in a direct comparison on the same subjects, and second, how multiple parameters could be mapped to a binary classifier to differentiate radiation necrosis from tumor. The data available to this study was quite limited, and we therefore emphasize that the results shown here are not intended to demonstrate which methods could best address this problem – that conclusion is best left to human studies, as animal models on preclinical scanners do not fully replicate values in humans on clinical scanners. Instead, this chapter contextualizes SSIFT in the body of quantitative MRI that has been applied to this clinical challenge and provides a methodological framework to motivate human studies.

5.1 Background

Stereotactic radiosurgery (SRS) is a non-invasive therapy using high radiation dosage to increase the local control of a small number of brain tumors. Major advantages of SRS include increased local control, a patient-friendly schedule of a single fraction treatment, and minimized late neurocognitive sequelae associated with conventional whole-brain radiotherapy [5]. However, 10-20% of SRS-treated patients will develop new radiographic enlargement at the site of prior SRS that is either radiation-induced necrosis (RN) or recurrent tumors. It remains a challenge in clinical

radiation oncology to reliably differentiate recurrent brain tumors from RN. Although computer-assisted stereotactic biopsy has been suggested as the gold standard to determine lesion types [10], the nature of its invasive procedure leads to unwanted risks such as hemorrhage associated with increased inpatient mortality [11]. The standard of care imaging method such as the conventional MRI with gadolinium (Gd)-based contrast agents (Gd-MRI) is incapable of distinguishing recurrent brain tumors from RN due to the breakdown of BBB in both types of lesions [121,122]. Therefore, there is a need to develop a reliable non-invasive imaging method to tackle this clinical challenge.

Numerous imaging methods have been developed and implemented to differentiate recurrent tumors from RN [13], including but not limited to the amino acid and FDG-PET/CT [14], proton MR spectroscopy (^{1}H MRS) [15–17], dynamic susceptibility contrast (DSC) MRI particularly with relative cerebral blood volume (rCBV) [22], chemical exchange saturation transfer (CEST) with amide proton transfer (APT) and nuclear Overhauser enhancement (NOE) [18,19], quantitative magnetization transfer (qMT) [20], and diffusion tensor imaging (DTI) with mean diffusivity (MD) [123,124]. Additionally, SSIFT is included based on its demonstrated ability to differentiate necrosis from tumor in our animal study (Chapter 4). All of these methods provide information on specific pathophysiological features of brain lesions and hence show promise to differentiate different brain lesions. Despite these efforts, however, there is still a lack of any single imaging method in practice that can reliably differentiate recurrent tumors from RN in practice. One possible reason is due to the remarkable heterogeneity of individual imaging metrics across different lesions in different patients, making no single MRI method likely to solve this clinical challenge alone [23].

To overcome such limitations, multi-modality imaging (e.g., combining PET and MRI [125,126]) has been proposed, but this in turn significantly increases medical cost and imaging time. An alternative approach is multi-parametric MRI, which acquires two or more MRI methods in a single session to enhance diagnostic accuracy. For example, previous studies have reported combining diffusion and perfusion MRI [127], and diffusion MRI with MRS [128] to distinguish recurrent tumors from RN. Because multiparametric MRI provides complementary information, a more comprehensive evaluation may provide a more accurate classification of lesion types. Despite these improvements, however, two fundamental questions remain unanswered:

1. How should candidate MRI methods be chosen? Because there are many promising MRI

methods, it is impossible to combine all of them in a reasonable amount of scan time. It is therefore of interest to find an effective combination with the least number of MRI methods.

2. How should multiple imaging metrics from different methods for better classification be incorporated? Previous studies usually combine two imaging metrics for simplicity, but it is of interest to combine three or more metrics to maximize classification performance in higher dimensional parametric space.

The present work aims to show some preliminary results towards addressing the above questions. To choose appropriate MRI methods, we use the following criteria that any candidate method should:

1. Have shown promise to distinguish recurrent tumors from RN as an individual method;

2. Be able to provide reasonably high spatial resolution (1-3mm in-plane) to detect small lesions in human imaging;

3. Provide quantitative metrics with minimized user intervention or an automated pipeline;

4. Probe pathophysiological information on different scales to comprehensively characterize lesions at different levels.

Based on these criteria, five types of MRI methods were identified as candidate MRI methods in this study, including T_2 (relaxation), CEST (chemical exchange saturation transfer) based APT (amid proton transfer, probing mobile proteins) and NOE (nuclear Overhauser effect, probing mobile macromolecules), qMT (quantitative magnetization transfer, probing macromolecules), diffusion based MD (mean diffusivity, probing cell density) and SSIFT (size-selective imaging using filters via diffusion times, probing cell size), and perfusion based DSC (dynamic susceptibility contrast, probing blood volume and flow). In addition to comparing the discrimination performance of individual MRI parameters, a general statistical approach was used to choose an appropriate combination of multiple MRI parameters with the maximized discrimination performance. To demonstrate how this analysis can be performed, multiparametric MRI was performed in a rodent brain tumor model and a radiation necrosis model at 4.7T.

5.2 Methods

Animal Preparation. All animal procedures were approved by the local IACUC. Male Fisher 344 rats (Envigo, Indianapolis, IN, USA) were used throughout the study. All animals were under

anesthesia by a 2/98% isoflurane/oxygen mixture stabilized with a bite bar and head bar in all radiotherapy and imaging procedures.

Brain tumor model. A 9L gliosarcoma xenograft model was implemented to generate brain tumors (n=6). Animals were anesthetized by a 5/95% isoflurane/oxygen mixture, immobilized using a stereotactic head holder, and inoculated with 10^5 9L cells in 5 µL using a 10-µL gastight syringe (Hamilton, Reno, NV, USA) 1 mm anterior and 3 mm lateral to the bregma on the right side of the head at a 4 mm depth from the dural surface. The subjects grew large tumors around 25 days after tumor induction.

Radiation necrosis model. Animals (n=6) were treated with high-dose radiotherapy to induce RN lesions. This treatment model used a clinical Novalix TX™ (Varian Medical Systems, Palo Alto, California, USA) linear accelerator with a multi-arc, single fraction plan of 140Gy to isocenter. This is the treatment described in Chapter 5. All six animals developed notable lesions by 60 days following radiation. 5 animals were scanned with all MRI protocols.

MRI. All imaging methods were completed in one session per animal using a 4.7T Varian/Agilent small animal scanner (Agilent Technologies, Santa Clara, CA) and a Litz38 volume coil (Doty Scientific, Columbia, SC, USA) for both transmit and receiver. Respiratory rate and internal temperature were monitored throughout the scans.

Anatomical. T_2-weighted fast spin echo (FSE) images were acquired before and after contrast injections. TR = 2,000 ms, echo train length (ETL) = 8, effective TE = 36 ms. FOV = 32 x 32 mm, image size 128 x 128, slice thickness 0.5 mm.

T_2 relaxation. Spin-echo echo planar imaging (SE-EPI) was performed with multiple echo times TE = {34, 40, 50, 60 ms}. TR = 3000 ms, spatial saturation bands were used for a reduced FOV = 16 x 16 mm covering animal brains only, image size 64 x 64, and a slice thickness 1 mm. A mono-exponential was fit to the signal to determine T_2.

CEST. A continuous-wave prepared SE-EPI was used for CEST imaging. The saturation power was 0.8 µT and the frequency offsets covered ±50 ppm, with a 0.2 ppm resolution from -5 to 5 ppm. TR/TE = 6000/28 ms, FOV = 32 x 32 mm, image size 64 x 64, slice thickness 2 mm. The Z-spectra were corrected for B_0 heterogeneity and then fit as three Lorentzian curves with set peak locations at +3.5, 0, and -3.55 ppm as described by Zaiss et al. [129] using a publicly available peak fitting package [130]. Peak height was used to quantify APT and NOE.

qMT. Selective inversion recovery qMT with SE-EPI [131,132] was performed using 7 t_i/t_d (inversion time / delay time) combinations optimized for cancer imaging [133]: {1331/10, 450/3454, 319/3589, 252/1080, 78/4531, 50/4729, 4/4735 ms}. TE = 28 ms, FOV = 32 x 32 mm, image size 64 x 64, slice thickness 2 mm. The signals with varying t_i/t_d combinations were fit to the signal model described in [134] with fixed S_m=0.83 and R_m=1. Five parameters including PSR (pool size ratio of immobilized protons over free water protons) and R_{1f} (R1 relaxation of free water) were fitted in the present study.

Diffusion. Diffusion sequence was performed with both pulsed gradients with gradient separation/duration Δ/δ={74/12, 54/12, 34/12 ms} for effective diffusion times t_{diff} {70, 50, and 30 ms}, and trapezoidal cosine-modulated oscillating gradients with 1 cycle and Δ/δ = 46/40 ms for t_{diff} = 10 ms. TR/TE = 3000/116 ms, spatial saturation bands were used for a reduced FOV = 16 x 16 mm, image size 64 x 64, slice thickness 1 mm. DTI fitting was performed on the 30 ms diffusion time volume using an iterated weighted least squares method [99] in MRTrix3 [94]. SSIFT was calculated as described in Chapter 4.

DSC. A spoiled gradient echo (GRE) sequence was used to acquire a 30-minute timecourse with 999 time points. A bolus of 0.6 mmol/kg gadolinium (gadobutrol/Gadavist, Bayer HealthCare Pharmaceuticals, Whippany, NJ, USA) was injected manually via jugular catheter over 15 sec after 30 baseline frames. TR/TE = 15.6/5 ms, flip angle 9º, FOV = 32 x 32 mm, image size 64 x 64, slice thickness 1 mm. First ΔR_2^* was calculated as:

$$\Delta R_2^*(t) = \frac{1}{\text{TE}} \ln\left(\frac{S_0}{S(t)}\right) \tag{63}$$

The Boxerman-Schmainda-Weisskoff method was used to correct for contrast leakage [135]. The arterial input function was determined using the automated method described by Carroll et al. [136]. CBV was calculated as the time-integral of the ΔR_2^* timeseries, and rCBV in the lesion normalized by that in the normal tissue.

Data Analysis

Univariate analysis. Statistical processing was performed using MATLAB (The MathWorks Inc, Natick, MA, USA). The Wilcoxon rank-sum test was used for each parameter to test group differences between tumor and necrosis. The contralateral normal-appearing tissue is shown for comparison but is not tested, as it is not independent from the lesions. Bonferroni correction for multiple comparison was applied to the significance levels. The single parameter values and significance are shown in Figure 25. Contrast is described as normalized by the joint tissue standard deviation to allow nondimensionalized comparison between parameters. I.e., contrast between samples X from tissues A and B is characterized by:

$$D_{A,B} = (\bar{X}_A - \bar{X}_B) \left[\frac{(n_A - 1)s_{X_A}^2 + (n_B - 1)s_{X_B}^2}{(n_A - 1) + (n_B - 1)} \right]^{-1/2} \tag{64}$$

where s_{X_i} is the standard deviation and n_i is the size of the sample X_i, respectively.

Multivariate analysis. We use penalized logistic regression to build a classification model from our data. This gives the probability of an outcome y given data x and parametrization η:

$$P(y|x,\eta) = \frac{1}{1 + e^{-\eta}} \tag{65}$$

For simplicity we model η as a linear model parameterized by β:

$$\eta = \beta_0 + \sum_{i=1}^{p} \beta_i x_i \tag{66}$$

where x_i is the value of the ith parameter for a given subject. These coefficients can be fit by minimizing the deviance D in the model likelihood:

$$\beta = \underset{\beta}{\text{argmin}}\, D(\beta, y) = \underset{\beta}{\text{argmin}}\, -2[(l(\beta, y) - l(\beta_s, y)] \tag{67}$$

where l is the log-likelihood of the model and β_s denotes the coefficients of a saturated model (i.e., the number of parameters is equal to the number of data points). Here the likelihood function depends on the link function (logit) and is given by:

$$l(\beta, y) = \sum_{i=1}^{n} [y_i ln(\mu_i) + (1 - y_i) ln(1 - \mu_i)] \tag{68}$$

where n is the number of subjects, y is the outcome (0 for necrosis, 1 for tumor), and μ is the value predicted by the model. This fitting for the model coefficients β, however, is a many-to-one map, making the optimization ill-posed. A penalized regression may stabilize this fit, as well as providing other advantages described below. With a penalty R on β, the fitting objective takes the form:

$$\beta_{lasso} = \underset{\beta}{\operatorname{argmin}} D(\beta, y) - \lambda R(\beta) \tag{69}$$

- Lasso (Least Absolute Shrinkage and Selection Operator) [137] regression penalizes the β using the L$_1$ norm: $R = \|\beta\|_1 = \sum |\beta|$. This has an interesting property that stable solutions tend to fall along the major parameter axes, meaning many coefficients shrink to zero. The nonzero components of β inform which parameters to use for the model.

- Ridge regression [138] penalizes the β using the L$_2$ norm: $R = \|\beta\|_2 = \sqrt{\sum \beta^2}$. This method sacrifices bias in β to reduce estimation variance, leading to more stable solutions.

- Elastic net regression simply penalizes a linear combination of L$_1$ and L$_2$ norms, balanced by a design parameter α: $R = \left(\frac{1-\alpha}{2}\|\beta\|_2 + \alpha\|\beta\|_1\right)$.

Our goal for this analysis is to determine what method provides the best predictive model of the lesion type in our rat data to inform how processing should be done in future human studies. We will compare unpenalized, lasso, ridge, and elastic net regression on our data. Additionally, since lasso can be used to reduce the dimensionality of the model, we will assess combining this with ridge regression in a two-step process.

Each fitting method (unpenalized, lasso, ridge, and elastic net) was performed using *lassoglm* in MATLAB (The MathWorks Inc., Natick, MA, USA). The regularization parameter λ in lasso, ridge, and elastic net was optimized using cross-validation minimizing the deviance between the fitted and saturated models. To prevent overfitting, the maximum λ within one standard error of the minimum was chosen (Figure 27). The parameter α in elastic net was optimized by minimizing the Bayesian Information Criterion (BIC) of the model, defined by:

$$BIC = (N_p + 1)\ln(N_k) + D(\beta, y) \tag{70}$$

where N_p is the number of nonzero β coefficients. The model's ability to significantly differentiate the two outcomes was tested using a Chi-squared Test with degrees of freedom N_p, testing the difference in deviance between the fitted logistic model and a null (constant) model:

$$p = 1 - \text{CDF}_{\chi^2}(D_0 - D) \tag{71}$$

5.3 Results

Representative parametric maps. Example slices from 9L and radionecrosis lesions from each parametric map are shown in Figure 24. The APT and NOE methods both show decreased values in radionecrosis, while they show opposite trends from each other in the tumor. Inter-subject variability in CEST was high, as seen in the contralateral normal-appearing tissues for the two subjects in APT and NOE maps. PSR and R_{1f} both show similar trends in contrast, with lesions being hypointense, indicating loss of macromolecular content (e.g., myelin) compared to normal tissue. T_2 measurements showed poor contrast in the tumor but were sensitive to the highly necrotic region near the isocenter in radionecrosis. SSIFT shows elevated signals in the tumor and slightly elevated signals in the region surrounding the highly necrotic region of radionecrosis, possibly reflecting inflammatory infiltrative cells detectible by the size selective filter. MD shows little contrast between the tumor and normal tissue, but high contrast between radionecrosis and the contralateral tissue. Interestingly, MD shows increased values in the whole hemisphere ipsilateral to the radiation treatment while T_2 is unchanged outside of the necrotic core. DSC also showed high inter-subject variability. In the subject shown, the tumor was hyperintense relative to normal tissue, though one subject showed an rCBV value < 1. Radionecrosis had highly heterogeneous lesions in rCBV, with ROI-averaged values around 1. One 9L subject was excluded due to severe susceptibility distortions. DSC data from one subject was additionally excluded as there was no signal change with injection, so fitting could not be performed. This leaves n=5 tumor subjects for CEST, qMT, and Diffusion and n=4 for DSC. We, therefore, include the DSC results in Figure 25 for comparison but exclude them from the multiparametric analysis to improve statistical power.
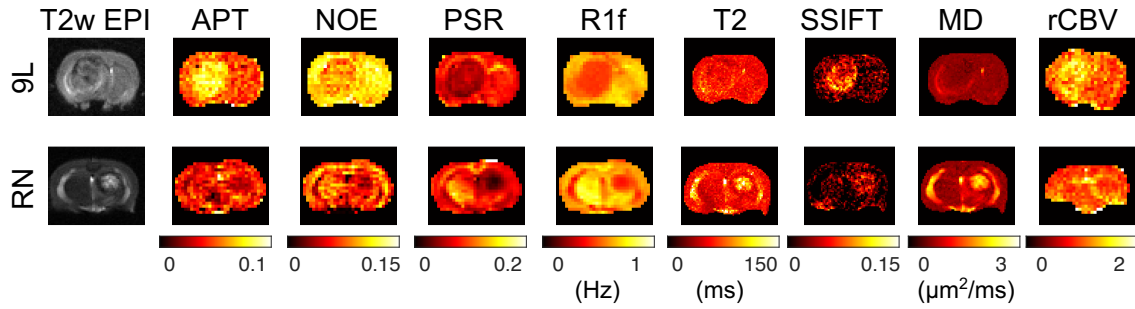
Figure 24. Representative parametric maps. The 9L lesions (top) are in the image-left hemisphere and the radionecrosis lesions (bottom) are in the image-right hemisphere.

Comparison of single-parametric contrast patterns. Figure 25 shows the mean values and standard deviations of each assessed parameter across subjects in tumor (9L), radionecrosis (RN), and contralateral normal-appearing tissues (CN). The SSIFT method presents the highest contrast between both 9L vs. RN, indicating that the density of cancer cells is highly specific to 9L tumor lesions. APT (mobile proteins and peptides) and MD (sensitive to cellularity) were also discriminators between 9L vs. RN. R_{1f} estimated by qMT had high contrast between both 9L and RN vs. CN, indicating that loss of myelinated tissue differentiates CN from the other tissues. PSR also had high raw contrast but a larger inter-subject variation. PSR and T_2 were unable to distinguish between 9L and RN within a standard deviation. Similarly, rCBV and APT lacked contrast between RN vs. CN, while NOE and T_2 lacked contrast between 9L vs. CN.
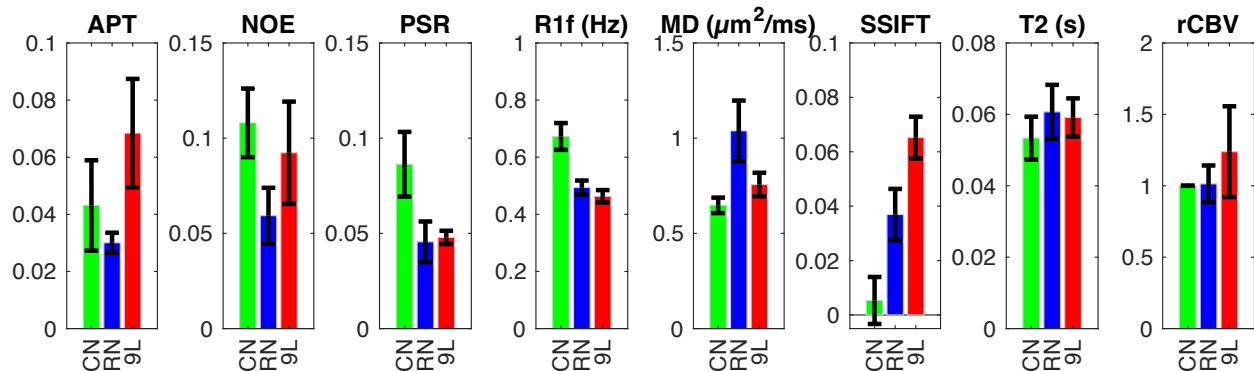
Figure 25. Comparison of sample distributions using single parameters. ROI-averaged means for contralateral normal-appearing tissue (green), radiation necrosis (blue), and 9L tumor (red) are shown, with error bars denoting the standard deviation. Using a Wilcoxon rank-sum test, RN and 9L were significantly different to $p < .01$ using SSIFT, MD, and APT.

Comparison of multi-parameter contrast patterns. For visualization, Figure 26 shows a comparison of multidimensional contrast within the three main categories of MRI methods, i.e., parameters that can be obtained from the same acquisition (MD being a subset of the SSIFT data). Ellipses denote the eigenvectors of the covariance matrices of each tissue. ROI-averaged parameter values show high covariance in the qMT and CEST parameters. MD and SSIFT seem to be less co-dependent, indicating that they offer complementary information. This is expected since MD relies on a single t_{diff} experiments while SSIFT relies on the t_{diff} dependence. The joint diffusion metrics have the highest ability to differentiate 9L from RN. Notably, the ability of CEST to differentiate both lesions from normal tissue was substantially improved by combining APT and NOE measurements compared to the metrics on their own, likely due to APT and NOE having opposite trends of contrast between 9L and CN (Figure 25).
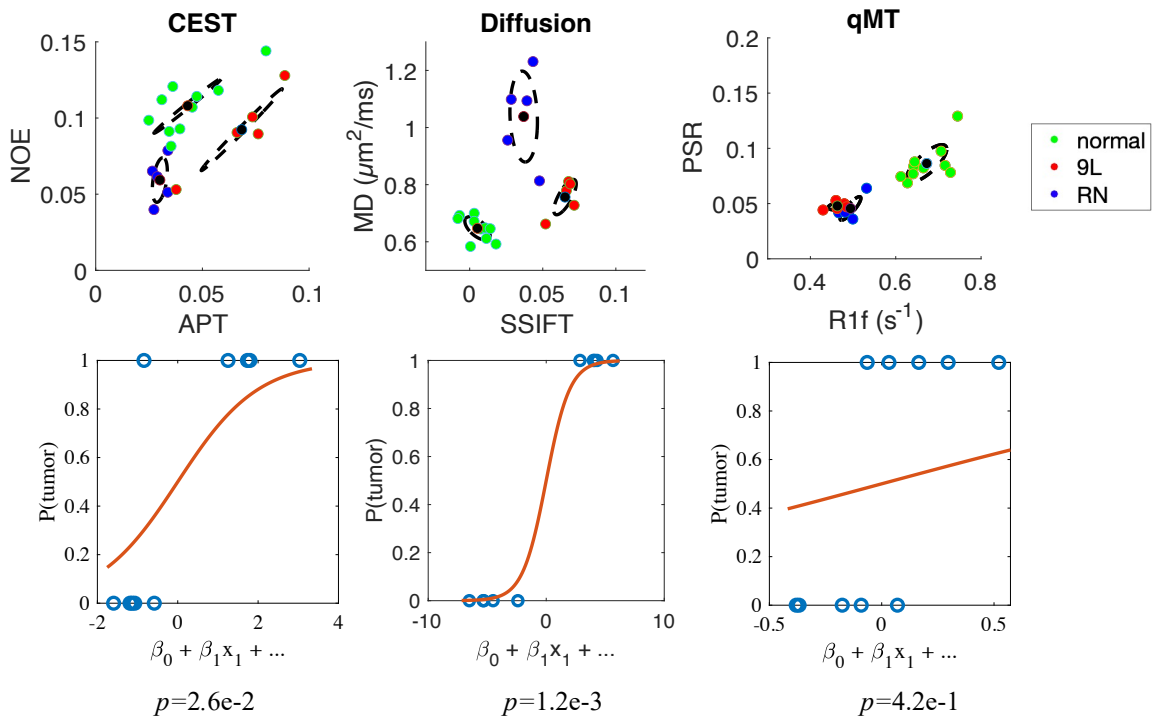
Figure 26. Multidimensional contrast for single acquisitions. (top) Dashed ellipses represent the covariance matrices of each tissue, with the axes along the normalized eigenvectors with length of the eigenvalues. Colored dots represent ROI-averaged values for 9L tumor (red) and radionecrosis (blue) subjects. Normal-appearing tissue (green) from both cohorts were grouped. (bottom) Ridge logistic regression using each set of two parameters was also performed to evaluate

how predictive each method was on its own. The diffusion metrics showed the lowest deviance between the data and model.

Optimization of classification protocol. Figure 27 shows example optimization for the regularization parameters λ and α (elastic net). Figure 28 shows fitted curves for unpenalized, lasso, ridge, combined lasso and ridge, and elastic net optimization, along with BIC and p-values for each. Lasso and elastic net both reduced the dimensionality from 7 parameters to 3: SSIFT, ADC, and APT. Combining lasso and ridge regression generated the model with the lowest deviance between the model and data, and best model for information efficiency (BIC), and the greatest statistical difference from the constant model (*p*-value). The linear model generated with this method was η = -2.98 + 155*SSIFT – 8.50*MD + 62.7*APT. Interestingly, this model had higher BIC (9.5) and *p*-value (3.6e-3) than the model comprising only diffusion metrics (BIC=7.3, *p*=1.2e-3). The deviance, which is the criterion by which the lasso step selected the parameters to pass to ridge regression, was lower in the full model (3.1 vs. 4.3). Including APT may therefore improve accuracy, though due to the lack of a test cohort the difference is undetermined.
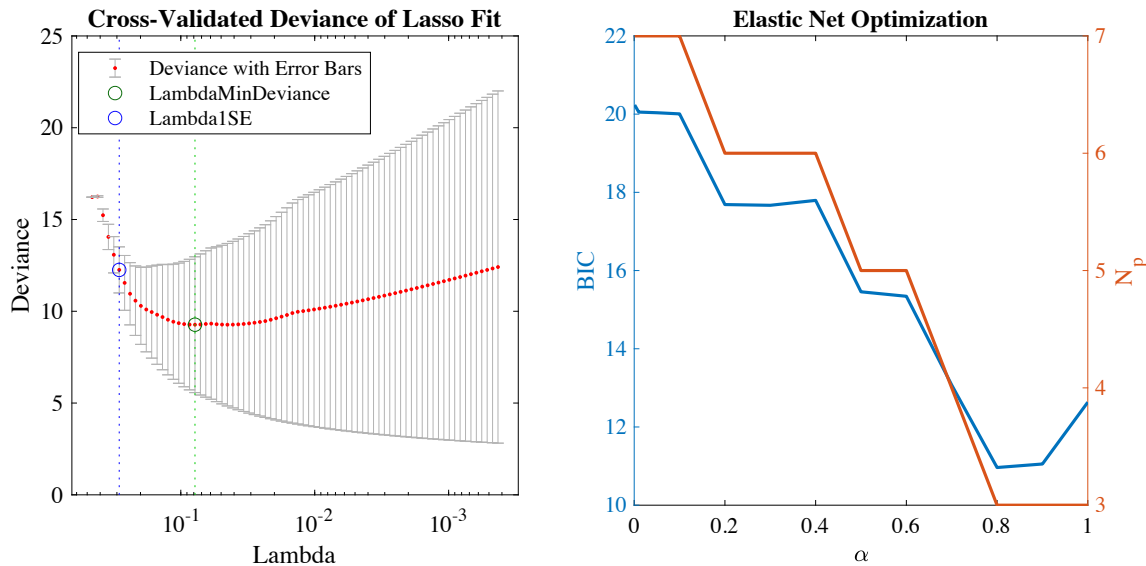
Figure 27. Optimization of design parameters. Left: cross-validation of the model fitted with a range of regularization parameters. The value giving the minimum deviance (green circle) was identified and the largest lambda within was standard deviation (blue circle) was used for our model. Right: optimization of α, which balances the L1 and L2 norm terms in elastic net fitting. The objective for this optimization was the BIC (blue curve), which has dependence on the number

of parameters (red curve). Larger values of α weight the L1 norm more heavily, which leads to fewer non-zero coefficients.
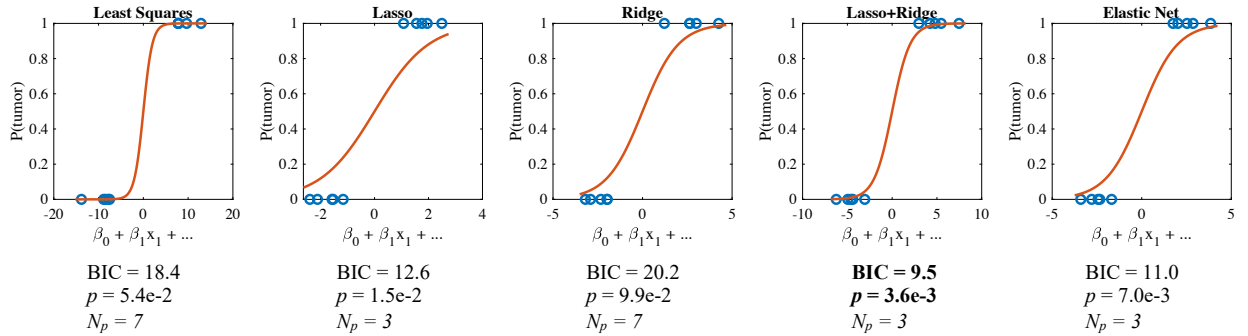
Figure 28. Fitting results from different penalty schemes. The blue scatter points indicate the linear model on the x-axis and the known outcome (tumor=1, necrosis=0) on the y-axis. The red curve is the fitted logistic function. BIC and Chi-squared Test p-values are shown under the curves. The number of non-zero predictor coefficients N_p are shown as well. Combined lasso and ridge had the strongest results.
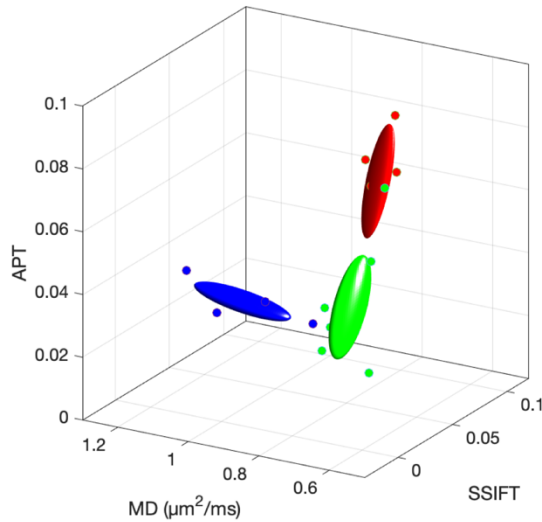
Figure 29. Multidimensional contrast of SSIFT, ADC, and APT. The ellipsoids are centered on the parameter means and depict the eigenvectors of the covariance matrices for the three tissues: 9L tumor (red), radionecrosis (blue), and normal-appearing tissue (green). Colored dots are the

ROI-averaged parameter values for individual subjects. The 2D projections of each pair of parameters are shown as ellipses.

SSIFT contributes high contrast to the multiparametric model. To view the role of SSIFT in this source of contrast we compare it to the other combinations of parameters. Figure 30 shows ridge regression performed on SSIFT and lasso+ridge regression performed on the remaining parameters. Model selection with the remaining parameters yielded MD and APT with nonzero coefficients. The deviance, BIC, and *p*-value of the logistic model with SSIFT alone were all lower than the combined MD and APT. This data does not therefore indicate that multiparametric MRI performs better than SSIFT alone, and the difference in deviance between the two models is not statistically significant with a Chi-Squared test.

$$D = 1.74$$
$$BIC = 6.3$$
$$p = 5.0\text{e-}4$$

$$D = 3.2$$
$$BIC = 10.2$$
$$p = 4.9\text{e-}3$$
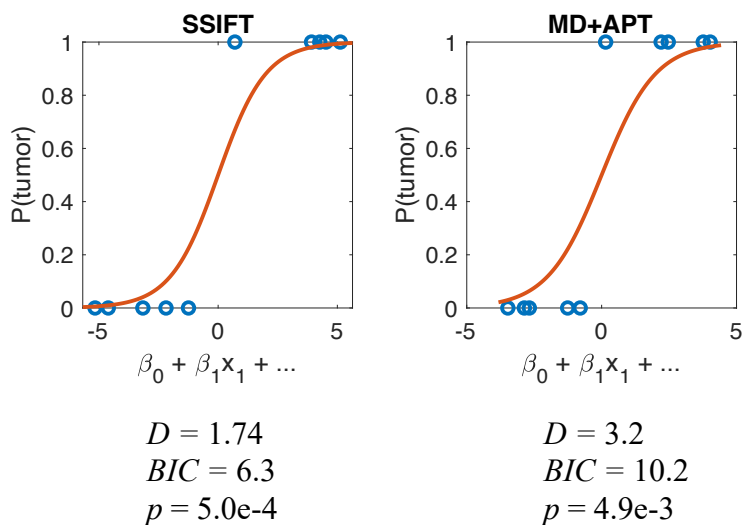
Figure 30. Logistic regression comparison of multiple parameters and SSIFT alone. Ridge regression on SSIFT alone (left) better fits the data than the two-step logistic regression applied to all other parameters. Lasso yielded MD and APT as the non-zero coefficients. Models were assessed using deviance, Bayesian information criterion, and p-value; smaller is better for each metric.

Diffusion model with test data gives full classification. Finally, while our number of subjects including all parameters was limited, additional diffusion (SSIFT and MD) data could be pulled from the analysis in Chapter 4 to further test the diffusion model shown in Figure 26. This training data comprises 1 radionecrosis and 7 tumor subjects. The test points are shown in Figure 31

compared to the previous model. The diffusion model fit the training data significantly better than the constant model ($p < 0.01$). Setting a threshold to $P(tumor) > 0.5$, there is 100% classification using this model among the training and test data.
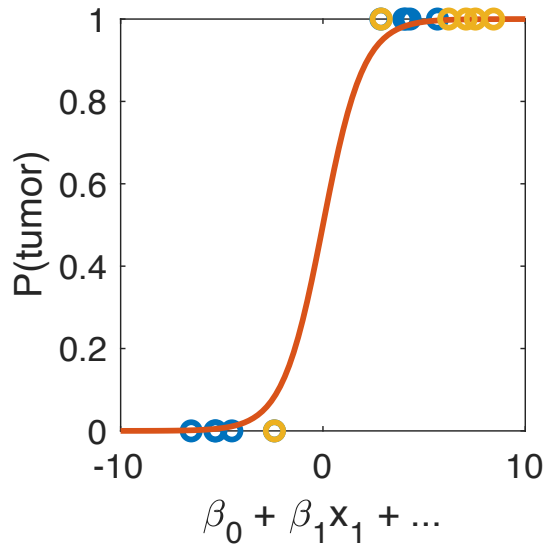
Figure 31. Training vs. Test data for a diffusion-based model. The SSIFT+MD model fit using the two-step logistic regression from our multiparametric data (blue) was tested with the remaining data from our previous study (yellow).

5.4 Discussion

Quantitative MRI methods have varying trends of contrast, supporting the claim that they are sensitive to different physiological features. Radiation necrosis is characterized by many such features, so utilizing multiple methods can help corroborate the classification of lesions. In this study, we applied methods probing cellular, vascular, and molecular features of tissue, investigating the contrast between tumor and radiation necrosis in a preliminary cohort of rat models. We found useful contrast between tissues in diffusion, CEST, and qMT methods. To investigate how metrics derived from these methods relate to each other, we compared contrast in 1-dimensional and higher-dimensional space. We also investigated the practicality of combining these methods into a single classifier. Using penalized logistic regression, we also applied a binary classification model to differentiate radiation necrosis from tumor. These preliminary results show that (a) these quantitative MRI techniques have varying forms of contrast in radionecrosis and tumors, (b) CNR can be improved between the groups using a joint multidimensional contrast, and

(c) generalized linear models, particularly logistic regression, are able to separate radiation necrosis from tumor. These results indicate multiparametric MRI may be worth pursuing in human studies, and we here demonstrated a framework of how to choose, combine, and analyze multiparametric MRI.

The data provided some additional promising insights for the role SSIFT can play among other quantitative methods. The multiparametric model that best fit the data included SSIFT, SSIFT was the best single parameter model, and SSIFT alone performed better than a combination of all other parameters. SSIFT had 100% classification using all animals combined in the test and training data. This is consistent with the theme of this thesis, that the cell size distribution may be a better discriminator between radionecrosis and tumor. However, since none of these results were statistically significant, our conclusion is not that SSIFT can definitively meet this challenge better than other metrics can, but rather that it is an important parameter to include in future larger, human studies.

This study was motivated by the apparent lack of a sufficiently accurate biomarker in clinical imaging of recurrent tumors and radionecrosis. Our proposed strategy to overcome this deficiency is to combine multiple parameters in a multidimensional domain of quantitative imaging parameters. Conventional imaging, such as anatomical T_1- or T_2-weighted images, may still have a role as well with novel processing methods. The analysis of texture features has been enabled by advances in image analysis and machine learning. These radiomic methods have been shown to improve diagnostic accuracy for distinguishing radiation necrosis and recurrent tumor [139]. Combining quantitative MRI with these radiomic methods may further enhance the classification performance.

The biggest limitation to this study is the small sample size. This impacts our results in a few ways. First, the small sample adds uncertainty to our estimation of parameter means and does not allow much hypothesis testing. Second, to compare raw contrast with different parameters, contrasts were normalized by their covariance. However, this means the accurate estimation of contrast also requires accurate estimation of the population standard deviation, which we may not have sufficient sampling to perform. Third, when performing the penalized logistic regression, with the exception of the diffusion model, we do not have an adequate sample size to split our data into a training set to estimate the model parameters and a testing set to assess its ability to classify

data. While we were able to demonstrate that the outcomes were significantly different using our model, an assessment of diagnostic accuracy would have been enabled by larger sample sizes.

The contrast in the individual parameters generally matches previous studies, but the intersubject variability in e.g., CEST and DSC makes it difficult to assess the methods. This is a common reproducible problem that many factors such as shimming, hardware stability, and image preprocessing may bias the measurements. For instance, although B0 heterogeneity is corrected through a voxelwise shift in the CEST peak fits, we found that in some subjects a frequency shift was concurrent with visible artifacts on the final image. This may be the source of some of the intersubject variability. As another example, DSC used a manual injection of gadolinium through a jugular catheter, which may have large variations in e.g., flow rates. The apparent lack of contrast in DSC, which is often used in humans for this clinical application, may be due to such factors. Additionally, animal models differ from humans. The tumor model used is a 9L gliosarcoma, which may differ in each pathophysiological feature targeted (cellular, molecular, and vascular). Finally, our model of radiation necrosis has been validated to present the same features as in humans, but the quantitative effects on each parameter may not be a true analog for necrosis in humans. We are therefore wary of making claims about the methods themselves based on this data, as human translation may yield different results. Instead, the goal of this study is to demonstrate the utility of multiparametric MRI, to use established methods to determine if SSIFT has added value, and to motivate both SSIFT and multiparametric MRI for use in future human studies.

CHAPTER 6

Rodent model of brain radionecrosis using clinical LINAC-based SRS

Chapters 4 and 5 described uses of rodent models of radiation necrosis. The LINAC-SRS method used in these studies was motivated by a lack of literature on how best to induce radiation necrosis in rodents without specialized equipment but while keeping clinically relevant features such as dose rate, beam quality, and an isotropic dose distribution. In this chapter, we therefore describe an observational study applying this method in mice. Details on the arcs and couch positions are provided to replicate the therapy. Data using high doses (100 Gy and higher max dose) has not been previously shown in LINAC-based rodent models. We therefore describe the time to lesion onset and track its volume over time. Histological validation of the pathological features induced by the therapy is also provided. This enables further study of imaging metrics in radiation necrosis such as what was described earlier in this thesis, and also allows expansion into other investigations of tissue response to high dose therapies.

The author acknowledges Guozhen Luo and Austin Kirschner for designing the treatment plan and performing the mouse and rat treatments; Xiaoyu Jiang, Jingping Xie, and Jing Cui for preparing tissues for histology; and Hannah Harmsen for providing an expert description of the histopathological features indicating radiation necrosis.

6.1 Introduction

Neurologic injury is generally a late side effect of radiation therapy, occurring months after the treatment has occurred. Histological findings include inflammatory changes such as reactive gliosis, demyelination, white matter necrosis, and vascular changes in both the white matter tracts and central gray matter [140]. Apoptosis of vascular endothelial cells may compromise the barrier between the circulatory system and neurologic tissue, as well as reduce the density of oligodendrocyte progenitor cells [140–142]. It is thought that both mechanisms contribute to radiation injury of neurologic tissue [142].

Radiation treatment for some neurologic diseases utilizes the purposeful injury of nerve or brain tissues. Examples of modern radiotherapy include the treatment of medically-refractory

trigeminal neuralgia [143], essential tremor and Parkinsonian tremor [144–147], epilepsy [148], and obsessive-compulsive disorder [149]. Typically, these are treated with high-dose short-course radiotherapy delivered in a focused and precisely designed treatment technique known as stereotactic radiosurgery (SRS).

More commonly, radiotherapy is used to treat malignancies of the central nervous system, both primary tumors of neurologic tissues as well as metastatic disease, which treatments are supported by numerous clinical trials [150–152]. However, there is a highly problematic clinical dilemma of differentiating tumor recurrence versus radiation necrosis, which is also known as pseudoprogression [153,154]. This confounding situation often leads to delay in management of the true ongoing pathology, which can have significant detriment to patient care [155]. Clinical factors have been associated with rates of radionecrosis, such as the volume of normal brain tissue receiving dose levels, e.g., 21 Gy for single-fraction SRS [156], maximum tumor diameter [157], and single-fraction versus multi-fraction SRS [158]. Unfortunately, radionecrosis is indistinguishable from tumor recurrence on clinical standard-of-care MRI with gadolinium (Gd)-based contrast agents due to the breakdown of blood brain barrier (BBB) in both types of lesions. Furthermore, besides dose constraints, what factors may help reduce the risk of radionecrosis are unknown.

It is impossible to study the effects of radionecrosis on neurologic tissues directly in healthy human brains and hence animal models of radionecrosis are necessary. Typically, radionecrosis is generated in one hemisphere of the animal and the contralateral hemisphere serves as a control. It is a challenging procedure due to the small size of rodent brains. To this end, specialized small animal irradiators have been developed and successfully implemented to induce radionecrosis in mice [159,160], but such a model requires dedicated preclinical equipment that is not broadly available. Clinical equipment such as Gamma Knife has been used in rats [161,162] and mice [108,163,164]. These models use the high precision of Gamma Knife SRS to induce radionecrosis in small animal brains and have been extensively characterized using imaging and histology. However, Gamma Knife is not widely available to clinics, which limits its usage in many institutions. To overcome this disadvantage, the linear accelerator (LINAC), which is more commonly used in clinics, has been applied in rats [165,166]. This model uses a single beam delivery but suffers toxicity such as moist desquamation dermatitis from a 60 Gy treatment [167]. This may limit the maximum deliverable dose using a single beam, which is undesirable to study

radionecrosis induced by higher doses such as 140 Gy used in the SRS treatments of tremor patients [147,167]. Moreover, rats are relatively more expensive and less used than mouse models particularly in cancer research. This may limit the ability to study large cohorts to investigate several hypotheses and make strong statistical conclusions. It is of interest to develop an animal model of brain radionecrosis in both rats and mice that allows the animals to tolerate such high maximum doses.

LINAC-based SRS with multiple arcs is becoming more widespread and growing in availability, which allows efficient treatment of both small and large neurologic tumors with minimized dose spillover to surrounding normal-appearing brain tissues [168]. Recently, clinical studies have used LINAC-based SRS to treat essential tremor patients [147,167]. These studies use single fraction, highly-focused (~4 mm), and high dose (maximum 162 Gy) plans to irradiate the ventral intermediate nucleus (VIM) of the thalamus and induce radionecrosis. A recent study has shown the dosage deliveray can be accurate with an overall three-dimensional uncertainty of 1.1 mm in patients and sub-mm in each dimension [169]. This approach makes it possible to generate radionecrosis in small animal brains with high accuracy and high dosage. However, LINAC SRS in clinics typically uses cone sizes ≥ 4 mm, which is comparable to the size of the mouse brain hemisphere. It is so far unknown if the dose volumes of this clinical approach could cause similarly severe toxicity as in whole brain or whole hemisphere treatments in small animals. This could impact the development of radionecrosis and may shorten animal lifespans, both of which are not desirable. In this work, we translate such a clinically available LINAC-based SRS protocol to both rats and mice, and investigate the incidence, accuracy, progression, and toxicity of this brain radionecrosis model.

6.2 Methods

Radiation treatment planning. Treatment plans were developed mimicking high-dose SRS patient treatment plans, including the use of up to 10 rotational arcs focused on a single isocenter. The iPlan® system (Version 4.5.5; Brainlab company; Munich, Germany) was the treatment planning system to design all the plans for the mice. A high-resolution CT (voxel size of $0.2 \times 0.2 \times 0.2 \text{mm}^3$) of a same-age mouse was imported into iPlan® RT dose for treatment planning. Our smallest stereotactic radiosurgery SRS cone of 4 mm from Brainlab was selected to minimize dose to surrounding brain tissue. The isocenter was placed at one-third to the left side in the left to right

(LR) direction, midline in the anterior to posterior (AP; i.e. rostral-caudal) direction, and midline in the superior to inferior (SI; i.e. dorsal-ventral) direction. For this study, we used three different prescription levels of 140 Gy, 100 Gy, and 60 Gy with five mice each. The maximum dose of 140 Gy was chosen to replicate the range of SRS treatments for tremor patients [147,167,169]. One cohort of six rats was treated with 140 Gy using a similar plan to test feasibility across species. To further spare the normal tissue from the radiation damage, arc therapy instead of static fields was chosen to deliver the dose. The geometry of every plan, including the couch and gantry angles, remain the same for different dose levels, and the numbers of monitor units (MUs) were renormalized to deliver the prescription dose to isocenter. A total of ten arcs with the same dose weight of each arc to isocenter were utilized. Table 2. shows the gantry and couch angles of the plans both in the Varian convention and the matching IEC convention.

		1	2	3	4	5	6	7	8	9	10
Couch angle (Varian convention)		260°	245°	230°	215°	200°	160°	145°	130°	115°	100°
Couch angle (IEC convention)		280°	295°	310°	325°	340°	20°	35°	50°	65°	80°
Gantry angle (Varian convention)	Start	150°	30°	150°	30°	150°	210°	330°	210°	330°	210°
	End	30°	150°	30°	150°	30°	330°	210°	330°	210°	330°
Gantry angle (IEC convention)	Start	30°	150°	30°	150°	30°	330°	210°	330°	210°	330°
	End	150°	30°	150°	30°	150°	210°	330°	210°	330°	210°

Table 2. Table and Gantry angles of rodent SRS treatments. Plans shown in both Varian convention and IEC convention. All the treatments were administered with a system commissioned in Varian convention.

Radiation plan delivery. The animals used were age-matched female CD-1 mice (Envigo; Indianapolis, IN, USA) and male Fischer rats (F344/NHsd; Envigo; Indianapolis, IN, USA). Mouse and rat radiation was administered with a clinical Novalis TX™ (Varian Medical Systems, Inc; Palo Alto, California). All the animals were planned and treated in head-first prone position. During treatment, each animal was under anesthesia with 2%/98% isoflurane/O_2, and was placed in a 3D printed animal holder to minimize motion. On-board imaging by cone-beam CT (CBCT)

was used to target the brain isocenter. CBCT was performed with the high-quality head protocol with a full bow tie. A reconstruction size of 5 × 5 cm, thickness of 2 mm, and matrix size of 512×512 pixels were used. After the CBCT, coregistration with the planning CT was performed on the console and the couch was moved to plan isocenter by automated robotics. Figure 32 shows the axial, coronal, and sagittal views with isocenter and brain contour overlays. After the couch was moved to the plan isocenter, all ten planned arcs were delivered. The total radiation delivery time including onboard imaging was less than ~30 minutes for the highest dose cohort. Less delivery time is needed for smaller dose levels due to the use of fewer MUs.
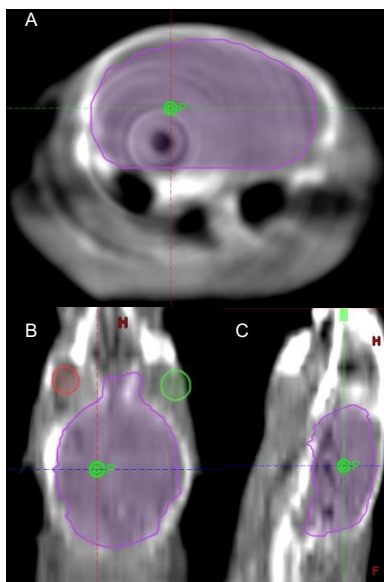
Figure 32. CBCT alignment. Cone beam CT (CBCT) images in Axial (A), Coronal (B) and Sagittal (C) views with isocenter and brain contours

Monitoring and confirmation of lesion progression. Radionecrotic lesions were identified in mice by Gd-enhanced T1- and T2-weighted 2D fast spin echo MRI with an image size 128x128 and a slice thickness of 500 μm using a Bruker (Bruker Corporation; Billerica, Massachusetts) 7.0 Tesla, 16 cm bore horizontal scanner. All animals were anesthetized using 1-2%/98% isoflurane/O_2. A dose of 2.5 mmol/kg of Gd contrast (gadobutrol, Gadavist; Bayer HealthCare Pharmaceuticals Inc; Whippany, New Jersey) was administered intraperitoneally (IP) 10 minutes prior to imaging in mice and 0.6 mmol/kg via jugular catheter injection in rats 15-20 minutes prior to imaging. One rat had an unexpected delay after injection so it was excluded from the volume analysis. Mice with 100 and 140 Gy treatments were imaged over the span of 90 days from treatment. Mice with 60 Gy were imaged at 1, 2, 4, and 8 months. Rats with 140 Gy were imaged at a single time point at

8 weeks. At the final time point, animals were sacrificed via transcardial perfusion of 10% formalin, and brain tissues were fixed by immersion in formalin for two days, and then stored in 70% ethanol. Hematoxylin and eosin (H&E) staining with a slice thickness of 8 μm was used in the histology analysis for confirmation of radiation necrosis.

6.3 Results

Dosimetry: Arc therapy allows normal tissue sparing in mice. The relative isodose distribution lines and arc arrangement in mice are shown in Figure 33. This figure shows that the multiple arc technique can significantly reduce the dose to surrounding tissues. In mice, the 50% isodose line has slight spillage into the contralateral brain, with 1% hemispheric volume above this dose. In rats, the maximum dose in the contralateral brain was 32% (45 Gy for our 140 Gy cohort). Figure 34 and Figure 35 include relative dose-volume histograms in the ipsilateral and contralateral hemispheres for both mice and rats, respectively.
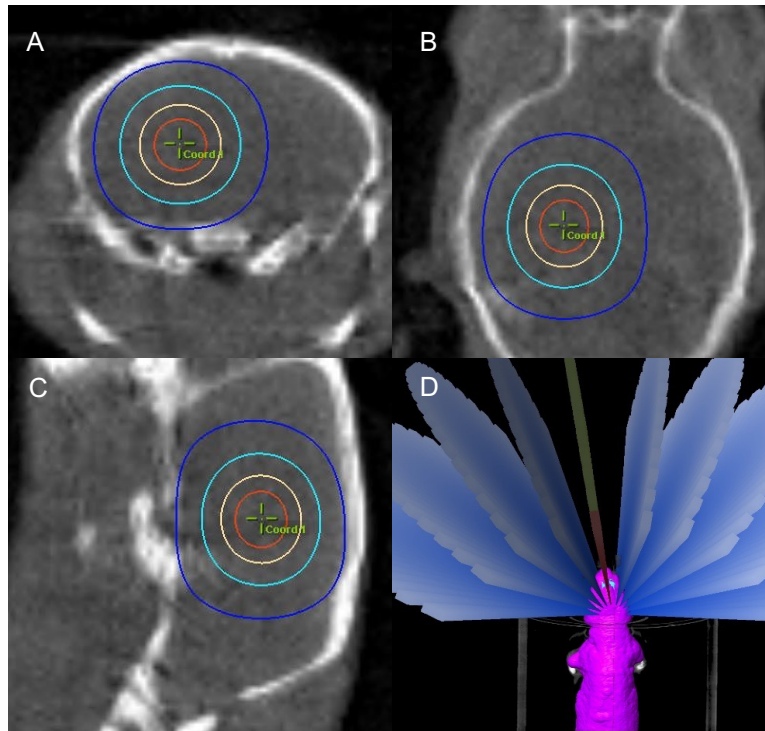
Figure 33. Isodose lines in mouse SRS plan. The isodose distribution lines for Axial (A), Coronal (B) and Sagittal (C) views for 90%, 75%, 50% and 25% dose level in a mouse brain. (D) shows the arc arrangement of the plan.
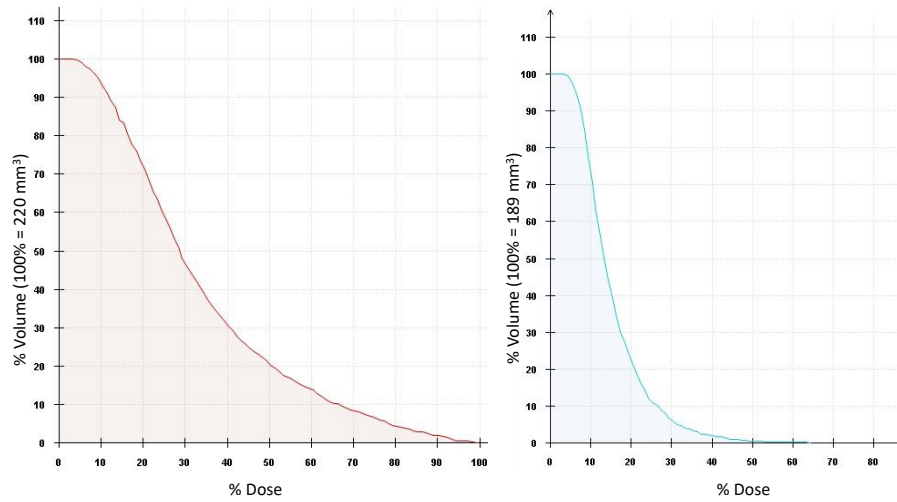
Figure 34. Mouse Dose Volume Histograms. Dose-volume histograms of ipsilateral (left) and contralateral (right) hemispheres in mice. Maximum dose in the contralateral hemisphere is 65%.
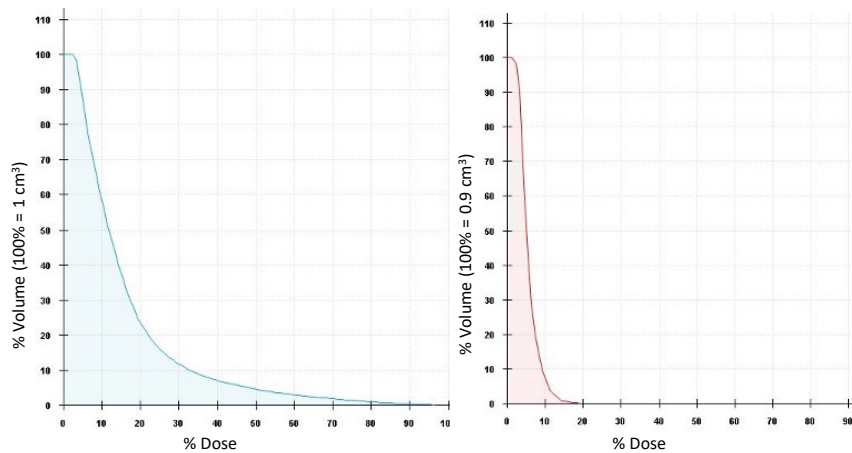
Figure 35. Rat Dose Volume Histograms. Dose-volume histograms of ipsilateral (left) and contralateral (right) hemispheres in rats. Maximum dose in the contralateral hemisphere is 32%.

High doses allow early time to lesion onset. All irradiated rats and mice developed apparent necrosis before sacrifice, except for one 60 Gy subject who did not survive until the 8-month time point. All mice treated with 140 Gy first showed Gd-T1w MRI hyperintensity at 2 weeks

following treatment. Two of the 100 Gy mice showed enhancement at 4 weeks and all showed enhancement by 6 weeks. The 60 Gy mice first showed enhancement at 8 months. Rats receiving 140 Gy showed radionecrosis at 8 weeks.

Lesions show steady progression over time. Lesion volumes for the three groups of mice are shown in Figure 36. Volume was measured by hand-drawing ROIs containing regions that were hyperintense on Gd-T1w MRI in the treated hemisphere relative to the contralateral side. Figure 37 shows a representative slice in a 140 Gy mouse at week 2 with the corresponding ROI. At the initial time point (2 weeks) the 140 Gy mice had a volume of 26.5 ± 1.0 mm^3 (mean $\pm$ SD) and grew to 97.6 ± 26.8 mm^3. The two 100 Gy subjects showing necrosis at 4 weeks had volumes of 7 and 10 mm^3. These subjects showed much larger volumes (both 29 mm^3) at week 6 than those first presenting at that timepoint (11-16 mm^3) and continued to show larger lesion growth (1.9 mm^3/day versus 0.6 mm^3/day). Five rats showed enhancement volume of 143 ± 20 mm^3 at 8 weeks, which is substantially larger than the mice at the same dose and time point (69 ± 29 mm^3).
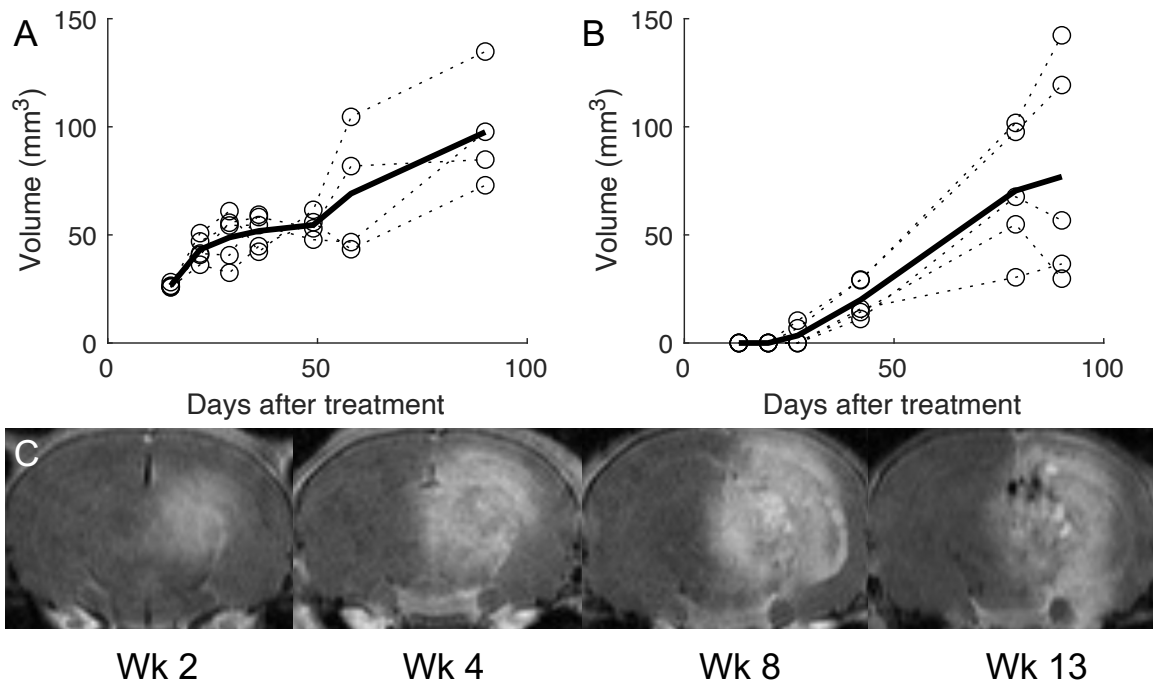
Figure 36. Radiation necrosis lesion progression over time. Volumetric assessment of radiation necrosis over time as assessed by Gd-MRI in 140 Gy (A) and 100 Gy (B) mice. Dashed lines are

the individual volume trends and the solid bold line is the mean across subjects. Panel (C) shows a representative timecourse in Gd-T1w images in a 140 Gy mouse.

Targeting accuracy is comparable to human treatments. Targeting accuracy was determined by first calculating the geometric centroid (i.e., the average position of all voxels) of the lesion ROI as a surrogate for the delivery isocenter. The 140 Gy mice showed the tightest volume distribution and earliest time point with a visible lesion on Gd-MRI, so the images of this group at the 2 week time point were chosen to most accurately represent the beam location. Because the only difference in treatment between the different groups of mice was the number of MUs delivered, which should not affect geometry, the accuracy of the 140 Gy group is sufficient to characterize all groups. The prescription point was then estimated as the point 50% SI, 50% AP, and 33% LR of the brain on the MR images. The Euclidean distance between the prescription point and the center of the lesion defined the delivery accuracy. Figure 37A-B shows a representative subject with the two points overlaid. Figure 37C summarizes the result for all subjects. The mean distance of the five subjects was 1.0 ± 0.2 mm, which is comparable to the targeting accuracy of 1.1 mm in patients [169]. The largest variance was in the SI direction (mean distance 0.7 mm), possibly due to motion from the subject breathing.
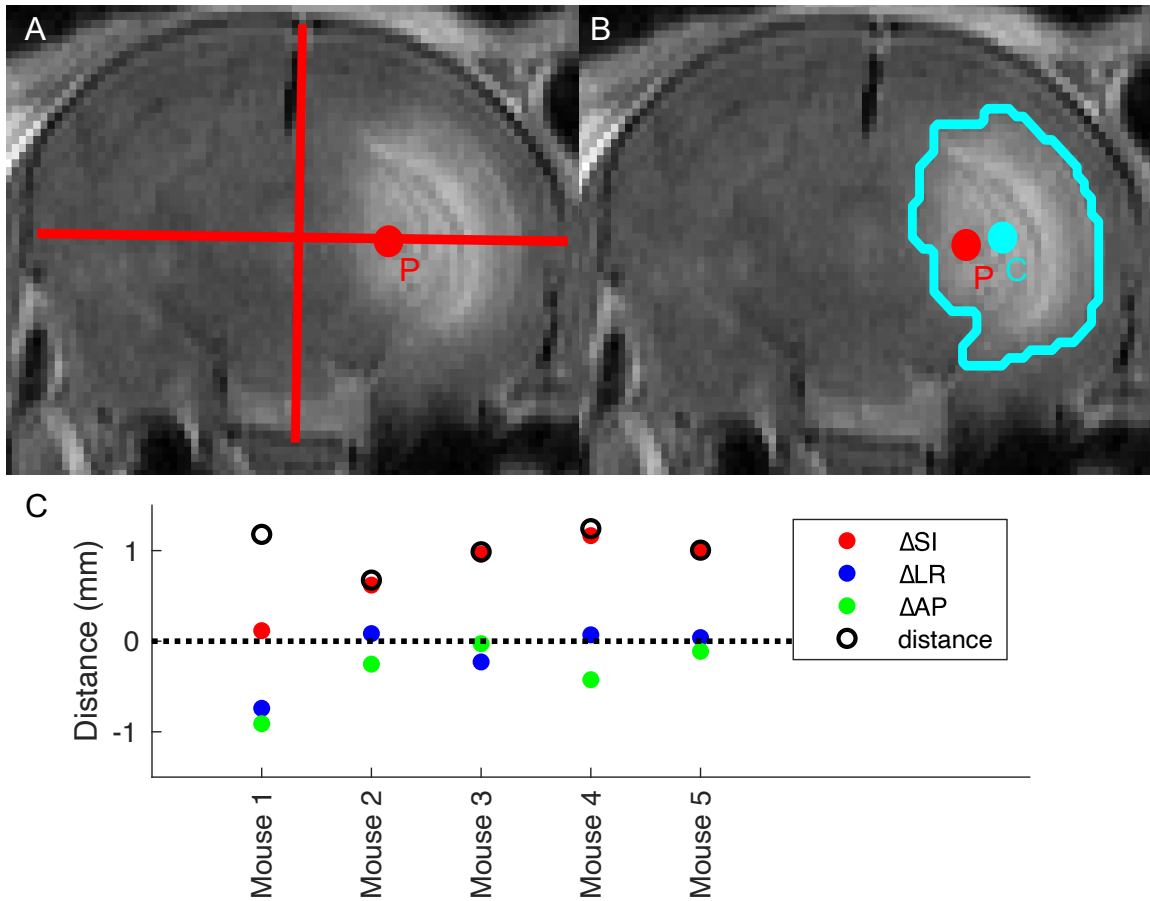
Figure 37. Calculation of accuracy by difference between anatomy and center of necrosis.
(A) The prescription point P as was defined by 50% of the brain in the SI direction, 50% AP, and 33% LR. (B) ROIs were hand-drawn around the region of hyperintensity present in only one hemisphere. The geometric centroid C of the ROI (i.e., the mean coordinates of all ROI points) was used to estimate the isocenter. (C) Distance in all three dimensions of the prescription to the center of the ROI (i.e., P minus C). Total distance is the Euclidean norm of the points. The subject denoted "Mouse 1" is displayed in (A) and (B). Both panels show slice of point P.

Histology: Tissues at endpoint show hallmarks of radionecrosis. Digital H&E cross-sections of excised brains were viewed by a pathologist using QuPath-0.3.0 [109]. All sections demonstrated evidence of radiation injury as shown in Figure 38, including vascular telangiectasia, vessel wall hyalinization, fibrinoid necrosis of blood vessels, intravascular thrombosis, edema, neuron and parenchyma loss, gliosis, microcavitation, cavitation, infiltrates of foamy macrophages, and

neutrophil infiltration. Microhemorrhages were encountered in nearly all cases, and a larger hemispheric hemorrhage was present in one case. Most histologic changes were confined to the hemisphere ipsilateral to the radiation; however, two cases showed changes in the contralateral hemisphere. The case with a large hemorrhage had extension of the hemorrhage across the corpus callosum into the contralateral hemisphere, and one case had dilated vessels extending into the contralateral thalamus.
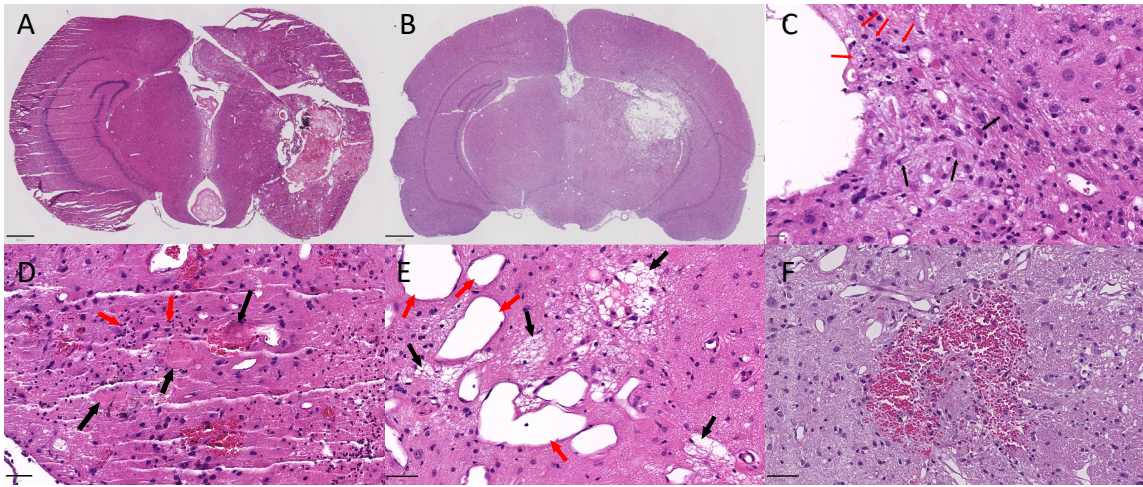
Figure 38. Histological validation of radionecrosis. Example slides using H&E staining in 140 Gy mice (A) and rats (B). Features indicative of radionecrosis include reactive astrocytes (C black arrows), foamy macrophages (C red arrows), thrombosis (D red arrows), neutrophils (D black arrows), microcavitation (E black arrows), vascular dilation (E red arrows), microhemorrhage (F), and gliosis (F). Scale bars are 800 μm (A), 1,000 μm (B), 20 μm (C), and 50 μm (D-F).

While the above features indicative of radiation effect were seen, there were differences between the various groups. While nearly all cases reviewed had vascular dilatations (telangiectasias), vessel wall hyalinosis and/or fibrinoid necrosis, microhemorrhages, and microcavitation with neuron loss, these features were relatively more prominent in the 100 Gy mice in comparison to the other groups (140 Gy mice and rats). Conversely, regions of cavitation, tissue necrosis, macrophage infiltrates, neutrophil infiltrates, and gliosis were more frequent in the 140 Gy mouse and rat groups.

SRS allowed low observed toxicity in mice. Some of the mice treated with 140 and 100 Gy showed alopecia on the region of the scalp near the isocenter. None of the 60 Gy mice or 140 Gy rats showed any alopecia. No moist desquamation, esophagitis, oral cavity irritation, or change in animal behavior was observed in any group. One 140 Gy mouse showed herniation of the brain midline at 5 weeks and was sacrificed. This mouse was included in volume measurements prior to but not including the observed herniation. One 60 Gy mouse was sacrificed without imaging prior to the 8-month timepoint due to severe hemorrhage.

6.4 Discussion

This study demonstrates the feasibility of a multi-arc LINAC-SRS-based small animal model of radiotherapy in rats and mice. To the best of our knowledge, this is the first study to generate radionecrosis in mouse brains using a clinical LINAC. Treatment planning on CT simulation as well as registration and alignment with high-resolution onboard CBCT allowed for accurate targeting in small animal brains comparable to that in patients. Successful delivery using a wide range of doses (60-140 Gy) demonstrates the flexibility of this method to accommodate even the ultra-high doses used in patients to date. The high incidence of radionecrosis in multiple species indicates this method can be applied to both rat and mouse tumor and/or necrosis models. The lesion volumes were tracked over time in the 100 and 140 Gy mice and showed growth over 13 weeks following treatment. The steady initial growth, high incidence, short time to onset, and low variance of lesion volume at the initial time point in the 140 Gy cohort are desirable characteristics of an animal model of radiation necrosis. The histopathological features of the tissues at their endpoints are consistent with radionecrosis. The dose-dependence of these features highlights a potential qualitative difference in injury induced by higher dose neuro-ablation techniques versus lower dose in cancer therapies, and motivates future study of this relationship.

Preclinical models in animals to evaluate novel radiotherapies, radioprotective pharmaceuticals, and imaging methods are an essential step toward human implementation in clinical radiation oncology. Although animal models of radiation treatment have existed for decades, keeping these models relevant to the rapidly emerging technologies in human care is nontrivial. For instance, clinical SRS has shown to have benefits over whole-brain radiotherapy (WBRT) in treating brain metastases [170], but requires accurate targeting that may be difficult to implement in mice [171]. Dedicated preclinical irradiators have grown in sophistication to meet

such challenges. Small animal irradiators with onboard imaging allow for highly accurate target localization and radiation delivery [172]. However, these machines generally do not fully replicate human therapies, for example, differing in dose rate and beam quality [173]. Furthermore, mice are sensitive to long durations of anesthesia [171], so the low dose rate of small animal irradiators may endanger the animals in the case of high-dose therapies. The use of clinical machines may therefore have advantages in cases where sub-millimeter targeting can be sacrificed for a more exact model of radiation. For this reason, several models of radiation necrosis in small animals have used clinical machines for irradiation. Gamma Knife has successfully delivered high doses (60 Gy prescribed at the 50% isodose line) to small volumes in mice [163], but clinical Gamma Knife generally suffers from a lower dose rate than LINAC-based methods (Liu et al., 2016) and may prolong an animal's time under anesthesia. Our treatment model in this study used a clinical machine to normalize effects of beam quality and treatment time on pathological response to radiation. The high dose rate of clinical LINAC facilitates high subject throughput and mitigates negative effects from prolonged time under anesthesia. In fact, modern LINACs that have flattening filter free (FFF) mode can deliver dose at least twice as fast as the LINAC used in our study.

Relative to other models of radiation necrosis using clinical LINAC, hypofractionated SRS enables higher doses in smaller volumes than previously published in mice. The plans used in this study were modeled after the highest doses used in patients with small treatment volumes. Our mice showed only mild observable toxicity in our maximum 140 Gy dose with multiple circular photon arcs. Such a high dose would not be achievable without severe toxicity using a single field beam. Because biopsy is not clinically accessible in many such CNS therapies, an animal model able to accommodate these doses allows further study of the effect of high dose radiation on tissues *in vivo*. Furthermore, an *in vivo* model accurately replicating human therapies which can be monitored over time by imaging histology or imaging allows for better testing of drugs and novel imaging methods.

The results of this study preliminarily demonstrate the feasibility of generating radionecrosis in both mice and rats using LINAC-SRS. BBB breakdown as indicated by Gd-MRI was used as a biomarker for necrosis, but a histology time-course could further elucidate what pathological changes occur other than detected by perfusion. BBB breakdown was also used as a marker to localize dose delivery and measure treatment accuracy. An alternative assessment of accuracy

performed by Kim et al. to characterize Cyber Knife targeting in mice was to sacrifice the subjects shortly after treatment and perform staining sensitive to DNA strand breaks [174]. DNA damage is likely a more direct biomarker than BBB breakdown for localizing radiation, but is unobtainable *in vivo*. Because eliminating geometric distortions between the excised tissue and the *in vivo* volume is not trivial [175], Gd-MRI may nonetheless have advantages for localizing radiation.

Chapter 7

Conclusion and future directions

In vivo imaging of the brain is a broad and rich field. Far beyond the scope of this thesis are applications using MRI, ultrasound, CT, or nuclear medicine combined with quantitative modeling and machine learning to perform image-guided neuromodulation and neuroablation, brain mapping with functional and structural connectivity, and assessing neurodegenerative diseases. Closer to the scope of this thesis are the clinical oncology applications of grading tumors, defining margins for treatment planning, and identifying tumor progression, pseudoprogression, and regression. There is currently a clinical need for better characterization of tissue for these applications, but it is far from trivial in the brain. Healthy intracranial tissues are highly complex, with vast heterogeneity in cell sizes, anisotropic fiber orientations, fractions of free water, arrangement of neuronal cell bodies and dendrite branches, number and type of glial cells, and degrees of myelination. Lesional tissue further complicates this, with inflammatory infiltrates, cerebral and cytotoxic edema, neoplastic cells of intracranial or extracranial origin, vascular fibrosis and angiogenesis, cellular death, axonal loss, demyelination, etc. A single pathological feature to fully characterize a lesion could be confounded by a host of other effects, which presents a tremendous challenge for radiologists, biologists, statisticians, biomedical engineers, physicists, and oncologists in academic, industry, and clinical roles to solve.

In this thesis, we highlighted how many of these challenges could be met by filtering signal by cell size to identify malignant lesions. We provided evidence that this method has high specificity to cancer in animal models and shows promise in a few human subjects. There are a few avenues of progress that could be made following this work, including further validation of the SSIFT contrast, extension into a quantitative model, and further recruitment of human subjects.

Validation. In this work we used microscopy correlates with *in vitro* data and histological correlates with *in vivo* data to inform how SSIFT contrast could be best interpreted. This showed that the method is sensitive to two key discriminators (cell size and count) between tumor and radionecrosis, which is necessary to validate that it can be used as a specific classifier between the lesions. While this objective was met in a qualitative sense – i.e., it was shown that the number of

nucleated cells was much higher in tumor, and that *a priori* information using *in vitro* data demonstrates that the tumor cell line falls within the SSIFT filter – there may be interest in a quantitative histological validation. There are many obstacles to achieve this, however. First, an appropriate membrane staining needs to be identified. The 9L gliosarcoma cells showed dense hematoxylin staining in both the intra and extracellular space (Figure 22), so delineation of the membrane for size estimation on conventional staining is not possible. Our group has used Na/K ATPase in previous studies of human breast cancer [49] and animal xenographs [176] to perform size measurements, but this staining was not suitable for the 9L cell line. Another issue is in the tissue preparation for histology. The tissues used in this study were fixed with formalin via transcardial perfusion and then ethanol via immersion. Ethanol has an advantage over extended immersion in formalin in its preservation of antigenicity [177], but leads to morphological changes in tissue, particularly cell size [178]. Finally, even if stains for cell membranes were identified and cellular morphology was preserved, diffusion time dependence may not be solely driven by cell diameter. Radiation necrosis saw an increase in SSIFT iAUC over normal tissue (Figure 21) that may not be fully explained by inflammatory infiltrates such as macrophages. Ischemia due to vascular degeneration is a known effect of radionecrosis, and it has been previously documented that similar effects in ischemic stroke can drive morphological changes reflected in the tissue diffusion time dependence [47,179,180]. Morphological changes such as axonal beading can be identified by histology [181], and a controlled study investigating the relationship between time-dependent diffusion, radiation injury, and axon morphology could elucidate the cause of this observation.

Quantitative cell size models. As discussed in Chapter 3, extending quantitative models such as IMPULSED to the brain could be challenging given scan time, SNR, and gradient strength constraints of clinical imaging. However, preclinical systems can often achieve higher gradient strengths, allowing shorter diffusion times at a given b-value. Additionally, preclinical applications generally do not have the throughput demands of clinical settings and scan time is therefore less of a concern. Relaxing these constraints may open the feasibility of parsing diffusion orientation, size, and volume fraction information. This has recently been of interest in neuronal soma imaging [182,183]. This could be an interesting application to cancer imaging as well – it is an analogous challenge to parse an isotropic compartment with high diffusion time-dependence (i.e., neuronal

soma, cancer cells) from a local or macroscopic compartment with little diffusion time-dependence (i.e., dendrites, axons). The work described in this thesis can move this direction forward in a few ways. First, some practical considerations concerning the integration of both PGSE and OGSE data made in this study would also apply to IMPULSED. Second, by providing a working LINAC-based model of radionecrosis, we extend the accessibility to study quantitative models of radionecrosis vs. tumor in preclinical settings. Third, while IMPULSED is unlikely to be sensitive to smaller restriction sizes in normal brain tissue with its previously used frequency domain (0-50 Hz), the SSIFT iAUC could serve as a map indicating whether a region of tissue or lesion has sufficient diffusion time dependence to fit cell sizes reliably.

Human trials. The stated goal of this project was to set up the foundational work to extend to human studies. With this goal accomplished, larger cohorts of patients with recurrent tumor or radionecrosis should be recruited. Chapters 3 and 4 showed that SSIFT is dependent on cellular volume fraction. This may turn out to be a limitation of the method in its application to primary tumors, since lower grade gliomas tend to have only moderate cellular density [184]. Metastases, however, may be a more suitable application. Non-small cell lung cancer is the most common type of brain metastasis [2], has large cell sizes suitable for SSIFT [115], showed sensitivity to SSIFT in our *in vitro* study (Figure 19), has high cell density [185], and had high contrast in our preliminary patient data (Figure 23). Its incidence and cellular suitability for SSIFT make it a good candidate for future human trials. We also scanned one subject with melanoma (Figure 23) which had visible contrast in SSIFT, but the lesion was not corroborated with Gd-MRI due to the patient having a kidney dysfunction. Given the SSIFT response to both human melanoma and breast cancer cells in our *in vitro* study (Figure 19), additional preliminary data in these cancer lines may also be promising applications of SSIFT.

References

[1]   United States Cancer Statistics (USCS). National Program of Cancer Registries and Surveillance, Epidemiology, and End Results Program SEER*Stat Database: NPCR and SEER Incidence – U.S. Cancer Statistics 2005–2018 Public Use Research Database. Released June 2021. n.d. https://www.cdc.gov/cancer/uscs/public-use.

[2]   Barnholtz-Sloan JS, Sloan AE, Davis FG, Vigneau FD, Lai P, Sawaya RE. Incidence proportions of brain metastases in patients diagnosed (1973 to 2001) in the Metropolitan Detroit Cancer Surveillance System. J Clin Oncol 2004;22:2865–72. https://doi.org/10.1200/JCO.2004.12.149.

[3]   Siegel RL, Miller KD, Jemal A. Cancer statistics, 2016. CA Cancer J Clin 2016;66:7–30. https://doi.org/10.3322/caac.21332.

[4]   Owonikoko TK, Arbiser J, Zelnak A, Shu HKG, Shim H, Robin AM, et al. Current approaches to the treatment of metastatic brain tumours. Nat Rev Clin Oncol 2014;11:203–22. https://doi.org/10.1038/nrclinonc.2014.25.

[5]   Chang EL, Wefel JS, Hess KR, Allen PK, Lang FF, Kornguth DG, et al. Neurocognition in patients with brain metastases treated with radiosurgery or radiosurgery plus whole-brain irradiation: a randomised controlled trial. Lancet Oncol 2009;10:1037–44. https://doi.org/10.1016/S1470-2045(09)70263-3.

[6]   Lagerwaard FJ, Levendag PC, Nowak PJCM, Eijkenboom WMH, Hanssens PEJ, Schmitz PIM. Identification of prognostic factors in patients with brain metastases: A review of 1292 patients. Int J Radiat Oncol Biol Phys 1999;43:795–803. https://doi.org/10.1016/S0360-3016(98)00442-8.

[7]   Magnuson WJ, Lester-Coll NH, Wu AJ, Yang TJ, Lockney NA, Gerber NK, et al. Management of brain metastases in tyrosine kinase inhibitor-Naïve epidermal growth factor receptor-mutant non-small-cell lung cancer: A retrospective multi-institutional analysis. J Clin Oncol 2017;35:1070–7. https://doi.org/10.1200/JCO.2016.69.7144.

[8]   Ruben JD, Dally M, Bailey M, Smith R, McLean CA, Fedele P. Cerebral radiation necrosis: Incidence, outcomes, and risk factors with emphasis on radiation parameters and chemotherapy. Int J Radiat Oncol Biol Phys 2006;65:499–508. https://doi.org/10.1016/j.ijrobp.2005.12.002.

[9]   Colaco RJ, Martin P, Kluger HM, Yu JB, Chiang VL. Does immunotherapy increase the rate of radiation necrosis after radiosurgical treatment of brain metastases? J Neurosurg 2016;125:17–23. https://doi.org/10.3171/2015.6.JNS142763.

[10] Forsyth PA, Kelly PJ, Cascino TL, Scheithauer BW, Shaw EG, Dinapoli RP, et al. Radiation necrosis or glioma recurrence: Is computer-assisted stereotactic biopsy useful? J Neurosurg 1995;82:436–44. https://doi.org/10.3171/jns.1995.82.3.0436.

[11] Malone H, Yang J, Hershman DL, Wright JD, Bruce JN, Neugut AI. Complications Following Stereotactic Needle Biopsy of Intracranial Tumors. World Neurosurg 2015;84:1084–9. https://doi.org/10.1016/j.wneu.2015.05.025.

[12] Valk PE, Dillon WP. Radiation injury of the brain. AJNR Am J Neuroradiol 1991;12:45–62.

[13] Pope WB. Brain metastases: neuroimaging. Handb. Clin. Neurol., vol. 149, Elsevier B.V.; 2018, p. 89–112. https://doi.org/10.1016/B978-0-12-811161-1.00007-4.

[14] Li H, Deng L, Bai HX, Sun J, Cao Y, Tao Y, et al. Diagnostic Accuracy of Amino Acid and FDG-PET in Differentiating Brain Metastasis Recurrence from Radionecrosis after

Radiotherapy: A Systematic Review and Meta-Analysis. Am J Neuroradiol 2018;39:280–8. https://doi.org/10.3174/ajnr.A5472.

[15] Chiang GC, Kovanlikaya I, Choi C, Ramakrishna R, Magge R, Shungu DC. Magnetic resonance spectroscopy, positron emission tomography and radiogenomics-Relevance to glioma. Front Neurol 2018;9:33. https://doi.org/10.3389/fneur.2018.00033.

[16] Fink K, Fink J. Imaging of brain metastases. Surg Neurol Int 2013;4:209. https://doi.org/10.4103/2152-7806.111298.

[17] Vellayappan B, Tan CL, Yong C, Khor LK, Koh WY, Yeo TT, et al. Diagnosis and Management of Radiation Necrosis in Patients With Brain Metastases. Front Oncol 2018;8. https://doi.org/10.3389/fonc.2018.00395.

[18] Zhou J, Lal B, Wilson DA, Laterra J, Van Zijl PCM. Amide Proton Transfer (APT) Contrast for Imaging of Brain Tumors. Magn Reson Med 2003;50:1120–6. https://doi.org/10.1002/mrm.10651.

[19] Zhou J, Tryggestad E, Wen Z, Lal B, Zhou T, Grossman R, et al. Differentiation between glioma and radiation necrosis using molecular magnetic resonance imaging of endogenous proteins and peptides. Nat Med 2011;17:130–4. https://doi.org/10.1038/nm.2268.

[20] Mehrabian H, Desmond KL, Soliman H, Sahgal A, Stanisz GJ. Differentiation between radiation necrosis and tumor progression using chemical exchange saturation transfer. Clin Cancer Res 2017;23:3667–75. https://doi.org/10.1158/1078-0432.CCR-16-2265.

[21] Welker K, Boxerman J, Kalnin A, Kaufmann T, Shiroishi M, Wintermark M. ASFNR recommendations for clinical performance of MR dynamic susceptibility contrast perfusion imaging of the brain. Am J Neuroradiol 2015;36:E41–51. https://doi.org/10.3174/ajnr.A4341.

[22] Mitsuya K, Nakasu Y, Horiguchi S, Harada H, Nishimura T, Bando E, et al. Perfusion weighted magnetic resonance imaging to distinguish the recurrence of metastatic brain tumors from radiation necrosis after stereotactic radiosurgery. J Neurooncol 2010;99:81–8. https://doi.org/10.1007/s11060-009-0106-z.

[23] Kwee RM, Kwee TC. Dynamic susceptibility MR perfusion in diagnosing recurrent brain metastases after radiotherapy: A systematic review and meta-analysis. J Magn Reson Imaging 2020;51:524–34. https://doi.org/10.1002/jmri.26812.

[24] Anderson AW, Xie J, Pizzonia J, Bronen RA, Spencer DD, Gore JC. Effects of cell volume fraction changes on apparent diffusion in human cells. Magn Reson Imaging 2000;18:689–95. https://doi.org/https://doi.org/10.1016/S0730-725X(00)00147-8.

[25] Beaulieu C, Allen PS. Determinants of anisotropic water diffusion in nerves. Magn Reson Med 1994;31:394–400. https://doi.org/10.1002/MRM.1910310408.

[26] Basser PJ, Mattiello J, LeBihan D. MR diffusion tensor spectroscopy and imaging. Biophys J 1994;66:259–67. https://doi.org/10.1016/S0006-3495(94)80775-1.

[27] Xu JL, Li YL, Lian JM, Dou SW, Yan FS, Wu H, et al. Distinction between postoperative recurrent glioma and radiation injury using MR diffusion tensor imaging. Neuroradiology 2010;52:1193–9. https://doi.org/10.1007/s00234-010-0731-4.

[28] Alexiou GA, Zikou A, Tsiouris S, Goussia A, Kosta P, Papadopoulos A, et al. Comparison of diffusion tensor, dynamic susceptibility contrast MRI and 99mTc-Tetrofosmin brain SPECT for the detection of recurrent high-grade glioma. Magn Reson Imaging 2014;32:854–9. https://doi.org/10.1016/j.mri.2014.04.013.

[29] Panagiotaki E, Chan RW, Dikaios N, Ahmed HU, O'Callaghan J, Freeman A, et al. Microstructural characterization of normal and malignant human prostate tissue with

vascular, extracellular, and restricted diffusion for cytometry in tumours magnetic resonance imaging. Invest Radiol 2015;50:218–27. https://doi.org/10.1097/RLI.0000000000000115.

[30]   Xu J, Jiang X, Li H, Arlinghaus LR, McKinley ET, Devan SP, et al. Magnetic resonance imaging of mean cell size in human breast tumors. Magn Reson Med 2020;83:2002–14. https://doi.org/10.1002/mrm.28056.

[31]   Brown R. XXVII. A brief account of microscopical observations made in the months of June, July and August 1827, on the particles contained in the pollen of plants; and on the general existence of active molecules in organic and inorganic bodies. Philos Mag 1828;4:161–73. https://doi.org/10.1080/14786442808674769.

[32]   Fick A. On liquid diffusion. J Memb Sci 1995;100:33–8. https://doi.org/https://doi.org/10.1016/0376-7388(94)00230-V.

[33]   Fourier JBJ. The Analytical Theory of Heat. Cambridge Libr Collect - Math 2009. https://doi.org/DOI: 10.1017/CBO9780511693205.

[34]   Einstein A. On the Movement of Small Particles Suspended in Stationary Liquids Required by the Molecular-Kinetic Theory of Heat. Ann Phys 1905;17:549–60.

[35]   Estermann I, Stern O. Über die magnetische Ablenkung von Wasserstoffmolekülen und das magnetische Moment des Protons. II. Zeitschrift Für Phys 1933;85:17–24. https://doi.org/10.1007/BF01330774.

[36]   Frisch R, Stern O. Über die magnetische Ablenkung von Wasserstoffmolekülen und das magnetische Moment des Protons. I. Zeitschrift Für Phys 1933;85:4–16. https://doi.org/10.1007/BF01330773.

[37]   Rabi II, Zacharias JR, Millman S, Kusch P. A New Method of Measuring Nuclear Magnetic Moment. Phys Rev 1938;53:318. https://doi.org/10.1103/PhysRev.53.318.

[38]   Bloch F. Nuclear Induction. Phys Rev 1946;70:460–74. https://doi.org/10.1103/PhysRev.70.460.

[39]   Purcell EM, Torrey HC, Pound R V. Resonance Absorption by Nuclear Magnetic Moments in a Solid. Phys Rev 1946;69:37–8. https://doi.org/10.1103/PhysRev.69.37.

[40]   Hahn EL. Spin Echoes. Phys Rev 1950;80:580–94. https://doi.org/10.1103/PhysRev.80.580.

[41]   Stejskal EO, Tanner JE. Spin Diffusion Measurements: Spin Echoes in the Presence of a Time-Dependent Field Gradient. J Chem Phys 1965;42:288–92. https://doi.org/10.1063/1.1695690.

[42]   Wang LZ, Caprihan A, Fukushima E. The Narrow-Pulse Criterion for Pulsed-Gradient Spin-Echo Diffusion Measurements. J Magn Reson Ser A 1995;117:209–19. https://doi.org/https://doi.org/10.1006/jmra.1995.0754.

[43]   Douglass DC, McCall DW. Diffusion in Paraffin Hydrocarbons. J Phys Chem 1958;62:1102–7. https://doi.org/10.1021/j150567a020.

[44]   Stepišnik J. Time-dependent self-diffusion by NMR spin-echo. Phys B Condens Matter 1993;183:343–50. https://doi.org/https://doi.org/10.1016/0921-4526(93)90124-O.

[45]   Gross B, Kosfeld R. Anwendung der spin-echo-methode der messung der selbstdiffusion. Messtechnik 1969;77:171–7.

[46]   Callaghan PT, Stepišnik J. JOURNAL OF MAGNETIC RESONANCE, Series A 117, 118–122 (1995) COMMUNICATIONS Frequency-Domain Analysis of Spin Motion Using Modulated-Gradient NMR 1995.

[47]   Does MD, Parsons EC, Gore JC. Oscillating gradient measurements of water diffusion in

normal and globally ischemic rat brain. Magn Reson Med 2003;49:206–15. https://doi.org/10.1002/MRM.10385.

[48]   Parsons EC, Does MD, Gore JC. Temporal diffusion spectroscopy: Theory and implementation in restricted systems using oscillating gradients. Magn Reson Med 2006;55:75–84. https://doi.org/10.1002/MRM.20732.

[49]   Xu J, Jiang X, Li H, Arlinghaus LR, McKinley ET, Devan SP, et al. Magnetic resonance imaging of mean cell size in human breast tumors. Magn Reson Med 2020;83:2002–14. https://doi.org/10.1002/mrm.28056.

[50]   Harkins KD, Galons J-P, Secomb TW, Trouard TP. Assessment of the effects of cellular tissue properties on ADC measurements by numerical simulation of water diffusion. Magn Reson Med 2009;62:1414–22. https://doi.org/https://doi.org/10.1002/mrm.22155.

[51]   Eis M, Els T, Hoehn-Berlage M. High resolution quantitative relaxation and diffusion mri of three different experimental brain tumors in rat. Magn Reson Med 1995;34:835–44. https://doi.org/https://doi.org/10.1002/mrm.1910340608.

[52]   Guo Y, Cai Y-Q, Cai Z-L, Gao Y-G, An N-Y, Ma L, et al. Differentiation of clinically benign and malignant breast lesions using diffusion-weighted imaging. J Magn Reson Imaging 2002;16:172–8. https://doi.org/https://doi.org/10.1002/jmri.10140.

[53]   Surov A, Meyer HJ, Wienke A. Correlation between apparent diffusion coefficient (ADC) and cellularity is different in several tumors: a meta-analysis. Oncotarget 2017;8:59492–9. https://doi.org/10.18632/oncotarget.17752.

[54]   Ginzberg MB, Kafri R, Kirschner M. Cell biology. On being the right (cell) size. Science 2015;348:1245075. https://doi.org/10.1126/science.1245075.

[55]   Dhawan S, Georgia S, Bhushan A. Formation and regeneration of the endocrine pancreas. Curr Opin Cell Biol 2007;19:634–45. https://doi.org/10.1016/j.ceb.2007.09.015.

[56]   Killander D, Zetterberg A. A quantitative cytochemical investigation of the relationship between cell mass and initiation of DNA synthesis in mouse fibroblasts in vitro. Exp Cell Res 1965;40:12–20. https://doi.org/https://doi.org/10.1016/0014-4827(65)90285-5.

[57]   Johnston GC, Pringle JR, Hartwell LH. Coordination of growth with cell division in the yeast Saccharomyces cerevisiae. Exp Cell Res 1977;105:79–98. https://doi.org/https://doi.org/10.1016/0014-4827(77)90154-9.

[58]   Bortner CD, Cidlowski JA. A necessary role for cell shrinkage in apoptosis. Biochem Pharmacol 1998;56:1549–59. https://doi.org/https://doi.org/10.1016/S0006-2952(98)00225-1.

[59]   Jiang X, Dudzinski S, Beckermann KE, Young K, McKinley E, McIntyre JO, et al. MRI of tumor T cell infiltration in response to checkpoint inhibitor therapy. J Immunother Cancer 2020;8:e000328. https://doi.org/10.1136/jitc-2019-000328.

[60]   Jiang X, Li H, Xie J, Zhao P, Gore JC, Xu J. Quantification of cell size using temporal diffusion spectroscopy. Magn Reson Med 2016;75:1076–85. https://doi.org/10.1002/mrm.25684.

[61]   Jiang X, Li H, Xie J, McKinley ET, Zhao P, Gore JC, et al. In vivo imaging of cancer cell size and cellularity using temporal diffusion spectroscopy. Magn Reson Med 2017;78:156–64. https://doi.org/10.1002/mrm.26356.

[62]   Wu D, Jiang K, Li H, Zhang Z, Ba R, Zhang Y, et al. Time-Dependent Diffusion MRI for Quantitative Microstructural Mapping   of Prostate Cancer. Radiology 2022:211180. https://doi.org/10.1148/radiol.211180.

[63]   Panagiotaki E, Walker-Samuel S, Siow B, Johnson SP, Rajkumar V, Pedley RB, et al.

Noninvasive Quantification of Solid Tumor Microstructure Using VERDICT MRI. Cancer Res 2014;74:1902–12. https://doi.org/10.1158/0008-5472.CAN-13-2511.

[64] Bonet-Carne E, Johnston E, Daducci A, Jacobs JG, Freeman A, Atkinson D, et al. VERDICT-AMICO: Ultrafast fitting algorithm for non-invasive prostate microstructure characterization. NMR Biomed 2019;32:e4019. https://doi.org/10.1002/NBM.4019.

[65] Doran M, Hajnal J V, Bruggen N Van, King MD, Young IR, Bydder GM. Normal and Abnormal White Matter Tracts Shown by MR Imaging using Directional Diffusion Weighted Sequences. J Comput Assist Tomogr 1990;14.

[66] Beaulieu C, Allen PS. Determinants of anisotropic water diffusion in nerves. Magn Reson Med 1994. https://doi.org/10.1002/mrm.1910310408.

[67] Tournier JD, Calamante F, Gadian DG, Connelly A. Direct estimation of the fiber orientation density function from diffusion-weighted MRI data using spherical deconvolution. Neuroimage 2004;23:1176–85. https://doi.org/10.1016/j.neuroimage.2004.07.037.

[68] Anderson AW. Measurement of fiber orientation distributions using high angular resolution diffusion imaging. Magn Reson Med 2005;54:1194–206. https://doi.org/https://doi.org/10.1002/mrm.20667.

[69] Tournier J-D, Calamante F, Connelly A. Robust determination of the fibre orientation distribution in diffusion MRI: Non-negativity constrained super-resolved spherical deconvolution. Neuroimage 2007;35:1459–72. https://doi.org/https://doi.org/10.1016/j.neuroimage.2007.02.016.

[70] Tuch DS. Q-ball imaging. Magn Reson Med 2004;52:1358–72. https://doi.org/https://doi.org/10.1002/mrm.20279.

[71] Jespersen SN, Kroenke CD, Østergaard L, Ackerman JJH, Yablonskiy DA. Modeling dendrite density from magnetic resonance diffusion measurements. Neuroimage 2007;34:1473–86. https://doi.org/https://doi.org/10.1016/j.neuroimage.2006.10.037.

[72] Kaden E, Kelm ND, Carson RP, Does MD, Alexander DC. Multi-compartment microscopic diffusion imaging. Neuroimage 2016;139:346–59. https://doi.org/10.1016/j.neuroimage.2016.06.002.

[73] Thornton JS, Ordidge RJ, Penrice J, Cady EB, Amess PN, Punwani S, et al. Anisotropic water diffusion in white and gray matter of the neonatal piglet brain before and after transient hypoxia-ischaemia. Magn Reson Imaging 1997;15:433–40. https://doi.org/https://doi.org/10.1016/S0730-725X(96)00378-5.

[74] Assaf Y. Imaging laminar structures in the gray matter with diffusion MRI. Neuroimage 2019;197:677–88. https://doi.org/https://doi.org/10.1016/j.neuroimage.2017.12.096.

[75] Liewald D, Miller R, Logothetis N, Wagner H-J, Schüz A. Distribution of axon diameters in cortical white matter: an electron-microscopic study on three human brains and a macaque. Biol Cybern 2014;108:541–57. https://doi.org/10.1007/s00422-014-0626-2.

[76] Rajkowska G, Selemon LD, Goldman-Rakic PS. Neuronal and glial somal size in the prefrontal cortex: A postmortem morphometric study of schizophrenia and huntington disease. Arch Gen Psychiatry 1998;55:215–24. https://doi.org/10.1001/archpsyc.55.3.215.

[77] Larsen NY, Li X, Tan X, Ji G, Lin J, Rajkowska G, et al. Cellular 3D-reconstruction and analysis in the human cerebral cortex using automatic serial sections. Commun Biol 2021;4:1030. https://doi.org/10.1038/s42003-021-02548-6.

[78] Zaccagna F, Riemer F, Priest AN, McLean MA, Allinson K, Grist JT, et al. Non-invasive assessment of glioma microstructure using VERDICT MRI: correlation with histology.

Eur Radiol 2019;29:5559–66. https://doi.org/10.1007/s00330-019-6011-8.

[79]   Mills R. Self-diffusion in normal and heavy water in the range 1-45.deg. J Phys Chem 2002;77:685–8. https://doi.org/10.1021/J100624A025.

[80]   Assaf Y, Freidlin R, Rohde G, Basser P. New modeling and experimental framework to characterize hindered and restricted water diffusion in brain white matter. Magn Reson Med 2004;52:965–78. https://doi.org/10.1002/MRM.20274.

[81]   Clark CA, Hedehus M, Moseley ME. Diffusion time dependence of the apparent diffusion tensor in healthy human brain and white matter disease. Magn Reson Med 2001;45:1126–9. https://doi.org/10.1002/MRM.1149.

[82]   Baron C, Beaulieu C. Oscillating gradient spin-echo (OGSE) diffusion tensor imaging of the human brain. Magn Reson Med 2014;72:726–36. https://doi.org/10.1002/MRM.24987.

[83]   Xu J, Li H, Li K, Harkins KD, Jiang X, Xie J, et al. Fast and simplified mapping of mean axon diameter using temporal diffusion spectroscopy. NMR Biomed 2016;29:400–10. https://doi.org/10.1002/nbm.3484.

[84]   Devan S, Jiang X, Bagnato F, Xu J. Optimization and numerical evaluation of multi-compartment diffusion MRI using the spherical mean technique for practical multiple sclerosis imaging. Magn Reson Imaging 2020;74:56–63. https://doi.org/10.1016/J.MRI.2020.09.002.

[85]   Oh J, Cha S, Aiken AH, Han ET, Crane JC, Stainsby JA, et al. Quantitative apparent diffusion coefficients and T2 relaxation times in characterizing contrast enhancing brain tumors and regions of peritumoral edema. J Magn Reson Imaging 2005;21:701–8. https://doi.org/10.1002/JMRI.20335.

[86]   Raffelt D, Tournier JD, Rose S, Ridgway GR, Henderson R, Crozier S, et al. Apparent Fibre Density: A novel measure for the analysis of diffusion-weighted magnetic resonance images. Neuroimage 2012;59:3976–94. https://doi.org/10.1016/J.NEUROIMAGE.2011.10.045.

[87]   Jensen JH, Helpern JA. MRI quantification of non-Gaussian water diffusion by kurtosis analysis. NMR Biomed 2010;23:698–710. https://doi.org/10.1002/nbm.1518.

[88]   Gudbjartsson H, Patz S. The Rician distribution of noisy MRI data. Magn Reson Med 1995;34:910–4. https://doi.org/10.1002/mrm.1910340618.

[89]   Veraart J, Novikov DS, Christiaens D, Ades-aron B, Sijbers J, Fieremans E. Denoising of diffusion MRI using random matrix theory. Neuroimage 2016;142:394. https://doi.org/10.1016/J.NEUROIMAGE.2016.08.016.

[90]   Does MD, Olesen JL, Harkins KD, Serradas-Duarte T, Gochberg DF, Jespersen SN, et al. Evaluation of principal component analysis image denoising on multi-exponential MRI relaxometry. Magn Reson Med 2019;81:3503–14. https://doi.org/10.1002/mrm.27658.

[91]   Ahn CB, Cho ZH. Analysis of the eddy-current induced artifacts and the temporal compensation in nuclear magnetic resonance imaging. IEEE Trans Med Imaging 1991;10:47–52. https://doi.org/10.1109/42.75610.

[92]   Andersson JLR, Sotiropoulos SN. An integrated approach to correction for off-resonance effects and subject movement in diffusion MR imaging. Neuroimage 2016;125:1063. https://doi.org/10.1016/J.NEUROIMAGE.2015.10.019.

[93]   Valsamis JJ, Dubovan PI, Baron CA. Characterization and correction of time-varying eddy currents for diffusion MRI. Magn Reson Med 2022;87:2209–23. https://doi.org/https://doi.org/10.1002/mrm.29124.

[94] Tournier JD, Smith R, Raffelt D, Tabbara R, Dhollander T, Pietsch M, et al. MRtrix3: A fast, flexible and open software framework for medical image processing and visualisation. Neuroimage 2019;202:116137. https://doi.org/10.1016/J.NEUROIMAGE.2019.116137.

[95] Kellner E, Dhital B, Kiselev VG, Reisert M. Gibbs-ringing artifact removal based on local subvoxel-shifts. Magn Reson Med 2016;76:1574–81. https://doi.org/10.1002/MRM.26054.

[96] Andersson JLR, Skare S, Ashburner J. How to correct susceptibility distortions in spin-echo echo-planar images: application to diffusion tensor imaging. Neuroimage 2003;20:870–88. https://doi.org/https://doi.org/10.1016/S1053-8119(03)00336-7.

[97] Jenkinson M, Beckmann CF, Behrens TEJ, Woolrich MW, Smith SM. FSL. Neuroimage 2012;62:782–90. https://doi.org/10.1016/j.neuroimage.2011.09.015.

[98] Smith SM, Jenkinson M, Woolrich MW, Beckmann CF, Behrens TEJ, Johansen-Berg H, et al. Advances in functional and structural MR image analysis and implementation as FSL. Neuroimage, vol. 23, Neuroimage; 2004. https://doi.org/10.1016/j.neuroimage.2004.07.051.

[99] Veraart J, Sijbers J, Sunaert S, Leemans A, Jeurissen B. Weighted linear least squares estimation of diffusion MRI parameters: Strengths, limitations, and pitfalls. Neuroimage 2013;81:335–46. https://doi.org/https://doi.org/10.1016/j.neuroimage.2013.05.028.

[100] Rastogi K, Bhaskar S, Gupta S, Jain S, Singh D, Kumar P. Palliation of Brain Metastases: Analysis of Prognostic Factors Affecting Overall Survival. Indian J Palliat Care 2018;24:308–12. https://doi.org/10.4103/IJPC.IJPC_1_18.

[101] Nieder C, Grosu AL, Gaspar LE. Stereotactic radiosurgery (SRS) for brain metastases: a systematic review. Radiat Oncol 2014;9:155. https://doi.org/10.1186/1748-717X-9-155.

[102] Ammirati M, Cobbs CS, Linskey ME, Paleologos NA, Ryken TC, Burri SH, et al. The role of retreatment in the management of recurrent/progressive brain metastases: a systematic review and evidence-based clinical practice guideline. J Neurooncol 2010;96:85–96. https://doi.org/10.1007/s11060-009-0055-6.

[103] Shah R, Vattoth S, Jacob R, Manzil FFP, O'Malley JP, Borghei P, et al. Radiation Necrosis in the Brain: Imaging Features and Differentiation from Tumor Recurrence. RadioGraphics 2012;32:1343–59. https://doi.org/10.1148/rg.325125002.

[104] Schouten LJ, Rutten J, Huveneers HAM, Twijnstra A. Incidence of brain metastases in a cohort of patients with carcinoma of the breast, colon, kidney, and lung and melanoma. Cancer 2002;94:2698–705. https://doi.org/10.1002/cncr.10541.

[105] Boyle W, Chow A. Isolation of Human Lymphocytes by a Ficoll Barrier Method. Transfusion 1969;9:151–5. https://doi.org/10.1111/j.1537-2995.1969.tb05534.x.

[106] Schneider CA, Rasband WS, Eliceiri KW. NIH Image to ImageJ: 25 years of image analysis. Nat Methods 2012;9:671–5. https://doi.org/10.1038/nmeth.2089.

[107] Jost SC, Hope A, Kiehl E, Perry A, Travers S, Garbow JR. A Novel Murine Model for Localized Radiation Necrosis and its Characterization using Advanced Magnetic Resonance Imaging. Int J Radiat Oncol Biol Phys 2009;75:527–33. https://doi.org/10.1016/J.IJROBP.2009.06.007.

[108] Jiang X, Engelbach JA, Yuan L, Cates J, Gao F, Drzymala RE, et al. Anti-VEGF antibodies mitigate the development of radiation necrosis in mouse brain. Clin Cancer Res 2014;20:2695–702. https://doi.org/10.1158/1078-0432.CCR-13-1941.

[109] Bankhead P, Loughrey MB, Fernández JA, Dombrowski Y, McArt DG, Dunne PD, et al.

QuPath: Open source software for digital pathology image analysis. Sci Reports 2017 71 2017;7:1–7. https://doi.org/10.1038/s41598-017-17204-5.

[110] Woolrich MW, Jbabdi S, Patenaude B, Chappell M, Makni S, Behrens T, et al. Bayesian analysis of neuroimaging data in FSL. Neuroimage 2009;45. https://doi.org/10.1016/j.neuroimage.2008.10.055.

[111] Tustison NJ, Avants BB, Cook PA, Zheng Y, Egan A, Yushkevich PA, et al. N4ITK: Improved N3 bias correction. IEEE Trans Med Imaging 2010;29:1310–20. https://doi.org/10.1109/TMI.2010.2046908.

[112] Gao F, Shen X, Zhang H, Ba R, Ma X, Lai C, et al. Feasibility of oscillating and pulsed gradient diffusion MRI to assess neonatal hypoxia-ischemia on clinical systems. J Cereb Blood Flow Metab 2021;41:1240–50. https://doi.org/10.1177/0271678X20944353.

[113] Daducci A, Canales-Rodríguez EJ, Zhang H, Dyrby TB, Alexander DC, Thiran JP. Accelerated Microstructure Imaging via Convex Optimization (AMICO) from diffusion MRI data. Neuroimage 2015;105:32–44. https://doi.org/10.1016/j.neuroimage.2014.10.026.

[114] Pronin IN, Kornienko V N, Fadeeva L M, Rodionov P V, Golanov A V. [Diffusion-weighted image in the study of brain tumors and peritumoral edema] . Zh Vopr Neirokhir Im N N Burdenko 2000:14–6.

[115] Hosokawa M, Kenmotsu H, Koh Y, Yoshino T, Yoshikawa T, Naito T, et al. Size-Based Isolation of Circulating Tumor Cells in Lung Cancer Patients Using a Microcavity Array System. PLoS One 2013;8. https://doi.org/10.1371/journal.pone.0067466.

[116] Molina JR, Yang P, Cassivi SD, Schild SE, Adjei AA. Non-small cell lung cancer: Epidemiology, risk factors, treatment, and survivorship. Mayo Clin. Proc., vol. 83, Elsevier Ltd; 2008, p. 584–94. https://doi.org/10.4065/83.5.584.

[117] Van AT, Holdsworth SJ, Bammer R. In vivo investigation of restricted diffusion in the human brain with optimized oscillating diffusion gradient encoding. Magn Reson Med 2014;71:83–94. https://doi.org/10.1002/mrm.24632.

[118] Wu D, Zhang J. The Effect of Microcirculatory Flow on Oscillating Gradient Diffusion MRI and Diffusion Encoding with Dual-Frequency Orthogonal Gradients (DEFOG). Magn Reson Med 2017;77:1583–92. https://doi.org/10.1002/mrm.26242.

[119] Jiang X, Xu J, Gore JC. Mapping hepatocyte size in vivo using temporal diffusion spectroscopy MRI. Magn Reson Med 2020;84:2671–83. https://doi.org/10.1002/mrm.28299.

[120] Holdsworth SJ, O'Halloran R, Setsompop K. The quest for high spatial resolution diffusion-weighted imaging of the human brain in vivo. NMR Biomed 2019;32:e4056. https://doi.org/10.1002/NBM.4056.

[121] Dequesada IM, Quisling RG, Yachnis A, Friedman WA. Can standard magnetic resonance imaging reliably distinguish recurrent tumor from radiation necrosis after radiosurgery for brain metastases? A radiographic-pathological study. Neurosurgery 2008;63:898–903. https://doi.org/10.1227/01.NEU.0000333263.31870.31.

[122] Stockham AL, Tievsky AL, Koyfman SA, Reddy CA, Suh JH, Vogelbaum MA, et al. Conventional MRI does not reliably distinguish radiation necrosis from tumor recurrence after stereotactic radiosurgery. J Neurooncol 2012;109:149–58. https://doi.org/10.1007/s11060-012-0881-9.

[123] Ross B, Moffat B, Lawrence T, Mukherji S, Gebarski S, Quint D, et al. Evaluation of cancer therapy using diffusion magnetic resonance imaging. Mol Cancer Ther

2003;2:581–7.

[124] Masch WR, Wang PI, Chenevert TL, Junck L, Tsien C, Heth JA, et al. Comparison of Diffusion Tensor Imaging and Magnetic Resonance Perfusion Imaging in Differentiating Recurrent Brain Neoplasm From Radiation Necrosis. Acad Radiol 2016;23:569–76. https://doi.org/10.1016/j.acra.2015.11.015.

[125] Heiss W-D, Raab P, Lanfermann H. Multimodality Assessment of Brain Tumors and Tumor Recurrence. J Nucl Med 2011;52:1585 LP – 1600. https://doi.org/10.2967/jnumed.110.084210.

[126] Fink JR, Muzi M, Peck M, Krohn KA. Multimodality Brain Tumor Imaging: MR Imaging, PET, and PET/MR Imaging. J Nucl Med 2015;56:1554 LP – 1561. https://doi.org/10.2967/jnumed.113.131516.

[127] Nael K, Bauer AH, Hormigo A, Lemole M, Germano IM, Puig J, et al. Multiparametric MRI for Differentiation of Radiation Necrosis From Recurrent Tumor in Patients With Treated Glioblastoma. Am J Roentgenol 2017;210:18–23. https://doi.org/10.2214/AJR.17.18003.

[128] Di Costanzo A, Scarabino T, Trojsi F, Popolizio T, Bonavita S, de Cristofaro M, et al. Recurrent glioblastoma multiforme versus radiation injury: a multiparametric 3-T MR approach. Radiol Med 2014;119:616–24. https://doi.org/10.1007/s11547-013-0371-y.

[129] Zaiß M, Schmitt B, Bachert P. Quantitative separation of CEST effect from magnetization transfer and spillover effects by Lorentzian-line-fit analysis of z-spectra. J Magn Reson 2011;211:149–55. https://doi.org/https://doi.org/10.1016/j.jmr.2011.05.001.

[130] O'Haver T. peakfit.m. MATLAB Cent File Exch 2022. https://www.mathworks.com/matlabcentral/fileexchange/23611-peakfit-m.

[131] Gochberg DF, Gore JC. Quantitative imaging of magnetization transfer using an inversion recovery sequence. Magn Reson Med 2003;49:501–5. https://doi.org/10.1002/MRM.10386.

[132] Xu J, Li K, Zu Z, Li X, Gochberg DF, Gore JC. Quantitative magnetization transfer imaging of rodent glioma using selective inversion recovery. NMR Biomed 2014;27:253–60. https://doi.org/10.1002/NBM.3058.

[133] Li K, Li H, Zhang XY, Stokes AM, Jiang X, Kang H, et al. Influence of water compartmentation and heterogeneous relaxation on quantitative magnetization transfer imaging in rodent brain tumors. Magn Reson Med 2016;76:635–44. https://doi.org/10.1002/MRM.25893/ASSET/SUPINFO/MRM25893-SUP-0001-SUPPINFO01.PDF.

[134] Gochberg DF, Gore JC. Quantitative magnetization transfer imaging via selective inversion recovery with short repetition times. Magn Reson Med 2007;57:437–41. https://doi.org/10.1002/MRM.21143.

[135] Boxerman JL, Schmainda KM, Weisskoff RM. Relative Cerebral Blood Volume Maps Corrected for Contrast Agent Extravasation Significantly Correlate with Glioma Tumor Grade, Whereas Uncorrected Maps Do Not. Am J Neuroradiol 2006;27:859 LP – 867.

[136] Carroll TJ, Rowley HA, Haughton VM. Automatic Calculation of the Arterial Input Function for Cerebral Perfusion Imaging with MR Imaging. Radiology 2003;227:593–600. https://doi.org/10.1148/radiol.2272020092.

[137] Tibshirani R. Regression Shrinkage and Selection via the Lasso. J R Stat Soc Ser B 1996;58:267–88.

[138] Hoerl AE, Kennard RW. Ridge Regression: Biased Estimation for Nonorthogonal

Problems. Technometrics 1970;12:55–67. https://doi.org/10.2307/1267351.

[139] Tiwari P, Prasanna P, Wolansky L, Pinho M, Cohen M, Nayate AP, et al. Computer-Extracted Texture Features to Distinguish Cerebral Radionecrosis from Recurrent Brain Tumors on Multiparametric MRI: A Feasibility Study. Am J Neuroradiol 2016;37:2231 LP – 2236. https://doi.org/10.3174/ajnr.A4931.

[140] Wong CS, Fehlings MG, Sahgal A. Pathobiology of radiation myelopathy and strategies to mitigate injury. Spinal Cord 2015;53:574–80. https://doi.org/10.1038/SC.2015.43.

[141] Li Y-Q, Chen P, Haimovitz-Friedman A, Reilly RM, Wong CS. Endothelial Apoptosis Initiates Acute Blood–Brain Barrier Disruption after Ionizing Radiation. Cancer Res 2003;63:5950 LP – 5956.

[142] Coderre JA, Morris GM, Micca PL, Hopewell JW, Verhagen I, Kleiboer BJ, et al. Late effects of radiation on the central nervous system: role of vascular endothelial damage and glial stem cell survival. Radiat Res 2006;166:495–503. https://doi.org/10.1667/RR3597.1.

[143] Tuleasca C, Régis J, Sahgal A, De Salles A, Hayashi M, Ma L, et al. Stereotactic radiosurgery for trigeminal neuralgia: a systematic review. J Neurosurg 2018;130:733–57. https://doi.org/10.3171/2017.9.JNS17545.

[144] Dallapiazza RF, Lee DJ, De Vloo P, Fomenko A, Hamani C, Hodaie M, et al. Outcomes from stereotactic surgery for essential tremor. J Neurol Neurosurg Psychiatry 2019;90:474–82. https://doi.org/10.1136/JNNP-2018-318240.

[145] Martínez-Moreno NE, Sahgal A, De Salles A, Hayashi M, Levivier M, Ma L, et al. Stereotactic radiosurgery for tremor: systematic review. J Neurosurg 2018;130:589–600. https://doi.org/10.3171/2017.8.JNS17749.

[146] Pérez-Sánchez JR, Martínez-Álvarez R, Martínez Moreno NE, Torres Diaz C, Rey G, Pareés I, et al. Gamma Knife® stereotactic radiosurgery as a treatment for essential and parkinsonian tremor: long-term experience. Neurologia 2020. https://doi.org/10.1016/J.NRL.2020.05.014.

[147] Luo G, Cameron BD, Wang L, Yu H, Neimat JS, Hedera P, et al. Targeting for stereotactic radiosurgical thalamotomy based on tremor treatment response. J Neurosurg 2021:1–8. https://doi.org/10.3171/2021.7.JNS21160.

[148] Kondziolka D, Flickinger JC, Lunsford LD. Stereotactic radiosurgery for epilepsy and functional disorders. Neurosurg Clin N Am 2013;24:623–32. https://doi.org/10.1016/J.NEC.2013.06.001.

[149] Martínez-Álvarez R. Radiosurgery for Behavioral Disorders. Prog Neurol Surg 2019;34:289–97. https://doi.org/10.1159/000493076.

[150] Barani IJ, Larson DA. Radiation therapy of glioblastoma. Cancer Treat Res 2015;163:49–73. https://doi.org/10.1007/978-3-319-12048-5_4.

[151] Soliman H, Das S, Larson DA, Sahgal A. Stereotactic radiosurgery (SRS) in the modern management of patients with brain metastases. Oncotarget 2016;7:12318–30. https://doi.org/10.18632/ONCOTARGET.7131.

[152] Thiagarajan A, Yamada Y. Radiobiology and radiotherapy of brain metastases. Clin Exp Metastasis 2017;34:411–9. https://doi.org/10.1007/S10585-017-9865-7.

[153] Fink J, Born D, Chamberlain MC. Radiation necrosis: relevance with respect to treatment of primary and secondary brain tumors. Curr Neurol Neurosci Rep 2012;12:276–85. https://doi.org/10.1007/S11910-012-0258-7.

[154] Strauss SB, AMeng, Ebani EJ, Chiang GC. Imaging Glioblastoma Posttreatment: Progression, Pseudoprogression, Pseudoresponse, Radiation Necrosis. Radiol Clin North

Am 2019;57:1199–216. https://doi.org/10.1016/J.RCL.2019.07.003.

[155] Miyatake S, Nonoguchi N, Furuse M, Yoritsune E, Miyata T, Kawabata S, et al. Pathophysiology, diagnosis, and treatment of radiation necrosis in the brain. Neurol Med Chir (Tokyo) 2015;55:50–9. https://doi.org/10.2176/NMC.RA.2014-0188.

[156] Doré M, Martin S, Delpon G, Clément K, Campion L, Thillays F. Stereotactic radiotherapy following surgery for brain metastasis: Predictive factors for local control and radionecrosis. Cancer Radiother 2017;21:4–9. https://doi.org/10.1016/J.CANRAD.2016.06.010.

[157] Kohutek ZA, Yamada Y, Chan TA, Brennan CW, Tabar V, Gutin PH, et al. Long-term risk of radionecrosis and imaging changes after stereotactic radiosurgery for brain metastases. J Neurooncol 2015;125:149–56. https://doi.org/10.1007/S11060-015-1881-3.

[158] Minniti G, Scaringi C, Paolini S, Lanzetta G, Romano A, Cicone F, et al. Single-Fraction Versus Multifraction (3 × 9 Gy) Stereotactic Radiosurgery for Large (>2 cm) Brain Metastases: A Comparative Analysis of Local Control and Risk of Radiation-Induced Brain Necrosis. Int J Radiat Oncol Biol Phys 2016;95:1142–8. https://doi.org/10.1016/J.IJROBP.2016.03.013.

[159] Kiehl EL, Stojadinovic S, Malinowski KT, Limbrick D, Jost SC, Garbow JR, et al. Feasibility of small animal cranial irradiation with the microRT system. Med Phys 2008;35:4735. https://doi.org/10.1118/1.2977762.

[160] Wong J, Armour E, Kazanzides P, Iordachita I, Tryggestad E, Deng H, et al. A high resolution small animal radiation research platform (SARRP) with x-ray tomographic guidance capabilities. Int J Radiat Oncol Biol Phys 2008;71:1591. https://doi.org/10.1016/J.IJROBP.2008.04.025.

[161] Kondziolka D, Lunsford LD, Claassen D, Maitz AH, Flickinger JC. Radiobiology of RadiosurgeryPart I. The Normal Rat Brain Model. Neurosurgery 1992;31:271–9. https://doi.org/10.1227/00006123-199208000-00012.

[162] Mori Y, Kondziolka D, Balzer J, Fellows W, Flickinger JC, Lunsford LD, et al. Effects of Stereotactic Radiosurgery on an Animal Model of Hippocampal Epilepsy. Neurosurgery 2000;46:157–68. https://doi.org/10.1093/NEUROSURGERY/46.1.157.

[163] Jiang X, Yuan L, Engelbach JA, Cates J, Perez-Torres CJ, Gao F, et al. A gamma-knife-enabled mouse model of cerebral single-hemisphere delayed radiation necrosis. PLoS One 2015;10. https://doi.org/10.1371/JOURNAL.PONE.0139596.

[164] Jiang X, Perez-Torres CJ, Thotala D, Engelbach JA, Yuan L, Cates J, et al. A GSK-3β inhibitor protects against radiation necrosis in mouse brain. Int J Radiat Oncol Biol Phys 2014;89:714–21. https://doi.org/10.1016/J.IJROBP.2014.04.018.

[165] Hartl BA, Ma HSW, Hansen KS, Perks J, Kent MS, Fragoso RC, et al. The effect of radiation dose on the onset and progression of radiation-induced brain necrosis in the rat model. Int J Radiat Biol 2017;93:676–82. https://doi.org/10.1080/09553002.2017.1297902.

[166] Kumar S, Arbab AS, Jain R, Kim J, DeCarvalho AC, Shankar A, et al. Development of a novel animal model to differentiate radiation necrosis from tumor recurrence. J Neuro-Oncology 2012 1083 2012;108:411–20. https://doi.org/10.1007/S11060-012-0846-Z.

[167] Khattab MH, Cmelak AJ, Sherry AD, Luo G, Wang L, Yu H, et al. Noninvasive Thalamotomy for Refractory Tremor by Frameless Radiosurgery. Int J Radiat Oncol Biol Phys 2021. https://doi.org/10.1016/J.IJROBP.2021.08.021.

[168] Park HS, Wang EH, Rutter CE, Corso CD, Chiang VL, Yu JB. Changing practice patterns

of Gamma Knife versus linear accelerator-based stereotactic radiosurgery for brain metastases in the US. J Neurosurg 2016;124:1018–24. https://doi.org/10.3171/2015.4.JNS1573.

[169] Luo G, Neimat JS, Cmelak A, Kirschner AN, Attia A, Morales-Paliza M, et al. Margin of error for a frameless image guided radiosurgery system: Direct confirmation based on posttreatment MRI scans. Pract Radiat Oncol 2017;7:e223–31. https://doi.org/10.1016/J.PRRO.2016.08.006.

[170] Mainwaring W, Bowers J, Pham N, Pezzi T, Shukla M, Bonnen M, et al. Stereotactic Radiosurgery Versus Whole Brain Radiation Therapy: A Propensity Score Analysis and Predictors of Care for Patients With Brain Metastases From Breast Cancer. Clin Breast Cancer 2019;19:e343–51. https://doi.org/10.1016/J.CLBC.2018.11.001.

[171] Yang L, Yang J, Li G, Li Y, Wu R, Cheng J, et al. Pathophysiological Responses in Rat and Mouse Models of Radiation-Induced Brain Injury. Mol Neurobiol 2015 542 2016;54:1022–32. https://doi.org/10.1007/S12035-015-9628-X.

[172] Sharma S, Narayanasamy G, Przybyla B, Webber J, Boerma M, Clarkson R, et al. Advanced Small Animal Conformal Radiation Therapy Device. Technol Cancer Res Treat 2017;16:45–56. https://doi.org/10.1177/1533034615626011.

[173] Verhaegen F, Dubois L, Gianolini S, Hill MA, Karger CP, Lauber K, et al. ESTRO ACROP: Technology for precision small animal radiotherapy research: Optimal use and challenges. Radiother Oncol 2018;126:471–8. https://doi.org/10.1016/J.RADONC.2017.11.016.

[174] Kim H, Fabien J, Zheng Y, Yuan J, Brindle J, Sloan A, et al. Establishing a process of irradiating small animal brain using a CyberKnife and a microCT scanner. Med Phys 2014;41:021715. https://doi.org/10.1118/1.4861713.

[175] Sinha TK, Khatib-Shahidi S, Yankeelov TE, Mapara K, Ehtesham M, Cornett DS, et al. Integrating spatially resolved three-dimensional MALDI IMS with in vivo magnetic resonance imaging. Nat Methods 2008;5:57. https://doi.org/10.1038/NMETH1147.

[176] Jiang X, McKinley ET, Xie J, Li H, Xu J, Gore JC. In vivo magnetic resonance imaging of treatment-induced apoptosis. Sci Rep 2019;9:9540. https://doi.org/10.1038/s41598-019-45864-y.

[177] Scalia CR, Boi G, Bolognesi MM, Riva L, Manzoni M, DeSmedt L, et al. Antigen Masking During Fixation and Embedding, Dissected. J Histochem Cytochem 2017;65:5–20. https://doi.org/10.1369/0022155416673995.

[178] Li Y, Almassalha LM, Chandler JE, Zhou X, Stypula-Cyrus YE, Hujsak KA, et al. The effects of chemical fixation on the cellular nanostructure. Exp Cell Res 2017;358:253–9. https://doi.org/10.1016/j.yexcr.2017.06.022.

[179] Baron CA, Kate M, Gioia L, Butcher K, Emery D, Budde M, et al. Reduction of Diffusion-Weighted Imaging Contrast of Acute Ischemic Stroke at Short Diffusion Times. Stroke 2015;46:2136–41. https://doi.org/10.1161/STROKEAHA.115.008815.

[180] Budde MD, Frank JA. Neurite beading is sufficient to decrease the apparent diffusion coefficient after ischemic stroke. Proc Natl Acad Sci 2010;107:14472–7. https://doi.org/10.1073/pnas.1004841107.

[181] Garthwaite G, Brown G, Batchelor AM, Goodwin DA, Garthwaite J. Mechanisms of ischaemic damage to central white matter axons: a quantitative histological analysis using rat optic nerve. Neuroscience 1999;94:1219–30. https://doi.org/https://doi.org/10.1016/S0306-4522(99)00389-9.

[182] Gyori NG, Clark CA, Alexander DC, Kaden E. On the potential for mapping apparent neural soma density via a clinically viable diffusion MRI protocol. Neuroimage 2021;239:118303. https://doi.org/https://doi.org/10.1016/j.neuroimage.2021.118303.

[183] Palombo M, Ianus A, Guerreri M, Nunes D, Alexander DC, Shemesh N, et al. SANDI: A compartment-based model for non-invasive apparent soma and neurite imaging by diffusion MRI. Neuroimage 2020;215:116835. https://doi.org/https://doi.org/10.1016/j.neuroimage.2020.116835.

[184] Gupta M, Djalilvand A, Brat DJ. Clarifying the Diffuse Gliomas: An Update on the Morphologic Features and Markers That Discriminate Oligodendroglioma From Astrocytoma. Am J Clin Pathol 2005;124:755–68. https://doi.org/10.1309/6JNX4PA60TQ5U5VG.

[185] Bilous M, Serdjebi C, Boyer A, Tomasini P, Pouypoudat C, Barbolosi D, et al. Quantitative mathematical modeling of clinical brain metastasis dynamics in non-small cell lung cancer. Sci Rep 2019;9:13018. https://doi.org/10.1038/s41598-019-49407-3.

[186] Bloembergen N, Purcell EM, Pound R V. Relaxation Effects in Nuclear Magnetic Resonance Absorption. Phys Rev 1948;73:679–712. https://doi.org/10.1103/PhysRev.73.679.

[187] Heitler W, Teller E. Time effects in the magnetic cooling method—I. Proc R Soc London Ser A - Math Phys Sci 1936;155:629–39. https://doi.org/10.1098/RSPA.1936.0124.

[188] Portnoy S, Flint JJ, Blackband SJ, Stanisz GJ. Oscillating and pulsed gradient diffusion magnetic resonance microscopy over an extended b-value range: implications for the characterization of tissue microstructure. Magn Reson Med 2013;69:1131–45. https://doi.org/10.1002/mrm.24325.

[189] Fordham EJ, Mitra PP, Latour LL. Effective Diffusion Times in Multiple-Pulse PFG Diffusion Measurements in Porous Media. J Magn Reson Ser A 1996;121:187–92. https://doi.org/https://doi.org/10.1006/jmra.1996.0159.